Electromagnetic Fields in Relativistic Heavy Ion Collisions

Dissertation

Presented to the School of Graduate Studies of Addis Ababa University

in Partial Fulfillment of the Requirements for the Degree

Doctor of Philosophy in Physics (Nuclear Physics)

By

Tewodros Gezhagn

Graduate Program in Physics

Addis Ababa University, Ethiopia

2021

Addis Ababa University

College of Natural and Computational Sciences

Department of Physics

The undersigned here- by certify that they have read and recommend to the College of Natural and Computational Sciences for acceptance a thesis entitled: "**Electromagnetic Fields in Relativistic Heavy Ion Collisions**" by **Tewodros Gezhagn** in partial fulfillment of the requirements for the degree of **Doctor of Philosophy in Physics (Nuclear Physics)**.

Dr. Teshome Senbeta (PhD, Assoc. Prof) Chairman	 Signature	7/18/21 Date
Prof. Shakeel Ahmad (PhD) External Examiner	 Signature	7/18/21 Date
Dr. Tilahun Tesfaye (PhD, Assist. Prof) Internal Examiner	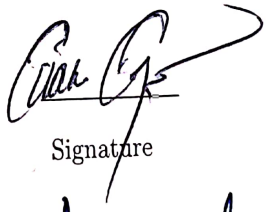 Signature	07/18/2021. Date
Prof. A. K. Chaubey (PhD) Advisor	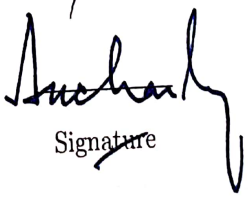 Signature	8/5/21 Date

ADDIS ABABA UNIVERSITY

Date: **March** 2021

Author: **Tewodros Gezhagn**

Title: **Electromagnetic Fields in Relativistic Heavy Ion Collisions**

Department: **Physics**

Degree: **Ph.D.** Convocation: **March** Year: **2021**

Permission is herewith granted to Addis Ababa University to circulate and to have copied for non-commercial purposes, at its discretion, the above title upon the request of individuals or institutions.

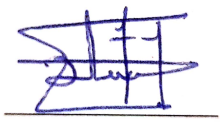

Signature of Author

ABSTRACT

Understanding the Quark Gluon Plasma, whose existence was known from the combination of three observations, is the central goal of high energy physics. All the three observations came from studying elliptic flow: how the energy, momentum and number of created particles are not uniform with direction. Any elliptic flow related studies have the chance to clear the road of understanding QGP well and answering what affects elliptic flow is part of the journey. This includes quantifying the created electromagnetic field during heavy ion collisions, which is ignored by the hydrodynamic models, and investigating its contribution to the flow of particles. So, the purpose of this research was to investigate the effect of electromagnetic field evolution created in relativistic heavy ion collision on the flow of identified particles. In order to address these problems, our model set-up followed three basic steps: describe the full relativistic viscous hydrodynamics of the considered heavy ions collision using the well known iEBE−VISHNU frame work, calculate the electromagnetic field created by the system with the possible drifting velocity sparked by it and finally investigate the change it brought to the final flow of those particles after injecting the drift velocities. The evolution of the electromagnetic fields calculated was found to play a role on the bending of flow. Beside the nature of created particles, the field evolution was affected by the electrical conductivity of the evolved system. The field arouse flow at lower transverse momentum and suppress it at higher. This change in flow is larger for heavier particles than the lighter ones during the early evolution time. Finally we found that, even flow harmonics are affected than the odds. This study definitively answers the question on whether elliptic flow is affected by the evolved electromagnetic field or not. Further study by softening many of the crude assumptions we made and a full event by event viscous hydrodynamic simulation, keeping the functionality of parameters we took as constant, is needed to establish a better ground on understanding the effect of electromagnetic field well and see from there what new things we can learn about the QGP.

In loving memory of my beloved Grandma

ጥሩዬ ካሣዉ

ACKNOWLEDGMENTS

First I would like to express my deepest gratitude to my advisor Proff. A. K. Chaubay, for his thoughtful guidance during the course works and my research time. I enjoy to work with him very much. He let me fly and land on such a fantastic research area, which made me busy and fruitful; he provided me the most inexpressible patience and freedom.

As far as my study area is concerned; I would love to thank Prof. Scott Pratt of Michigan State university for letting the inexperienced me swim in the ocean of High Energy Nuclear physics yet be there helping me not to drawn and get lost; I thank him for the research visit I had at MSU and for all the e-mails through our long distance communication too. For the code work covered in this thesis, I gratefully acknowledgement the fruitful and enlightening discussions with Chun Shen for his genuine collaborations during the code compilation.

This study happens to be realized because of the generous fundings I get from my former institution Aksum University, and that of Addis Ababa University; I am thankful for all the support I get from the two institution. The Addis Ababa University physics department staffs have played a valuable role in following my progress and for that all deserve to be acknowledged. I specially thank the head department Dr. Teshome S. for his target-full guidance and inspiring advises.

Last but not least, I thank my wife Meseret Haile for the space she has provided me to dive and get lost in my own world, yet discuss with me on every topics I feel like talking; including the physics of the nucleus. I thank my baby boy for understanding and giving me room, at the age he really wants me play with. I thank my friend and family members for their unconditional love and support. Too many other people contributed for me, thank a lot, every one. I have not replied to all the contributions I have received; sorry for that, and thanks again for the help.

VITA

March 4, 1988 . . . . . Born - Woldia, Ethiopia

September 2005 - July 2008 . . . . . BSc. in applied physics, Hawassa University

March 2008 - September 2010 . . . . . Graduate Assistant, Aksum University

September 2010 - March 2012 . . . . . MSc. in Nuclear Physics, Addis Ababa University

March 2012 - Present . . . . . Lecturer, Aksum University

Research Publication

1. Tewodros Gezhagn and A. K. Chaubey, Electromagnetic field evolution in relativistic heavy ion collision and its effect on flow of particles Sch J Phys Math Stat. DOI: 10.36347/sjpms.2021. V08i02.002 (2021).

2. Tewodros Gezhagn and A. K. Chaubey, Elliptic Flow of Particles under the Influence of Electromagnetic Field Evolution in Relativistic Heavy Ion Collision, Sch J Phys Math Stat. DOI: 10.36347/sjpms.2021. V08i02.002 (2021).

Research Visit

- Facility for Rare Isotope Beams (FRIB) and the National Superconducting Cyclotron Laboratory (NSCL) at Michigan State University in East Lansing, Michigan, USA from June through October 2016.

Workshop

- "Deuteron-induced reactions and beyond: Inclusive breakup fragment Cross sections" at the Facility for Rare Isotope Beams in East Lansing, Michigan. From July 18 to July 22, 2016,

TABLE OF CONTENTS

LIST OF TABLES

LIST OF FIGURES

Chapter 1: Introduction

Quenching our burning desire in understanding the very physics of nature happens to look on the hand of High Energy Nuclear Collision Physics. Assuming that the Big Bang actually happened, in the first moments after it, the universe was extremely hot and dense. As the universe cooled, conditions became just right to give rise to the building blocks of matter : the quarks and electrons of which we are all made. A few millionths of a second later, quarks aggregated to produce protons and neutrons. Within minutes, these protons and neutrons combined into nuclei. As the universe continued to expand and cool, things began to happen more slowly. It took 380,000 years for electrons to be trapped in orbits around nuclei, forming the first atoms [1]. Heavy-ions are extended objects and the system created in a head-on collision is different from that in a peripheral collision. To study the properties of the created system, collisions are therefore categorized by their centrality. Theoretically the centrality is defined by the impact parameter **b** (see Fig. 2.1) which, however, cannot be directly observed. Experimentally, the collision centrality can be inferred from the measured particle multiplicities, given the assumption that the multiplicity is a monotonic function of **b**. Ultra-relativistic heavy-ion collisions at RHIC and the LHC produce fireballs made of extraordinarily hot matter. Due to enormous pressure gradients between the fireball center and the surrounding vacuum, these fireballs undergo explosive collective expansion, cooling down rapidly through several different states of matter, finally fragmenting into thousands of free-streaming hadrons whose energy and momentum distributions can be detected in the detectors set up around the collider rings. The evolution history of these "Little Bangs" has much similarity with the Big Bang that created our Universe. Although they differ dramatically in geometric size and are governed by different fundamental physics (gravity for the big bang, but strong interaction for the little bang), the dynamical evolution of the little bangs share a lot of similarities with the big bang [2]. The theory toolkit in relativistic heavy ion physics is quite diverse. It includes QCD perturbation theory in the vacuum and in a thermal medium (especially for the description of jets and heavy quarkonia); semiclassical gauge theory (for the description of the initial conditions reached in the nuclear collision); lattice gauge theory (for static thermodynamic properties of QCD matter, such as its equation of state and color screening); holographic methods mapping strongly coupled gauge theories on their gravity duals (for transport properties and the dynamics of thermalization); and transport theory, especially viscous hydrodynamics (for the evolution of the bulk matter) [3]. Possible signals and probes for the quark-gluon

plasma have been investigated for around 30 years since the birth of the field. Such signatures include: collective flow [4–7], strangeness enhancement [8, 9], charmonium suppression [10, 11], thermal photon and dilepton emission [12, 13], jet quenching [14–17], critical fluctuations [18], and others. Some of the predicted signature were already found in earlier heavy ion experiments at AGS and SPS energies [19]. However, none of these signatures allow individually to prove QGP formation, as they are contaminated by the dynamical evolution of the fireball through various stages, usually from the very early pre-equilibrium stage through (perhaps) a QGP phase to the late hadronic stage. The combination of three observations at RHIC; the measurements of strong anisotropic collective flow, valence quark number scaling of the elliptic flow v_2, and jet quenching finally convinced the community that the QGP has been successfully created [20, 21]. This led to the announcement in 2005 that the QGP had been discovered at RHIC [20, 22]. Over the past decade, relativistic hydrodynamics has established itself as an indispensable component in modeling the collective dynamics of the quark-gluon plasma (QGP) produced in relativistic heavy ion collisions [23]. Over the past decade, relativistic hydrodynamics has established itself as an indispensable component in modeling the collective dynamics of the quark-gluon plasma (QGP) produced in relativistic heavy ion collisions [24–26]. Studying the hydrodynamics evolution which is affected with different parameters like, the starting time, initial energy profile, initial flow velocity and viscous stress tensor, The equation of state (EOS), the specific shear viscosity, the kinetic decoupling temperature and many more [23]. As far as Heavy Ion Nuclear Collision is concerned, we are dealing with moving charges, whether the participants, spectators or just the QGP is in mind; which leads us to get concerned of the Electromagnetic fields created from those charges. A huge ongoing effort is being employed in producing a full Magnetohydrodynamics analysis and part of it is understanding how the electromagnetic fields arise and its effect on the evolution. Our work totally deals with understanding how these fields are created and how they affect the hydrodynamic Flow of those elementary particles created in heavy ion collision in relation with other observables.

1.1 The Little Bang and the Quark Gluon Plasma

Already in the early 70's deep inelastic electron collision experiments on protons indicated that nucleons have an internal structure, they are built of quarks and gluons. The field theory which describes these quanta is the Quantum Chromodynamics (QCD). This theory leads to the conclusion that single free quarks or gluons cannot be studied or observed in our laboratories, in the so called physical vacuum, because they are confined by the strong interaction which binds them to each other [27]. Shortly after the discovery of the asymptotic freedom of QCD, people realized that common nuclear matter, confining quarks and gluons within individual protons and neutrons, could at high energy densities transform into a new de-confinement

phase called the Quark Gluon Plasma (QGP) [28, 29]. QGP is assumed to be a form of matter that once existed in the very early universe or some variant of which possibly still exists in the inner core of a neutron star. It was theoretically conjectured that such extreme conditions can also be realized on earth through colliding two heavy nuclei with ultra-relativistic energies which transform some fraction of the kinetic energies of the two nuclei into heating the QCD vacuum within an extremely small volume [30]. Before discussing about the QGP signatures, let's first explain the concept of the QGP.

1.1.1 The QGP

Quark Gluon Plasma or QGP is an interacting localized assembly of quarks and gluons at thermal (local kinetic) and (close to) chemical (abundance) equilibrium. It can also be defined as a thermalized state of quarks and gluons without color confinement [31,32]. In a QGP, the color charge of the quarks and gluons is screened. The color charge in QGP is non-abelian, whereas the electric charge in normal plasma is abelian. Outside a finite volume of QGP the color-electric field is not screened, so that a volume of QGP must still be color-neutral. It will therefore, like a nucleus, have integer electric charge. Because of the extremely high energies involved, quark-antiquark pairs are produced by pair production and thus QGP is a roughly equal mixture of quarks and antiquarks of various flavors, with only a slight excess of quarks. This property is not a general feature of conventional plasmas [33].

It was originally conceived as a weakly coupled gas, motivated by the asymptotic freedom of QCD at high energies. Using the statistics of relativistic massless fermions and bosons, one obtains the equation of state (EOS) for a free massless QGP gas [31]:

$$p = \left[g_g + \frac{7}{8}(g_q + g_{\bar{q}})\right] \frac{\pi^2}{90} T^4, \qquad e = \left[g_g + \frac{7}{8}(g_q + g_{\bar{q}})\right] \frac{\pi^2}{30} T^4. \tag{1.1}$$

These equations give the ideal EOS for a non-interacting massless QGP, $p = e/3$. If one assumes that the phase transition happens at $e \approx 1\text{GeV/fm}^3$, roughly seven times that of normal nuclear matter, then one finds a critical temperature of $T_c \approx 160$ MeV for a massless 2 flavor (u, d) QGP. In principle, the free energy and the EOS of the weakly coupled QGP can be perturbatively calculated order by order in thermal QCD. However, Lattice QCD offers a non-perturbative approach to study the QCD properties at finite temperature. Recent developments in this field have made available quite precise lattice calculations of the EOS with almost physical quark masses [34, 35]. Fig 1.1. shows the Lattice EOS (at zero chemical potential)

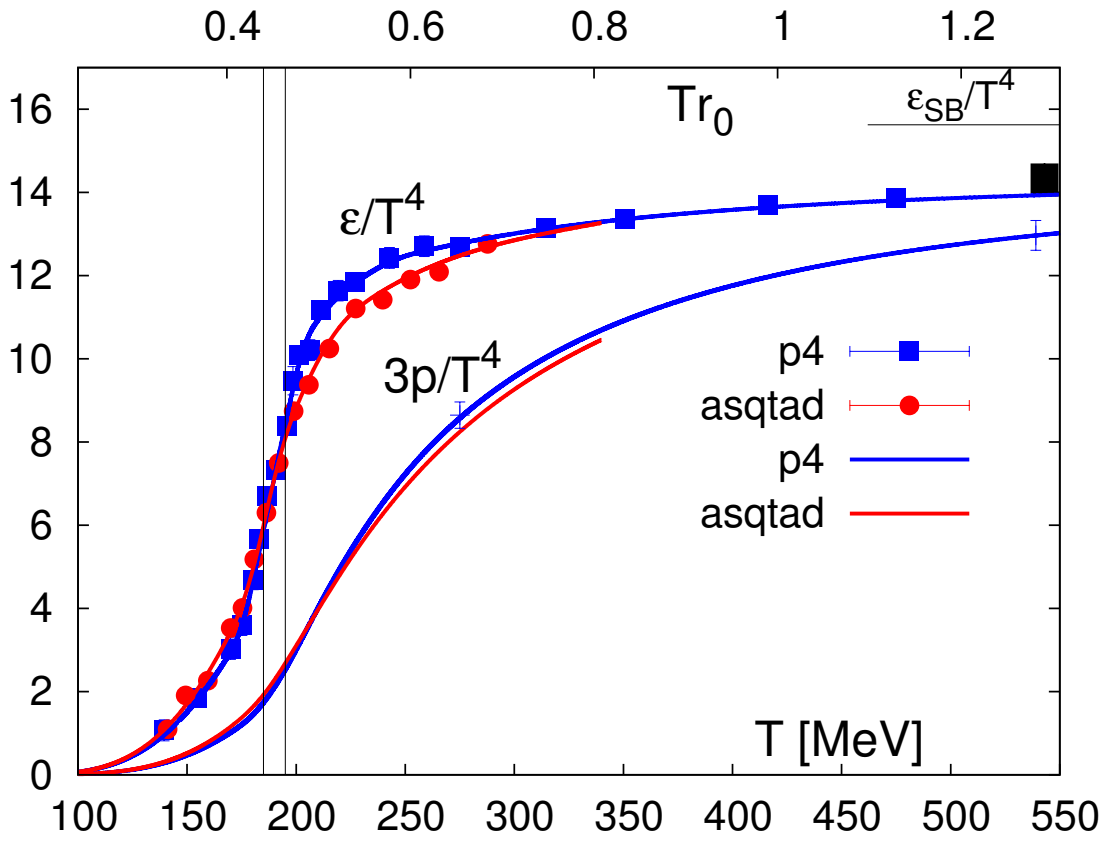

Figure 1.1: Energy density and three times the pressure as a function of temperature, calculated from lattice QCD with asqtad and p4 action [34].

from Bazavov et al., using two different improved staggered fermion actions (the asqtad and p4 action, respectively) [34]. They found that both deconfinement and chiral symmetry restoration happen in a narrow temperature region: 185 MeV $< T_c <$ 195 MeV, one finds that the lattice EOS approaches 85-90% of the Stefan-Boltzmann limit for an ideal non-interacting QGP gas. But this does not necessarily mean that the QGP is already weakly coupled there. From the EOS alone, lattice QCD simulations can not distinguish a weakly coupled QGP from a strongly coupled QGP. Indeed, the concept of a strongly coupled QGP, which behaves like an almost perfect liquid with very low viscosity [36–39], came from the strong collective flow observed in RHIC experiments and its very successful descriptions by ideal hydrodynamics [6, 7]. However, why the QGP is strongly coupled at RHIC energies is still a theoretical challenge and it is also unknown whether the QGP created in the future LHC experiments will continue to be a strongly coupled liquid or behave more like a weakly coupled gas.

1.1.2 QGP signatures

Physicists have long thought that a new state of matter could be reached if the short range repulsive forces between nucleons could be overcome and if squeezed nucleons would merge into one another. Present theoretical ideas provide a more precise picture for this new state of matter: it should be a quark-gluon plasma (QGP), in which quarks and gluons, the fundamental constituents of matter, are no longer confined within the dimensions of the nucleon, but free to move around over a volume in which a high enough temperature and/or density prevails [40]. The quarks and gluons that spill out of a proton collision tend to have nothing but empty space around them. In a heavy ion collision, the large number of nucleons that are broken apart at once means that, instead of flying into empty space, a given quark or gluon will have the opportunity to interact with those pouring out of nearby nucleons. As a result, for a brief instant, the collisions don't look much like an explosion; instead, it looks more like the boundaries between nucleons melting, leaving behind a sea of quarks and gluons that are interacting [41]. Some of the experiments use multipurpose detectors to measure simultaneously and correlate several of the more abundant observables. Others are dedicated experiments to detect rare signatures with high statistics [40]. Positive identification of the quark-gluon plasma state in relativistic heavy ion collisions is, however, extremely difficult. If created, the QGP state would have only a very transient existence. Due to color confinement, a well-known property of strong interactions at low energies, single quarks and gluons cannot escape from the collision – they must always combine to color-neutral hadrons before being able to travel to the detector. This process is called "hadronization": long after which 99.9% of detected particles are hadrons thus, evidence for or against formation of an initial state of deconfined quarks and gluons at the SPS thus must be extracted from a careful and quantitative analysis of the observed final state [40].

Many hadronic observables show a strong nonlinear dependence on the number of nucleons which participate in the collision. Models based on hadronic interaction mechanisms have consistently failed to simultaneously explain the wealth of accumulated data. On the other hand, the data exhibit many of the predicted signatures for a quark-gluon plasma. Even if a full characterization of the initial collision stage is presently not yet possible, the data provide strong evidence that it consists of deconfined quarks and gluons [40]. There has been many signature analysis eventhough, none of these signatures allow individually to prove QGP formation, as they are contaminated by the dynamical evolution of the fireball through various stages, usually from the very early pre-equilibrium stage through (perhaps) a QGP phase to the late hadronic stage. From the many methods the following are well traced: collective flow [4–7], strangeness enhancement [8, 9], charmonium suppression [10,11], thermal photon and dilepton emission [12,13], jet quenching [14–17], critical fluctuations [18], Bose-Einstein interferometry and others.

However, The combination of three observations at RHIC, that finally convinced the community that the QGP has been successfully created, were the measurements of **strong anisotropic collective flow**, **valence quark number scaling of the elliptic flow** v_2 , and **jet quenching** [21]. This led to the announcement in 2005 that the QGP had been discovered at RHIC [20, 22, 37, 38]. Let's have a dive in the three very valueble observations and finally one experimental tool.

Elliptic flow:

One of the main discoveries at RHIC was that such a matter has a very low shear viscosity to entropy density ratio $\eta/s = 1/4\pi$ [42, 43]. The first and principal observable that has been extensively used for extracting such information from heavy ion collisions is the collective flow of various particles, specially the elliptic flow [44–48]. It is a measure of the anisotropy in the angular distribution of the emitted particle. It corresponds to the second Fourier coefficient in the transverse momentum distribution [49] and describes the eccentricity of an ellipse-like distribution, i.e., $v_2 > 0$ indicates in-plane enhancement, $v_2 < 0$ characterizes the squeeze-out perpendicular to the reaction plane, and $v_2 = 0$ shows an isotropic distribution in the transverse plane.

When analyzed quantitatively by means of hydrodynamical simulation [6], it has been found that the amount of $v_2(p_T)$ observed is nearly consistent with the one of a perfect fluid, while an advanced analysis by means of viscous hydrodynamics [50, 51] or transport kinetic theory both confirm that the data on v_2 at RHIC and LHC are consistent with an average $4\pi\eta/s$.

Taking the beam direction along the $z-$axis and the reaction plane on the $x-z$ plane, the elliptic flow is then determined from the average difference between the square of the x and y components of particle transverse momentum, i.e.,

$$v_2 = \langle cos(2\,\varphi_p)\rangle = \left\langle \frac{p_x^2 - p_y^2}{p_x^2 + p_y^2} \right\rangle = \langle \cos(2\phi_p)\rangle \equiv \frac{\int d\phi_p \, \cos(2\phi_p) \, \frac{dN}{dy\, p_T dp_T\, d\phi_p}}{\int d\phi_p \, \frac{dN}{dy\, p_T dp_T\, d\phi_p}} \,, \tag{1.2}$$

where $\frac{dN}{dy\, p_T dp_T\, d\phi_p}$ is the angular distribution of the transverse momentum (p_T) dependent spectra, and $y = \frac{1}{2}\ln[(E + p_L)/(E - p_L)]$ is the rapidity of the particles. The hadron momentum spectra, their angular distribution (flow patterns) and the particle yield ratios are primary observables for the bulk medium created in heavy ion collisions. One of the main discoveries of RHIC is that the medium displays strong collective. In the language of hydrodynamics, the collective flow is driven by pressure gradients, thus providing access to the equation of state (EOS) of the medium. Whereas the azimuthally averaged radial flow receives contributions from all expansion stages, the anisotropic "elliptic" flow seen in non-central collisions is generated mostly

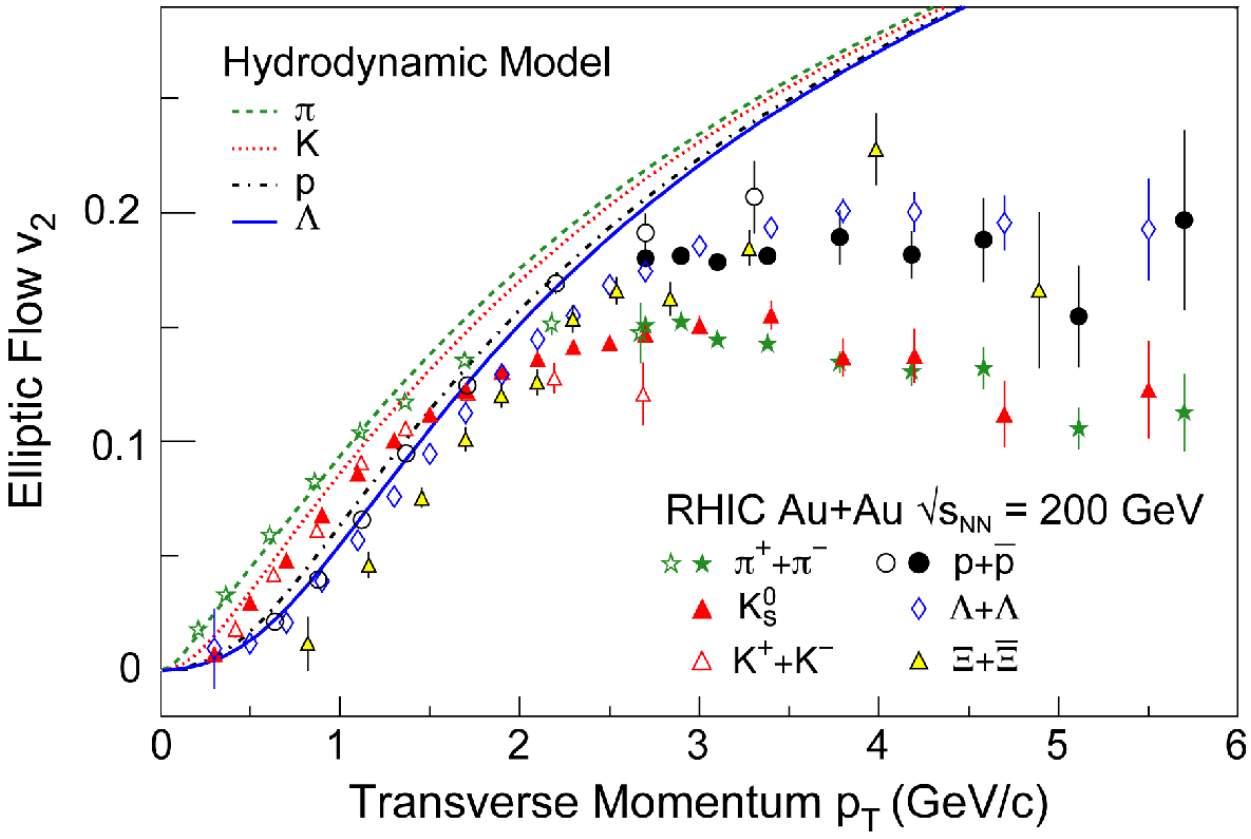

Figure 1.2: Elliptic flow v_2 for different hadron species [52,53], plotted as a function of transverse momentum, compared with ideal hydrodynamics predictions [54].

during the hot early stage, and thus provides the information about the QGP phase, namely its thermalization and its EOS [6, 7].

Fig 1.2 compares the experimental elliptic flow data $v_2(p_T)$ with ideal hydrodynamic predictions [52,53]. For $p_T < 1.5$ GeV, where most (more than 98%) of the particles are produced, ideal hydrodynamics shows excellent agreement with the experimental data and correctly predicts the observed splitting for different hadron species. This strongly indicates that the bulk of the matter is strongly coupled and behaves like an almost perfect fluid [20].

For a successful description of the RHIC data, especially for the elliptic flow, ideal hydrodynamic requires a fast thermalization of the system, which must happen on a time scale of about 0.6 fm/c [36]. Around that time, the early matter has a peak temperature of $\sim$ 350 MeV – about twice the QGP phase transition temperature. Although this gives indirect evidence for QGP formation, the success of ideal hydrodynamics is primarily evidence for the formation of a *thermalized* new form of matter at $T \sim 2T_c$ [36–38].

Quark degrees of freedom and partonic collectivity:

Understanding partonic recombination is crutial in explaining the prior nature of the system which is the QGP. This started back in 1977 when two competing papers appeared trying to model the hadronization process in high energy elementary collisions. The initial Feynman/Fields paper describes the hadronization process in vacuum through jet fragmentation [55]. This approach was later on extended to string fragmentation. The other paper was by Das and Hwa [56] and it tried to describe hadronization through recombination or coalescence of independent free quarks which is modeled through a momentum overlap probability function. There is no explicit hadronization mechanism in both cases, but the particle emission spectra are described well by the recombination approach. This model has been the basis for many recent recombination models used in heavy ion collisions (e.g. [57, 58]). The success of the statistical model in analyzing of the measured hadron abundances gives additional evidence for the QGP phase transition. Particle ratios including a large number of hadron species are well described by a thermal model with just two parameters, T and μ, yielding a chemical freeze-out temperature $T_{ch} = 160 - 170$ MeV, which is approximately equal to the QCD phase transition temperature as determined by lattice QCD simulations. This strongly indicates that hadrons are born during the QGP to hadron phase transition, and that flavor changing interactions (from inelastic collisions) quickly cease right after the phase transition [59].

The intermediate transverse momentum region of the measured spectra has revealed a scaling, the so-called constituent quark scaling, which can be interpreted as evidence for not only deconfinement but also quark recombination so, direct evidence for quark degrees of freedom in the newly formed matter can be extracted from detailed measurements of the p_T-differential elliptic flow $v_2(p_T)$ for a large variety of mesons and baryons. This observable, shown in Fig. 1.2, shows a characteristic splitting between mesons and baryons at intermediate transverse momentum $p_T = 2 - 5$ GeV. Even though this is above the p_T range where hydrodynamics is valid, the underlying collective flow of the fireball still affects hadron production at this p_T. Baryons, which contain three valance quarks, show stronger v_2 at intermediate transverse momentum than mesons, containing only two valance quarks. This phenomenon can be well explained by the quark recombination model [60], in which collectively flowing baryons and mesons are generated by the coalescence of quarks that collectively flow with the medium. According to the recombination model, the baryon and meson elliptic flow coefficients are expressed in terms of the quark elliptic flow in the following way [59, 60]:

$$v_2^{(M)}(p_T) = 2v_2^{(q)}(p_T/2); \qquad v_2^{(B)}(p_T) = 3v_2^{(q)}(p_T/3). \tag{1.3}$$

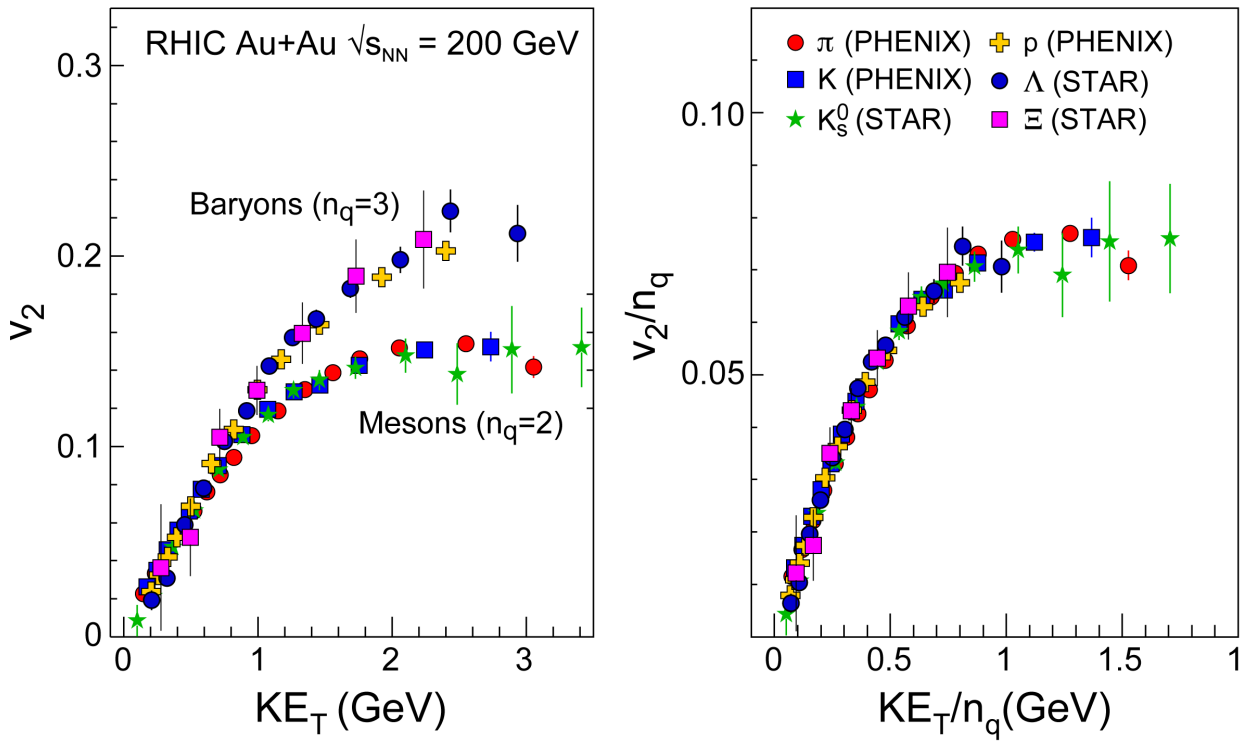

Figure 1.3: left: The transverse kinetic energy KE_T dependence of v_2 for various hadron species. Mesons and baryons fail to different universal curves respectively. right: v_2 and KE_T are scaled by the number of valence quarks. All of the hadron species fail to the same universal curve: the differential elliptical flow per quark [59].

As the right panel in Fig. 1.3 shows, a corresponding rescaling of both v_2 and KE_T by the number of valence quark (2 for mesons and 3 for baryons) leads to a universal v_2 scaling curve for *all* hadron species. In short, the universal valence quark number scaling v_2 suggests that the collectively flowing matter directly involves quarks, and that the quark collective properties are transferred to those of hadrons by quark recombination.

Jet quenching:

Hard scatterings of incoming quarks and gluons every now and then create a pair of energetic fast partons with large transverse momentum, at the very beginning of a heavy ion collision. Each of the two fast partons will finally fragment into a spray of hadrons, forming what is called a jet. Much more precise measurements of the quark energy loss could be achieved by clustering those particles into jets to measure the quark energy very precisely. At the same time, the constituents of the jets could hold information on how the medium modifies the way quarks turn into daughter particles. The rates for such hard process are small but grow rapidly with increasing collision energy. At RHIC energies, the fast partons for the first time became

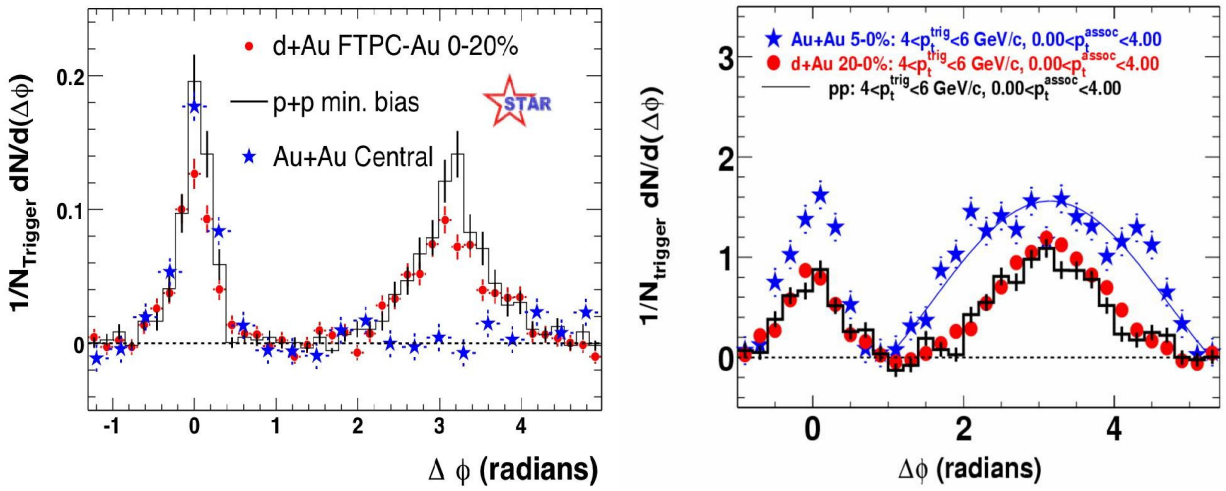

Figure 1.4: Azimuthal angular correlations between high momentum hadrons in p + p, d + Au, and central Au + Au collisions. In both cases, the trigge particle of the pair has high-momentum ($p_T > 4$GeV). Left: Associated particles recoiling with high momenta ($p_T > 2$GeV) exhibit strong suppression in Au + Au [**?**]. Right: Associated particles with low recoil momenta ($p_T > 0.15$GeV) are strongly enhanced in Au + Au collisions [53].

sufficiently abundant as useful probes for the hot medium. Their production rates are well understood, both experimentally from pp collision at the same energy or theoretically via PQCD. What makes them useful for heavy ion collisions is that, before hadronization to jets, they have to travel through the hot fireball medium formed in the collision, which modifies their initial energy and momentum [60].

Angular correlations between a high-p_T leading (trigger) hadron with other energetic hadrons provide additional strong support for the picture of significant parton energy loss in the QGP medium [15]. Energy momentum conservation requires that fast partons are always generated in pairs, moving along opposite directions in the pair center of mass frame. This leads to back-to-back correlations between the resulting jets, as shown by two peaks in the azimuthal angle correlation separated by 180^0. Such a back-to-back correlation is clearly seen in p+p and d+Au collisions (see left panel of Fig. 1.4). In central Au+Au collisions, however, one sees only one such peak in the direction of fast trigger hadron (blue stars in the left panel of Fig. 1.4). This can be understood if one assumes that the energetic parton pair is created near the surface of fireball: the near-side outgoing parton quickly escapes from the medium and fragments into the leading hadron and other softer hadrons correlated in angle with the leading hadron, while its inward-traveling partner at 180^0 loses most of its energy through interactions with the QGP medium and no longer contributes to energetic hadrons in the away-side (recoiling) direction [15]. The energy carried by the away-side fast parton is deposited in the medium, which leads to an enhancement of soft hadron production in the away-side hemisphere, as shown in the right panel of Fig 1.4. Soon, people realized that the much broadened away-side

correlations may be related to a possible collective "hydrodynamic" response of the medium to the energy and momentum deposition from the fast parton, called Mach Cone [61].

Bose-Einstein interferometry:

Hadrons created in relativistic heavy ion collision undergo many secondary interactions before escaping from the collision "fireball"and when they are finally set free, the fireball volume has expanded by about a factor 30–50; this information can be extracted from two-particle correlations between identical hadrons by a method called "Bose-Einstein interferometry". At this point, the relative abundances and momentum distributions of the hadrons still contain important memories of the dense early collision stage which can be extracted by a comprehensive analysis of the hadronic final state [40]. A combined analysis of ore than 20 different hadron species momentum distributions and two-particle correlations shows that, at the point where they stop interacting and "freeze out", the fireball is in a state of tremendous explosion, with expansion velocities exceeding half the speed of light, and very close to local thermal equilibrium at a temperature of about 100-120 MeV. This characteristic feature gave rise to the name "Little Bang". The observed explosion calls for strong pressure in the earlier collision stages. Recently measured anisotropies in the angular distribution of the momenta perpendicular to the beam direction (NA49, NA45, WA98) indicate that the pressure was built up quickly, pointing to intense rescattering in the early collision stages.

1.2 The goal

Understanding the Quark Gluon Plasma, whose existence was known from the combination of three observations, is the central goal of high energy heavy ion collision physics. The compelling observations came from studying elliptic flow which is a measure of how the energy, momentum and number of created particles are not uniform with direction. So, any elliptic flow related study has the chance to clear the road of understanding QGP well, and answering what affects elliptic flow is part of the journey. The main goals of this PhD work relies on : investigating the evolution of electromagnetic field in relativistic heavy ion collision, Calculating the drift velocity that arises from the field and evaluating its effect on the net flow of identified particles.

1.3 Outline

This thesis focuses on calculation of the electromagnetic field created by a system of relativistic heavy ion collision and investigation of the change it brings to the final flow of those particles. Chapter 2 explains the

basics of heavy ion collision. Chapter 3 has dedicated it self in explaining about the flow harmonics. Chapter 4 Explains the governing principles behind the electromagnetic fields created in the reaction. Chapter 5 Develop the model set-up used and explains about the routines used to make the calculations. The results are presented and analyzed in Chapter 6 and finally Our conclusions are summarized in Chapter 7.

Chapter 2: The Basics of Heavy Ion Collision

2.1 Introduction

Quarks and gluons make up protons and neutrons found in the nucleus of every atom in the universe. At heavy ion colliders like RHIC and the LHC, scientists can create matter more than 100,000 times hotter than the center of the sun (2TK) so hot that protons and neutrons melt into a plasma of quarks and gluons. The particle collisions and emerging quark-gluon plasma hold keys to understanding how these fundamental particles interact with each other, which helps explain how everything is held together from atomic nuclei to human beings to the biggest stars how all matter has mass, and what the universe looked like microseconds after the Big Bang [62]. This is why we are smashing heavy ions, to understand the femtoscopic world. But what are heavy ions? Heavy ion, in nuclear physics, is any particle with one or more units of electric charge and a mass exceeding that of the helium-4 nucleus (alpha particle). Special types of accelerators are capable of producing fairly intense, high-energy beams of heavy ions.

2.2 Event Characterization

Heavy-ions are extended objects and the system created in a head-on collision is different from that in a peripheral collision. To study the properties of the created system, collisions are therefore categorized by their centrality. Theoretically the centrality is defined by the impact parameter **b** (see Fig. 2.1) which, however, cannot be directly observed. Experimentally, the collision centrality can be inferred from the measured particle multiplicities, given the assumption that the multiplicity is a monotonic function of **b**.

The centrality is then characterized by the fraction, $\pi b^2/\pi(2R_A)^2$, of the geometrical cross-section with R_A the nuclear radius (see Fig. 2.2).

Instead of by impact parameter, the centrality is also often characterized by the number of participating nucleons (nucleons that undergo at least one inelastic collision) or by the number of equivalent binary collisions. Phenomenologically it is found that the total particle production scales with the number of participating nucleons whereas hard processes scale with the number of binary collisions. These measures

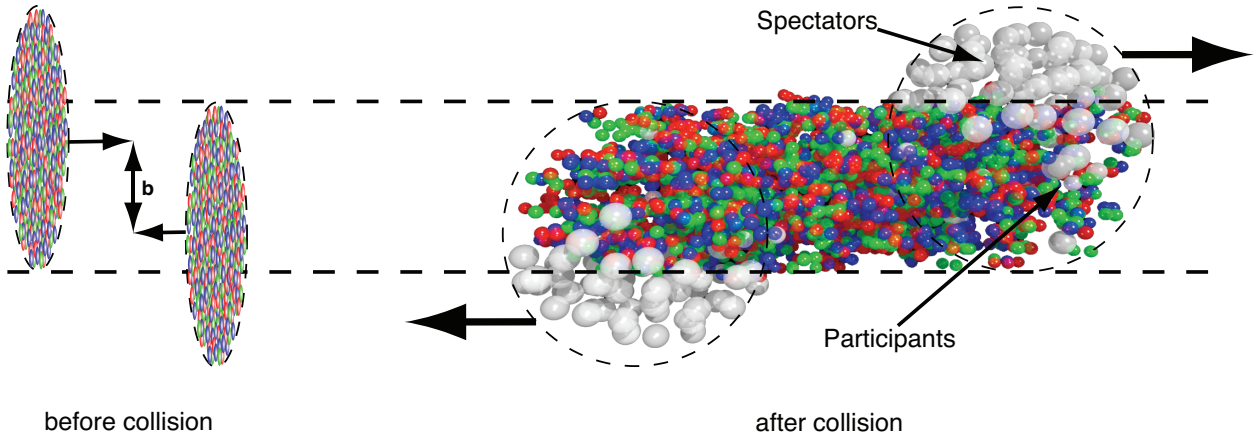

Figure 2.1: Left: The two heavy-ions before collision with impact parameter **b**. Right: The spectators continue unaffected, while in the participant zone particle production takes place.

can be related to the impact parameter **b** using a realistic description of the nuclear geometry in a Glauber calculation, as is shown in Fig. 2.2b. This Figure also shows that Pb–Pb collisions at 2.76 TeV and Au-Au at 0.2 TeV have a similar distribution of participating nucleons. The number of binary collisions increases from Au–Au to Pb–Pb by about 50% because the nucleon-nucleon inelastic cross section increases by about that amount at the respective center of mass energies of 0.2 and 2.76 TeV.

2.3 Energy Domains

Obviously the energy range about which we have presented here involves very different collision processes and concentrate on the features that are common to the whole heavy ion research; specially on collective phenomena in heavy ion reactions considered in our model setup described in chapter 5. From the physical point of view the energy region can be divided into three main regions: The intermediate energy heavy ion reactions, relativistic energy heavy ion reactions and ultra-relativistic heavy ion reactions.

2.3.1 Intermediate energy reactions

This is the energy region where the properties of hot nuclear matter can be studied around the normal nuclear density. The corresponding beam energies are in the range of 10-100 A.MeV. In this region of the thermodynamic variable space there is an interesting phenomenon the nuclear liquid-gas phase transition. At low excitations the nuclear matter is bound due to the attractive nuclear interaction. In an intermediate energy heavy in collision we may compress the nuclear matter initially and heat up the matter to 10-20

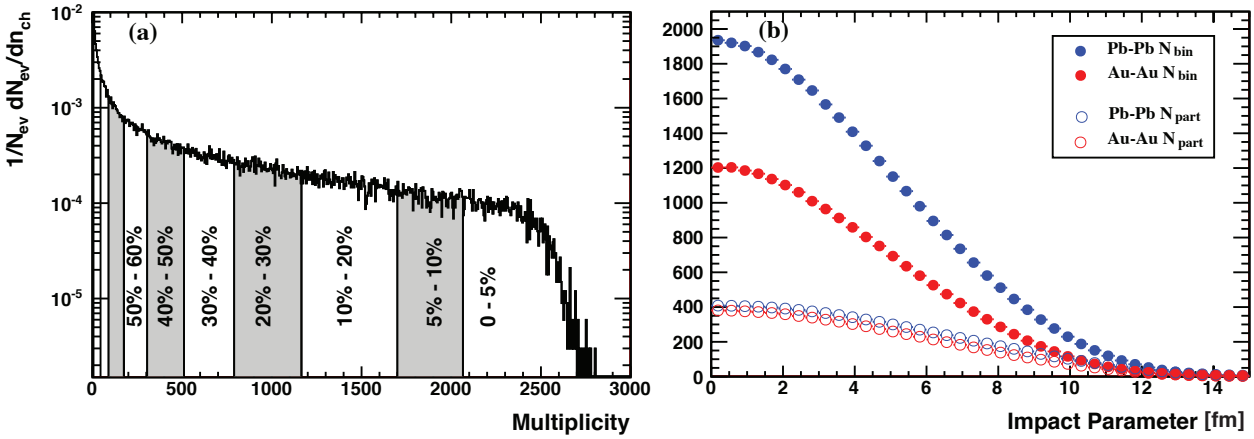

Figure 2.2: a : Charged particle distribution from Pb-Pb collisions at 2.76 TeV measured with ALICE, showing a classification in centrality percentiles (from [68]). b : Number of participating nucleons and binary collisions versus impact parameter for Pb-Pb and Au-Au collisions at 2.76 TeV and 0.2 TeV, respectively.

MeV. This matter then expands nearly adiabatically to densities below the normal nuclear density and to a smaller temperature, 5-10 MeV. Due to the attractive interaction in this final state smaller nuclear fragments are formed, the nuclear vapor is condensed to form droplets of nuclear liquid. This is the nuclear multi-fragmentation. If the collision energy is low enough the effects of the phase transition, for example critical phenomena, can be studied. The accelerators doing research in this energy domain are for example the NSCL at Michigan State University, UNILAC and SIS at GSI in Darmstadt Germany, GANIL in Caen France, CELSIUS in Uppsala Sweden and others [69].

2.3.2 Relativistic heavy ion reactions

In this energy range, 100 A.MeV - 10 A.GeV, the nuclear matter is compressed and heated more than at lower beam energies. Here mainly the compressibility and other basic properties of the nuclear EOS and nuclear interactions can be tested. The results in this energy range have astrophysical relevance to neutron stars and supernova explosions. This is the area where the research is most developed and real quantitative questions on the nuclear incompressibility, transport coefficients, in medium cross sections, momentum dependence of the nucleon-nucleon interaction, etc., are studied. Collective processes are well established both experimentally and theoretically, such as different collective flow patterns. The most dominant is the collective sidewards flow in the reaction plane which is used as a tool to extract the EOS and transport properties of nuclear matter. This energy range is studied at some of the accelerators mentioned above and

at some others like the BEVALAC at LBL in Berkeley, the heavy ion accelerator in Dubna, SATURN in Saclay France [69].

2.3.3 Ultra-relativistic heavy ion reactions

This energy region starts around 10 A.GeV beam energy and the most intriguing physics question is the search for Quark Gluon Plasma. The most optimistic theoretical estimates allow QGP formation already at 10 A.GeV. The ultra-relativistic domain can be separated into two regimes with essentially different physics: the stopping region where baryons stemming from the projectile and the target are fully or partly stopped by each other, forming a fairly baryon rich matter in the middle of the reaction zone, and the transparent region where initial target and projectile baryons are so far apart in the phase space that the heavy ion collision cannot slow them down completely. The boundary between these two regions is not very sharp and experimentally not known yet.

An ultrarelativistic heavy-ion collision (URHIC) of two (identical) Lorentz-contracted nuclei is thought to proceed as follows. Each incoming nucleus can be looked upon as a coherent [71] cloud of partons (more precisely, a colour-glass-condensate (CGC) plate [72]). The collision results in shattering of the two CGC plates. A significant fraction of the incoming kinetic energy is deposited in the central region leading to a high-energy-density fireball (more precisely, a highly non-equilibrium state called glasma [72]). This is still a coherent state and liberation of partons from the glasma takes a finite amount of (proper) time (a fraction of a fm/c). Subsequently collisions among partons lead to a nearly thermalized (local thermalization!) state called QGP. This happens at a time of the order of 1 fm/c — a less understood aspect of the entire process. Due to near thermalization, the subsequent evolution of the system proceeds as per relativistic imperfect fluid dynamics. This involves expansion, cooling, and dilution. Eventually the system hadronizes. Hadrons continue to collide among themselves elastically which changes their energy-momenta, as well as inelastically which alters abundances of individual species. Chemical freezeout occurs when inelastic processes stop. Kinetic freezeout occurs when elastic scatterings too stop. These late stages of evolution when the system is no longer in local equilibrium are simulated using the relativistic kinetic theory framework. Hadrons decouple from the system approximately 10-15 fm/c after the collision and travel towards the surrounding detectors. From the volume of experimental data thus collected one has to establish whether QGP was formed and if so, extract its properties [73].

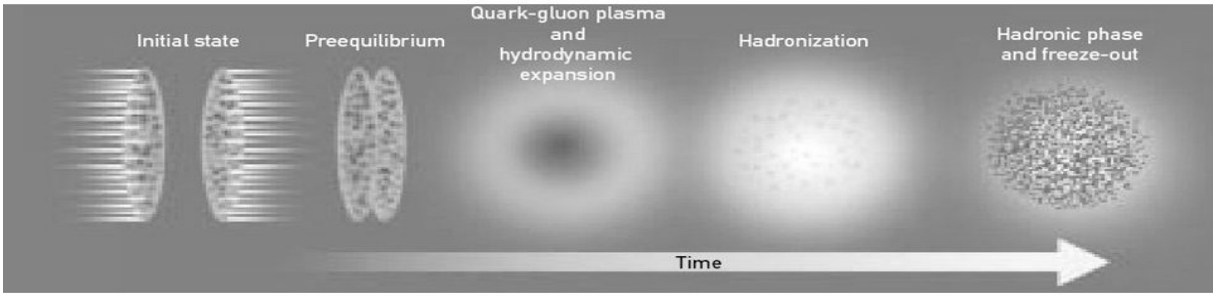

Figure 2.3: Different stages for relativistic heavy ion collisions [74].

2.4 Stages of Heavy Ion Collision

The different stages for an ultra-relativistic heavy ion collision are schematically illustrated in Fig 2.3 and 2.4. The initial stage before the collision is followed after impact by a pre-equilibrium stage, an expanding QGP and hadron resonance gas (HRG) stage and a final freeze-out/decoupling stage [40] explained in detail as follows:

1. Initial stage at $\tau < 0$: Two Lorentz contracted heavy nuclei approach each other with more than 99.9% of the speed of light. At sufficiently high collision energy (possibly reached at RHIC), this initial stage can be described by dense gluon walls known as the Color Glass Condensate (CGC). Because of the fluctuation of the moving charge gluon field, this is one of the list understood stage.

2. Pre-equilibrium stage and thermalization: The energetic collision of the two heavy nuclei excites the QCD vacuum and produces a dense pre-equilibrium matter consisting of quarks, anti-quarks and gluons. It takes around 1 fm/c for the pre-equilibrium bulk matter to achieve local thermalization and form the quark-gluon plasma. In this very early pre-equilibrium stage, the primary collisions between fast partons inside the colliding nuclei also generate "hard probes" with either large mass or large transverse momentum, such as heavy quark pairs ($c\bar{c}$ and $b\bar{b}$), pre-equilibrium real or virtual photons, and very energetic quarks and gluons with large transverse momentum (from which jets are formed after hadronization).

3. QGP expansion and hadronization: After thermalization, the quark-gluon plasma (QGP), driven by thermal pressure gradients, expands and cools down very quickly. After reaching the critical temperature $T_c \simeq 170$ MeV, it hadronizes and turns into hadronic matter, consisting of a mixture of stable and unstable hadrons and hadron resonances. Hadronization happens continuously at the edge of the

QGP fireball during the whole QGP expansion period. In central Au+Au collisions at RHIC, it takes around 10 fm/c for the QGP fireball to expand and fully convert to hadronic matter.

4. Hadronic expansion and decoupling: The hadronic matter continues to expand until the system becomes very dilute. Then individual hadrons decouple from the system (kinetic freeze-out) and free-stream to the detector. Like the QGP hadronization process, the hadronic decoupling happens continuously at the edge of the fireball, where the density is low. After complete hadronization, it takes another $5 - 10$ fm/c for the hadronic matter to completely freeze-out.

2.5 Theory

There does not exists a unique theoretical tool to describe the whole heavy ion collision process from the very beginning till the end. The different energy and time scales during different collision stages imply dramatic changes of the effective physical degrees of freedom and their interactions, which thus require different tools for their description. A complete description requires matching these tools to each other, generating so-called hybrid approaches. Nevertheless, all the equations are Energy-momentum conservation given the initial conditions, viscosity and the equation of states. The theory tools to be used in the different stages, Fig2.5, was plotted by song 20 plus years ago which are yet to be fully developed in detail.

Color Glass Condensate: At very high collision energies, particle production at mid rapidity probes the nuclear structure functions in the small-x regime (x is the fraction between parton momentum and beam momentum). It is well known that the gluon distribution function $xG(x, Q^2)$ increases dramatically with decreasing of x, for large enough probe resolution Q^2. When the gluon density becomes high enough, two

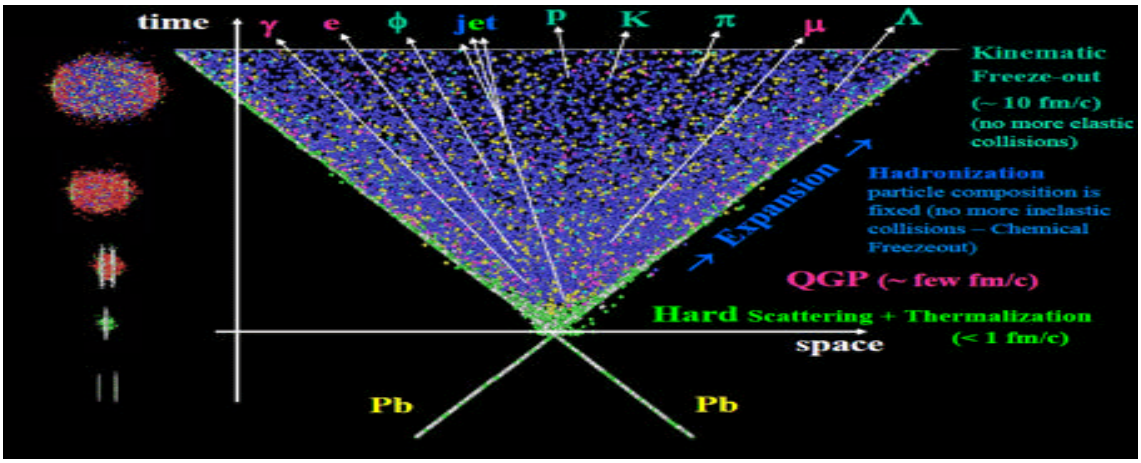

Figure 2.4: The space-time picture of a heavy ion collision [60].

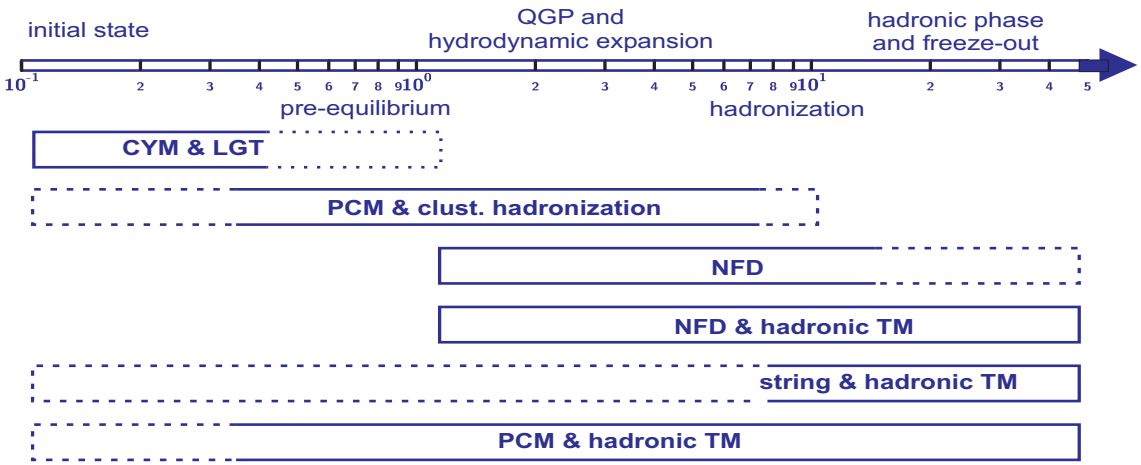

Figure 2.5: Theory tools for RHIC and their range of applicability [6, 7, 75, 76, 82, 99].

gluons start to recombine to one. This leads to gluon saturation below some momentum scale Q_s^2. At this momentum scale, each gluon mode has macroscopic occupation number $\sim \frac{1}{\alpha_s}$, which is why this state has been called a condensate. These small-x gluons are generated by radiation corrections from gluons at large x, whose natural evolution time scale is Lorentz dilated. This time dilation is transferred to the small-x degrees of freedoms, making them evolve very slowly compared to other natural time scales: their behavior is "glassy". Considering these factors, together with the color nature of gluons, this initial stage has been named Color Glass Condensate (CGC) [75, 76, 88]. The production of the pre-equilibrium secondary soft gluons is related to breaking the phase coherence in this initial CGC wave function [77].

Parton cascade model: After the initial parton production, one needs to describe the pre-equilibrium stage and its thermalization. For dilute systems with incoherent parton configurations, the classical motion of on-shell partons can be described by the Parton Cascade Model (PCM) [**?**, **?**, **?**], which solves the Boltzmann equation with a leading order PQCD collision term. Initially, the PCM was assumed to work for the pre-equilibrium stage, the subsequent thermalization period and the succeeding QGP expansion stage. However, the typical thermalization time obtained from PCM with 2-body ($gg \leftrightarrow gg$) PQCD scattering cross sections is of the order of 5 fm/c [**?**], which is too long for the fast thermalization (< 1 fm/c) required by RHIC data [36, 70]. The recent development of a PCM with $2 \leftrightarrow 3$ ($gg \leftrightarrow ggg$) processes leads to faster thermalization and indeed reproduces the large observed elliptic flow [**?**, **?**]. However, it is applied to a dense system, which creates tension with the assumptions under which the Boltzmann equation is valid. In a very dense system (such as the very early pre-equilibrium stage at RHIC and LHC energies) the partons scatter so frequently that they are no longer on shell. To treat partons with off-shell energies requires the use of

quantum transport theory. The theoretical framework for quark-gluon quantum transport was developed by Heinz more than 20 years ago [78–81], but its numerical demands are exorbitant, and it has not yet been implemented numerically.

Thermalization: The formation of the quark gluon plasma requires two aspects: local equilibrium (thermalization) and local momentum isotropy. Generally, it is believed that the system achieves momentum isotropy before completing thermalization, which is assumed to happen at a time scale of ~ 0.6 fm/c at RHIC energies as indicated by the validity of ideal hydrodynamic simulations [36,70]. Elucidating the mechanism for fast isotropization and thermalization has been a theoretical challenge. Although much progress has been made during the past years, the thermalization mechanism is still not fully understood. Recently, people realized that the Weibel instability, which is known from traditional electromagnetic plasmas, might help to understand the fast isotropization and thermalization of the QGP The presence of a Chromo-Weibel instability in the early parton plasma, which is characterized by strong momentum anisotropies, has been confirmed by numerical simulations in 1+1-dimensional and 3+1-dimensional hard thermal loop effective theory and in a 3+1-dimensional expanding Glasma. However, non-Abelian saturation effects temper the exponential growth of the Chromo-Weibel instability, leading to significantly larger time scales even for isotropization than those required for the fast thermalization approximately observed at RHIC [100, 101].

Hydrodynamics: If thermalization is achieved and can be locally maintained during the subsequent expansion, the further evolution of the QGP and hadronic matter can be described by hydrodynamics [99]. Hydrodynamics is a macroscopic approach which describes the system by macroscopic variables, such as local energy density, pressure, temperature and flow velocity. It requires knowledge of the equation of state, which gives a relation between pressure, energy and baryon density, but no detailed knowledge of the microscopic dynamics. The simplest version is ideal hydrodynamics [6,7], which totally neglects viscous effects and assumes that local equilibrium is always perfectly maintained during the fireball expansion. Microscopically, this requires that the microscopic scattering time is very much shorter than the macroscopic expansion (evolution) time and that the mean free path is much smaller than the system size. If this is not satisfied, viscous effects come in, and one can apply viscous hydrodynamics as long as the deviation from equilibrium remains small. If the system is far away from equilibrium, one has to switch to a kinetic theory approach, such as parton or hadron cascade models [60].

Hadron cascade model and hybrid approaches: The hadron cascade model [82], which solves the Boltzmann equation for a variety of hadron species with flavor-dependent cross-sections, is a successful tool

to describe the hadronic matter created at AGS and SPS energies. At these collision energies, the hadron cascade model is initialized by a superposition of hadrons and hadronic strings, produced in the primary nucleon-nucleon collisions. At RHIC energies and above, hybrid approaches that combine a parton cascade model or hydrodynamics with a hadron cascade, provide a "unified" description of the evolution of the QGP and the succeeding hadronic matter. However, some caution must be taken for the transition between the models. Parton + hadron cascade hybrids must deal with the problem of converting partons to hadrons without violating the second law of thermodynamics (i.e. without losing entropy), and they have difficulties to incorporate the change in the structure of the QCD vacuum during the phase transition. Hydrodynamics + hadron cascade hybrids can more easily accommodate these, by employing a realistic EOS from lattice QCD. One generally stops hydrodynamics at a switching temperature slightly below T_c, converting the fluid to hadrons using a Cooper-Frye prescription for phase-space distributions to generate (via Monte-Carlo) initial momentum and spectra profiles for the hadron cascade simulations. However, this procedure can not deal with a potential feed-back from cascade hadrons to the hydrodynamics fluid along space-like parts of the matching freeze-out hypersurface [60].

2.6 Parameters and Observables to deal with

As explained above, heavy ion collision is a multistage system which needs and should consider different physical parameters in every step of the stages. Everything we give-in affects the very outputs. Whether we deal with experiment or theory the initial conditions we choose to use, matters. some of the parameters to be considered includes: the Gluon fields of the flying particles, the viscosity, entropy, temperature, equation of state with the right pressure and energy density distribution, number of nucleons, beam energy, impact parameters, eccentricity and many more.

Equation of state: An equation of state (EOS) is a nontrivial relation between thermodynamic variables characterizing a medium. While the term is used in a singular form in nuclear physics, actually different relations are of interest, such as between pressure, baryon density , and temperature, between P, chemical potential and temperature, or between energy per baryon and baryon density and temperature, etc. Some of the possible relations are fundamental under certain conditions, meaning that all remaining relations under those conditions may be derived from them.

2.7 Fluid Dynamics

2.7.1 Non-relativistic fluid dynamics

Fluid dynamics is one of the oldest and most successful theories in modern physics. In its non-relativistic form, it is intuitively understandable due to our everyday experience with hydrodynamics, or the dynamics of water [83]. The degrees of freedom for an ideal, neutral, uncharged, one-component fluid are the fluid velocity $\vec{v}(t, \vec{x})$, the pressure $p(t, \vec{x})$, and the fluid mass density $\rho(t, \vec{x})$, which are linked by the fluid dynamic equations.

The movement of fluid in the physical domain is driven by various properties. For the purpose of bringing the behavior of fluid flow to light and developing a mathematical model, those properties have to be defined precisely as to provide a transition between the physical and the numerical domain. Velocity, pressure, temperature, density, and viscosity are the main properties that should be considered simultaneously when conducting a fluid flow examination. In accordance with the physical phenomena such as combustion, multiphase flow, turbulence, mass transport, etc., those properties diversify enormously and can be categorized into kinematic, transport, thermodynamic, and other miscellaneous properties1.

Thermo-fluid incidents directed by governing equations are based on the laws of conservation. The Navier-Stokes (N-S) equations is the broadly applied mathematical model to examine changes on those properties during dynamic and/or thermal interactions. The equations are adjustable regarding the content of the problem and are expressed based on the principles of conservation of mass, momentum, and energy:

- Conservation of Mass: Continuity Equation.
- Conservation of Momentum: Newton$'s$ Second Law
- Conservation of Energy: First Law of Thermodynamics or Energy

These equations are thought to govern the motion of all fluids; they thus are essential to the physics of continuum mechanics. Practically every area of science that makes macroscopic approximations at least touches on fluid dynamics from cosmology and the motion of galaxies to nuclear fusion and the confinement of plasma, from electrodynamics and the flow of charges to aerospace engineering and the design of airplanes, the Navier-Stokes equations are vital to the understanding of the universe. Yet, it is not known whether physically realistic smooth solutions are guaranteed to exist on all of $|R^3$. [84], [85]

,

$$\partial_t \vec{v} + \left(\vec{v}\cdot\vec{\partial}\right)\vec{v} = -\frac{1}{\rho}\vec{\partial}p\,, \tag{2.1}$$

$$\partial_t \rho + \rho\,\vec{\partial}\cdot\vec{v} + \vec{v}\cdot\vec{\partial}\rho = 0\,. \tag{2.2}$$

These equations are referred to as "Euler equation" (2.1) and "Continuity equation" (2.2), respectively, and typically have to be supplemented by an equation of state $p = p(\rho)$ to close the system. For non-ideal fluids, where dissipation can occur, the Euler equation generalizes to the "Navier-Stokes equation" [86,87], [85]§15,

$$\frac{\partial v^i}{\partial t} + v^k\frac{\partial v^i}{\partial x^k} = -\frac{1}{\rho}\frac{\partial p}{\partial x^i} - \frac{1}{\rho}\frac{\partial \Pi^{ki}}{\partial x^k}\,, \tag{2.3}$$

$$\Pi^{ki} = -\eta\left(\frac{\partial v^i}{\partial x^k} + \frac{\partial v^k}{\partial x^i} - \frac{2}{3}\delta^{ki}\frac{\partial v^l}{\partial x^l}\right) - \zeta\,\delta^{ik}\frac{\partial v^l}{\partial x^l}\,, \tag{2.4}$$

where Latin indices denote the three space directions, e.g. $i = 1, 2, 3$. The viscous stress tensor Π^{ki} contains the coefficients for shear viscosity, η, and bulk viscosity, ζ, which are independent of velocity. The non-relativistic Navier-Stokes equation is well tested and found to be reliable in many applications, so any successful theory of relativistic viscous hydrodynamics should reduce to it in the appropriate limit.

2.7.2 Relativistic ideal fluid dynamics

For a relativistic system, the mass density $\rho(t, \vec{x})$ is not a good degree of freedom because it does not account for kinetic energy that may become sizable for motions close to the speed of light. Instead, it is useful to replace it by the total energy density $\epsilon(t, \vec{x})$, which reduces to ρ in the non-relativistic limit. Similarly, $\vec{v}(t, \vec{x})$ is not a good degree of freedom because it does not transform appropriately under Lorentz transforms. Therefore, it should be replaced by the Lorentz 4-vector for the velocity,

$$u^\mu \equiv \frac{dx^\mu}{d\mathcal{T}}, \tag{2.5}$$

where Greek indices denote Minkowski 4-space, e.g. $\mu = 0, 1, 2, 3$ with metric $g_{\mu\nu} = \mathrm{diag}(+, -, -, -)$ (the same symbol for the metric will also be used for curved spacetimes). The proper time increment $d\mathcal{T}$ is given by the line element,

$$\begin{aligned}(d\mathcal{T})^2 &= g_{\mu\nu}dx^\mu dx^\nu = (dt)^2 - (d\vec{x})^2\,,\\ &= (dt)^2\left[1 - \left(\frac{d\vec{x}}{dt}\right)^2\right] = (dt)^2\left[1 - (\vec{v})^2\right]\,,\end{aligned}$$

where here and in the following, natural units $\hbar = c = k_B = 1$ will be used. This implies that

$$u^\mu = \frac{dt}{d\mathcal{T}}\frac{dx^\mu}{dt} = \frac{1}{\sqrt{1-\vec{v}^2}}\begin{pmatrix}1\\ \vec{v}\end{pmatrix} = \gamma(\vec{v})\begin{pmatrix}1\\ \vec{v}\end{pmatrix}\ , \tag{2.6}$$

which reduces to $u^\mu = (1, \vec{v})$ in the non-relativistic limit. In particular, one has $u^\mu = (1, \vec{0})$ if the fluid is locally at rest ("local rest frame"). Note that the 4-vector u^μ only contains three independent components since it obeys the relation

$$u^2 \equiv u^\mu g_{\mu\nu} u^\nu = \gamma^2(\vec{v})\left(1-\vec{v}^2\right) = 1, \tag{2.7}$$

so one does not need additional equations when trading $\vec{v}$ for the fluid 4-velocity u^μ.

To obtain the relativistic fluid dynamic equations, it is sufficient to derive the energy-momentum tensor $T^{\mu\nu}$ for a relativistic fluid, as will be shown below. The energy-momentum tensor of an ideal relativistic fluid (denoted as $T^{\mu\nu}_{(0)}$) has to be built out of the hydrodynamic degrees of freedom, namely two Lorentz scalars (ϵ, p) and one vector u^μ, as well as the metric tensor $g_{\mu\nu}$. Since $T^{\mu\nu}$ should be symmetric and transform as a tensor under Lorentz transformations, the most general form allowed by symmetry is therefore

$$T^{\mu\nu}_{(0)} = \epsilon\left(c_0 g^{\mu\nu} + c_1 u^\mu u^\nu\right) + p\left(c_2 g^{\mu\nu} + c_3 u^\mu u^\nu\right)\ . \tag{2.8}$$

In the local restframe, one requires the $T^{00}_{(0)}$ component to represent the energy density ϵ of the fluid. Similarly, in the local rest frame, the momentum density should be vanishing $T^{0i}_{(0)} = 0$, and the space-like components should be proportional to the pressure, $T^{ij}_{(0)} = p\,\delta^{ij}$ [85] §133. Imposing these conditions onto the general form (2.8) leads to the equations

$$(c_0 + c_1)\epsilon + (c_2 + c_3)p = \epsilon, \qquad -c_0\epsilon - c_2 p = p, \tag{2.9}$$

which imply $c_0 = 0, c_1 = 1, c_2 = -1, c_3 = 1$, or $T^{\mu\nu}_{(0)} = \epsilon\, u^\mu u^\nu - p\ (g^{\mu\nu} - u^\mu u^\nu)$. For later convenience, it is useful to introduce the tensor

$$\Delta^{\mu\nu} = g^{\mu\nu} - u^\mu u^\nu. \tag{2.10}$$

It has the properties $\Delta^{\mu\nu}u_\mu = \Delta^{\mu\nu}u_\nu = 0$ and $\Delta^{\mu\nu}\Delta^\alpha_\nu = \Delta^{\mu\alpha}$ and serves as a projection operator on the space orthogonal to the fluid velocity u^μ. In this notation, the energy-momentum tensor of an ideal relativistic fluid becomes

$$T^{\mu\nu}_{(0)} = \epsilon\ u^\mu u^\nu - p\ \Delta^{\mu\nu}. \tag{2.11}$$

If there are no external sources, the energy-momentum tensor is conserved,

$$\partial_\mu T^{\mu\nu}_{(0)} = 0 \ . \tag{2.12}$$

It is useful project these equations in the direction parallel ($u_\nu \partial_\mu T^{\mu\nu}_{(0)}$) and perpendicular ($\Delta^\alpha_\nu \partial_\mu T^{\mu\nu}_{(0)}$) to the fluid velocity. For the first projection, one finds

$$\begin{aligned} u_\nu \partial_\mu T^{\mu\nu}_{(0)} &= u^\mu \partial_\mu \epsilon + \epsilon \, (\partial_\mu u^\mu) + \epsilon \, u_\nu u^\mu \partial_\mu u^\nu - p \, u_\nu \partial_\mu \Delta^{\mu\nu} \, , \\ &= (\epsilon + p) \partial_\mu u^\mu + u^\mu \partial_\mu \epsilon = 0 \ , \end{aligned} \tag{2.13}$$

where the identity $u_\nu \partial_\mu u^\nu = \frac{1}{2} \partial_\mu (u_\nu u^\nu) = \frac{1}{2} \partial_\mu 1 = 0$ was used. For the other projection one finds

$$\begin{aligned} \Delta^\alpha_\nu \partial_\mu T^{\mu\nu}_{(0)} &= \epsilon \, u^\mu \Delta^\alpha_\nu \partial_\mu u^\nu - \Delta^{\mu\alpha} (\partial_\mu p) + p \, u^\mu \Delta^\alpha_\nu \partial_\mu u^\nu \, , \\ &= (\epsilon + p) \, u^\mu \partial_\mu u^\alpha - \Delta^{\mu\alpha} \partial_\mu p = 0 \ . \end{aligned} \tag{2.14}$$

Introducing the shorthand notations

$$D \equiv u^\mu \partial_\mu, \qquad \nabla^\alpha = \Delta^{\mu\alpha} \partial_\mu \tag{2.15}$$

for the projection of derivatives parallel and perpendicular to u^μ, equations (2.13),(2.14) can be written as

$$D\epsilon + (\epsilon + p) \partial_\mu u^\mu = 0 \tag{2.16}$$

$$(\epsilon + p) D u^\alpha - \nabla^\alpha p = 0 \ . \tag{2.17}$$

These are the fundamental equations for a relativistic ideal fluid. Their meaning becomes transparent in the non-relativistic limit: for small velocities $|\vec{v}| \ll 1$ one finds

$$D = u^\mu \partial_\mu \simeq \partial_t + \vec{v} \cdot \vec{\partial} + \mathcal{O}(|\vec{v}|^2), \qquad \nabla^i = \Delta^{i\mu} \partial_\mu \simeq \partial^i + \mathcal{O}(|\vec{v}|), \tag{2.18}$$

so D and ∇^i essentially reduce to time and space derivatives, respectively. Imposing further a non-relativistic equation of state where $p \ll \epsilon$, and that energy density is dominated by mass density $\epsilon \simeq \rho$, Eq. (2.16) becomes the continuity equation (2.2), and Eq. (2.17) the non-relativistic Euler equation (2.1).

One thus recognizes the fluid dynamic equations (both relativistic and non-relativistic) to be identical to the conservation equations for the fluid's energy-momentum tensor.

2.8 Hydrodynamics

2.8.1 The Relativistic Navier-Stokes equation

In the ideal fluid picture, all dissipative (viscous) effects are by definition neglected. If one is interested in a fluid description that includes for instance the effects of viscosity, one has to go beyond the ideal fluid limit, and in particular the fluid's energy momentum tensor will no longer have the form Eq. (2.11). Instead, one writes

$$T^{\mu\nu} = T^{\mu\nu}_{(0)} + \Pi^{\mu\nu}, \tag{2.19}$$

where $T^{\mu\nu}_{(0)}$ is the familiar ideal fluid part given by Eq. (2.11) and $\Pi^{\mu\nu}$ is the viscous stress tensor that includes the contributions to $T^{\mu\nu}$ stemming from dissipation. Considering for simplicity a system without conserved charges (or at zero chemical potential), all momentum density is due to the flow of energy density

$$u_\mu T^{\mu\nu} = \epsilon\, u^\nu \longrightarrow \quad u_\mu \Pi^{\mu\nu} = 0. \tag{2.20}$$

While here this is the only possibility, for a more general system with conserved charges one can view this as a choice of frame for the definition of the fluid 4-velocity, sometimes referred to as Landau-Lifshitz frame. This can be easily understood by recognizing that in a system with a conserved charge there will be an associated charge current n^μ that can be used alternatively to define the fluid velocity, e.g. the Eckart frame $u_\mu n^\mu = n$. These choices reflect the freedom of defining the local rest frame either as the frame where the energy density (Landau-Lifshitz) or the charge density (Eckart) is at rest. Since the physics must be the same in either of these frames, one can show that charge diffusion in one frame is related to heat flow in the other frame, as done e.g. in the appendix of [90]. For other recent discussions of relativistic viscous hydrodynamics in the presence of conserved charges, see e.g. [83, 91].

Similar to the case of ideal fluid dynamics studied in section 2.7.2, the fundamental equations of viscous fluid dynamics are found by taking the appropriate projections of the conservation equations of the energy momentum tensor,

$$\begin{aligned} u_\nu \partial_\mu T^{\mu\nu} &= D\epsilon + (\epsilon + p)\partial_\mu u^\mu + u_\nu \partial_\mu \Pi^{\mu\nu} = 0\,, \\ \Delta^\alpha_\nu \partial_\mu T^{\mu\nu} &= (\epsilon + p) D u^\alpha - \nabla^\alpha p + \Delta^\alpha_\nu \partial_\mu \Pi^{\mu\nu} = 0\,. \end{aligned} \tag{2.21}$$

The first equation can be further simplified by rewriting $u_\nu \partial_\mu \Pi^{\mu\nu} = \partial_\mu \left(u_\nu \Pi^{\mu\nu}\right) - \Pi^{\mu\nu}\partial_{(\mu} u_{\nu)}$, and using the identity

$$\partial_\mu = u_\mu D + \nabla_\mu \tag{2.22}$$

as well as the choice of frame, $u_\mu \Pi^{\mu\nu} = 0$. Here and in the following the $(\ldots)$ denote symmetrization, e.g.

$$A_{(\mu} B_{\nu)} = \frac{1}{2}\left(A_\mu B_\nu + A_\nu B_\mu\right) \ .$$

Hence, the fundamental equations for relativistic viscous fluid dynamics are

$$\boxed{\begin{aligned} D\epsilon + (\epsilon + p)\partial_\mu u^\mu - \Pi^{\mu\nu}\nabla_{(\mu} u_{\nu)} &= 0 \,, \\ (\epsilon + p) D u^\alpha - \nabla^\alpha p + \Delta^\alpha_\nu \partial_\mu \Pi^{\mu\nu} &= 0 \ . \end{aligned}} \tag{2.23}$$

At this point, however, the viscous stress tensor has not been specified. Indeed, much of the remainder of this work will deal with deriving expressions for $\Pi^{\mu\nu}$, which together with (2.23) will give different theories of viscous hydrodynamics.

An elegant way of obtaining $\Pi^{\mu\nu}$ builds upon the second law of thermodynamics, which states that entropy must always increase locally. The entropy density s is connected to energy density, pressure and temperature T by the basic equilibrium thermodynamic relations for a system without conserved charges (or zero chemical potential),

$$\epsilon + p = Ts, \qquad Tds = d\epsilon \ . \tag{2.24}$$

The second law of thermodynamics can be recast in the covariant form

$$\partial_\mu s^\mu \geq 0 \tag{2.25}$$

using the entropy 4-current s^μ which in equilibrium is given by

$$s^\mu = s u^\mu \ . \tag{2.26}$$

The thermodynamic relations (2.24) allow to rewrite the second law (2.25) as

$$\partial_\mu s^\mu = Ds + s\partial_\mu u^\mu = \frac{1}{T} D\epsilon + \frac{\epsilon + p}{T}\partial_\mu u^\mu = \frac{1}{T}\Pi^{\mu\nu}\nabla_{(\mu} u_{\nu)} \geq 0 \ , \tag{2.27}$$

where (2.23) was used to rewrite $D\epsilon$. It is customary to split $\Pi^{\mu\nu}$ into a part $\pi^{\mu\nu}$ that is traceless, $\pi^{\mu}_{\mu} = 0$, and a remainder with non-vanishing trace,

$$\Pi^{\mu\nu} = \pi^{\mu\nu} + \Delta^{\mu\nu}\Pi \ . \tag{2.28}$$

Similarly one introduces a new notation for the traceless part of $\nabla_{(\mu}u_{\nu)}$,

$$\nabla_{<\mu}u_{\nu>} \equiv 2\nabla_{(\mu}u_{\nu)} - \frac{2}{3}\Delta_{\mu\nu}\nabla_{\alpha}u^{\alpha} \,, \tag{2.29}$$

so that the the second law becomes

$$\partial_{\mu}s^{\mu} = \frac{1}{2T}\pi^{\mu\nu}\nabla_{<\mu}u_{\nu>} + \frac{1}{T}\Pi\nabla_{\alpha}u^{\alpha} \geq 0 \ . \tag{2.30}$$

One recognizes that this inequality is guaranteed to be fulfilled if

$$\pi^{\mu\nu} = \eta\nabla^{<\mu}u^{\nu>} \,, \quad \Pi = \zeta\nabla_{\alpha}u^{\alpha} \,, \quad \eta \geq 0 \,, \quad \zeta \geq 0 \,, \tag{2.31}$$

because then $\partial_{\mu}s^{\mu}$ is a positive sum of squares.

In the non-relativistic limit, the viscous stress tensor becomes that of the Navier-Stokes equations (2.4), which leads one to equate η, ζ with the shear and bulk viscosity coefficient, respectively. Also, for this reason we refer to the system of equations (2.23),(2.28),(2.31) as the relativistic Navier-Stokes equation. While beautifully simple, it turns out that the relativistic Navier-Stokes equation – unlike its non-relativistic counterpart – exhibits pathologies for all but the simplest flow profiles, as will be shown below.

2.8.2 Problem of the relativistic Navier-Stokes equation

Let us consider small perturbations of the energy density and fluid velocity in a system that is initially in equilibrium and at rest,

$$\epsilon = \epsilon_0 + \delta\epsilon(t,x), \qquad u^{\mu} = (1,\vec{0}) + \delta u^{\mu}(t,x), \tag{2.32}$$

where for simplicity the perturbation was assumed to be dependent on one space coordinate only. The relativistic Navier-Stokes equation then specifies the space-time evolution of the perturbations. For the

particular direction $\alpha = y$, Eq. (2.23) gives

$$\begin{aligned}(\epsilon + p)Du^y - \nabla^y p + \Delta^y_\nu \partial_\mu \Pi^{\mu\nu} &= (\epsilon_0 + p_0)\partial_t \delta u^y + \partial_x \Pi^{xy} + \mathcal{O}(\delta^2)\,, \\ \Pi^{xy} = \eta\left(\nabla^x u^y + \nabla^y u^x\right) + \left(\zeta - \frac{2}{3}\eta\right)\Delta^{xy}\nabla_\alpha u^\alpha &= -\eta_0\ \partial_x \delta u^y + \mathcal{O}(\delta^2)\ .\end{aligned}$$

This implies a diffusion-type evolution equation for the perturbation $\delta u^y(t, x)$:

$$\partial_t \delta u^y - \frac{\eta_0}{\epsilon_0 + p_0}\partial_x^2 \delta u^y = \mathcal{O}(\delta^2)\ . \tag{2.33}$$

To investigate the individual modes of this diffusion process, one can insert a mixed Laplace-Fourier wave ansatz

$$\delta u^y(t, x) = e^{-\omega t + ikx} f_{\omega,k}$$

into Eq. (2.33). This gives the "dispersion-relation" of the diffusion equation,

$$\omega = \frac{\eta_0}{\epsilon_0 + p_0}k^2\ , \tag{2.34}$$

which one can use to estimate the speed of diffusion of a mode with wavenumber k,

$$v_T(k) = \frac{d\omega}{dk} = 2\frac{\eta_0}{\epsilon_0 + p_0}k\ . \tag{2.35}$$

One finds that v_T is linearly dependent on the wavenumber, which implies that as k becomes larger and larger, the diffusion speed will grow without bound. In particular, at some sufficiently large value of k, $v_T(k)$ will exceed the speed of light, which violates causality. Therefore the relativistic Navier-Stokes equation does not constitute a causal theory.

The obvious conclusion to draw from this argument is that the relativistic Navier-Stokes equation exhibits unphysical behavior for the short wavelength ($k \gg 1$) modes and hence can only be valid in the description of the long wavelength modes. This is not a principal problem, as one can regard hydrodynamics simply as an effective theory of matter in the long wavelength, $k \to 0$ limit. However, having a finite range of validity in k typically is a practical problem when dealing with more complicated flow profiles that do not lend themselves to analytic solutions and have to be solved numerically. In this case, it turns out that the high k modes are associated with instabilities [93] that make it necessary to regulate the theory by other means. A simple argument to understand the practical problem can be given as follows: modes that travel faster than the speed of light in one Lorentz frame correspond to modes traveling backwards in time in a different frame.

Hydrodynamics is an initial value problem which requires a well defined set of initial conditions. However, if there are modes present in the equations that travel backwards in time, the initial conditions cannot be given freely [94], and as a consequence one cannot solve the relativistic Navier-Stokes equation numerically.

2.8.3 Müller-Israel-Stewart theory

In the derived Navier-Stokes equation, it is not guaranteed that the entropy current equals its equilibrium expression for a dissipative fluid that can be out of equilibrium. Specifically, it was suggested [83] that out of equilibrium the entropy current can have contributions from the viscous stress tensor, which is sometimes referred to as "extended irreversible thermodynamics" [83]. Assuming that the entropy current has to be algebraic in the hydrodynamic degrees of freedom and that deviations from equilibrium are not too large so that high order corrections can be neglected, the entropy current has to be of the form [83, 92]

$$s^\mu = s u^\mu - \frac{\beta_0}{2T} u^\mu \Pi^2 - \frac{\beta_2}{2T} u^\mu \pi_{\alpha\beta}\pi^{\alpha\beta} + \mathcal{O}(\Pi^3) \ , \tag{2.36}$$

where β_0, β_2 are coefficients that quantify the effect of these second-order modifications of the entropy current. Using again Eq. (2.23) to rewrite $\partial_\mu s^\mu$ as in section 2.8.1 one finds

$$\begin{aligned} \partial_\mu s^\mu &= \frac{\pi^{\alpha\beta}}{2T}\left(\nabla_{<\alpha}u_{\beta>} - \pi_{\alpha\beta} T D\left(\frac{\beta_2}{T}\right) - 2\beta_2 D\pi_{\alpha\beta} - \beta_2 \pi_{\alpha\beta}\partial_\mu u^\mu\right) \\ &\quad + \frac{\Pi}{T}\left(\nabla_\alpha u^\alpha - \frac{1}{2}\Pi\, T D\left(\frac{\beta_0}{T}\right) - \beta_0 D\Pi - \frac{1}{2}\beta_0 \Pi \partial_\mu u^\mu\right) \geq 0 \ . \end{aligned} \tag{2.37}$$

The inequality is guaranteed to be fulfilled if

$$\begin{aligned} \pi_{\alpha\beta} &= \eta\left(\nabla_{<\alpha}u_{\beta>} - \pi_{\alpha\beta} T D\left(\frac{\beta_2}{T}\right) - 2\beta_2 D\pi_{\alpha\beta} - \beta_2 \pi_{\alpha\beta}\partial_\mu u^\mu\right) \ , \\ \Pi &= \zeta\left(\nabla_\alpha u^\alpha - \frac{1}{2}\Pi\, T D\left(\frac{\beta_0}{T}\right) - \beta_0 D\Pi - \frac{1}{2}\beta_0 \Pi \partial_\mu u^\mu\right) \ , \end{aligned} \tag{2.38}$$

with η, ζ the usual bulk and shear viscosity coefficients. Note that Eq. (2.38) coincides with the Navier-Stokes equation in the limit of $\beta_0, \beta_2 \to 0$. For non-vanishing β_0, β_2, Eq. (2.38) contains time derivatives of $\pi_{\alpha\beta}, \Pi$, which are similar (but not identical) to the Maxwell-Cattaneo law Eq. (**??**) if one identifies $\beta_2 = \frac{\tau_\pi}{2\eta}$ (and similarly, $\beta_0 = \frac{\tau_\Pi}{\zeta}$). The set of equations (2.23),(2.38) (and some variations thereof) are commonly referred to as "Müller-Israel-Stewart" theory and will be discussed more in section **??**.

Similar to section 2.8.2, one can study the causality properties of the Müller-Israel-Stewart theory by considering small perturbations around equilibrium, Eq. (2.32). Keeping only perturbations to first order,

Eq. (2.23) and Eq. (2.38) become

$$\partial_t \delta\epsilon + (\epsilon_0 + p_0)\partial_x \delta u^x = 0, \quad (\epsilon_0 + p_0)\partial_t \delta u^x + \partial_x p + \partial_\mu \delta\Pi^{\mu x} = 0,$$
$$(\epsilon_0 + p_0)\partial_t \delta u^y + \partial_\mu \delta\Pi^{\mu y} = 0, \quad \delta\Pi^{\mu\nu} = \delta\pi^{\mu\nu} + g^{\mu\nu}\delta\Pi$$
$$\delta\pi^{xx} + \tau_\pi \partial_t \delta\pi^{xx} = -\tfrac{4}{3}\eta_0 \partial_x \delta u^x, \quad \delta\pi^{xy} + \tau_\pi \partial_t \delta\pi^{xy} = -\eta_0 \partial_x \delta u^y,$$
$$\delta\Pi + \tau_\Pi \partial_t \delta\Pi = \zeta_0 \partial_x \delta u^x \,. \tag{2.39}$$

The equation of state $\epsilon = \epsilon(p)$ relates the pressure and energy density gradients, $\partial_x p = \frac{dp}{d\epsilon}\partial_x \epsilon$, and the condition $u_\mu \Pi^{\mu\nu} = 0$ implies $\delta\Pi^{t\nu} = \mathcal{O}(\delta^2)$. Using a Fourier ansatz

$$\delta\epsilon = e^{i\omega t - ikx}\delta\epsilon_{\omega,k}, \quad \delta u^i = e^{i\omega t - ikx}\delta u^i_{\omega,k}, \quad \delta\pi^{\mu\nu} = e^{i\omega t - ikx}\delta\pi^{\mu\nu}_{\omega,k}, \quad \delta\Pi = e^{i\omega t - ikx}\delta\Pi^{\mu\nu}_{\omega,k},$$

in Eq. (2.39) gives the system of equations

$$i\omega\ \delta\epsilon_{\omega,k} - ik(\epsilon_0 + p_0)\ \delta u^x_{\omega,k} = 0, \tag{2.40}$$
$$i\omega(\epsilon_0 + p_0)\ \delta u^x_{\omega,k} - ik\frac{dp}{d\epsilon}\ \delta\epsilon_{\omega,k} - ik\left(\frac{4}{3}\frac{ik\eta_0}{1 + i\omega\tau_\pi} + \frac{ik\zeta_0}{1 + i\omega\tau_\Pi}\right)\delta u^x_{\omega,k} = 0, \tag{2.41}$$
$$i\omega(\epsilon_0 + p_0)\ \delta u^y_{\omega,k} - ik\left(\frac{ik\eta_0}{1 + i\omega\tau_\pi}\right)\delta u^y_{\omega,k} = 0\,. \tag{2.42}$$

Eq. (2.42) corresponds to result from the Maxwell-Cattaneo law for the transverse velocity perturbation δu^y, discussed in section 2.8.2. The other two equations correspond to density perturbations and longitudinal fluid velocity displacements, commonly known as sound. The sound dispersion relation is given by

$$i\omega - i\frac{k^2}{\omega}\frac{dp}{d\epsilon} + k^2\left(\frac{4}{3}\frac{\eta_0}{\epsilon_0 + p_0}\frac{1}{1 + i\omega\tau_\pi} + \frac{\zeta_0}{\epsilon_0 + p_0}\frac{1}{1 + i\omega\tau_\Pi}\right) = 0\,, \tag{2.43}$$

and in the hydrodynamic limit $(\omega, k \ll 1)$ becomes

$$\omega = \pm k c_s + ik^2\left(\frac{2}{3}\frac{\eta_0}{\epsilon_0 + p_0} + \frac{1}{2}\frac{\zeta_0}{\epsilon_0 + p_0}\right)$$
$$\mp\frac{k^3}{2c_s}\left[\left(\frac{2}{3}\frac{\eta_0}{\epsilon_0 + p_0} + \frac{1}{2}\frac{\zeta_0}{\epsilon_0 + p_0}\right)^2 - 2c_s^2\left(\frac{2}{3}\frac{\eta_0}{\epsilon_0 + p_0}\tau_\pi + \frac{1}{2}\frac{\zeta_0}{\epsilon_0 + p_0}\tau_\Pi\right)\right] + \mathcal{O}(k^4)\,. \tag{2.44}$$

The quantity

$$c_s \equiv \sqrt{\frac{d\ p}{d\ \epsilon}} \tag{2.45}$$

can be recognized to be the speed of sound when calculating the group velocity $\lim_{k\to 0}\frac{d\omega}{dk}$. For large wavenumbers and frequencies, Eq. (2.43) gives a limiting sound mode group velocity of

$$v_L^{\max} \equiv \lim_{k\to\infty}\frac{d\omega}{dk} = \sqrt{c_s^2 + \frac{4}{3}\frac{\eta_0}{\tau_\pi(\epsilon_0+p_0)} + \frac{\zeta_0}{\tau_\Pi(\epsilon_0+p_0)}}\,, \tag{2.46}$$

which together with the result for the transverse mode Eq. (**??**) suggests that the Müller-Israel-Stewart theory – derived via an extended second law of thermodynamics – constitutes a relativistic theory of viscous hydrodynamics that obeys causality if the relaxation times τ_π, τ_Π are not too small. Note that the requirement $v_L^{\max} \leq 1$ from Eq. (2.46) is more restrictive than Eq. (**??**) concerning the allowed values of $c_s^2, \eta, \zeta, \tau_\pi, \tau_\Pi$.

However, many questions remain unanswerable within this formalism, e.g. how to obtain the value of τ_π, τ_Π, or whether the assumption that the entropy current should be algebraic in the hydrodynamic degrees of freedom is valid seem to indicate the contrary). Therefore, it is necessary to have a different derivation of viscous hydrodynamics [83].

2.9 Hydrodynamics as a tool in high energy nuclear collisions

Relativistic collisions of heavy ions (nuclei with an atomic weight heavier than carbon) offer one of the few possibilities to study nuclear matter under extreme conditions in a laboratory. The defining parameters for heavy-ion collisions are the center-of-mass collision energy per nucleon pair $\sqrt{s}$ and the geometry of the colliding nuclei (gold nuclei are typically larger than copper, and uranium nuclei are not spherically symmetric). The collisions are said to be relativistic once the center-of-mass energy is larger than the rest mass of the nuclei, or equivalently if $\sqrt{s}/2$ is larger than the nucleon mass. For the Lorentz γ factor of the collision, this implies

$$\gamma = \frac{m\gamma c^2}{mc^2} = \frac{E^{\text{total}}}{m} \simeq \frac{\sqrt{s}}{2\text{GeV}}\,, \tag{2.47}$$

so typically $\gamma > 1$. Experiments at Brookhaven National Laboratory (AGS, RHIC) and CERN (SPS) have provided a wealth of data for Au+Au collisions (AGS, RHIC) and Pb+Pb collisions (SPS) ranging in energy from $\sqrt{s} \sim 2.5-4.3$ GeV at the AGS over $\sqrt{s} \sim 8-17.3$ GeV at the SPS to $\sqrt{s} \sim 130-200$ GeV at RHIC. It was found that the number density of particles produced in these collisions increases substantially for larger $\sqrt{s}$, indicating a similar rise in the energy density [**?**], that may allow the study of nuclear matter above the deconfinement transition (see Figure **??**).

Early after the collision the evolution in the directions transverse to the initial beam direction (transverse plane) can be assumed to be static, and the dynamics is dominated by the longitudinal expansion of the

system. The evolution of relativistic heavy-ion collision, can be divided into four stages in proper time $\tau = \sqrt{t^2 - z^2}$.

- Stage **I** : Immediately following the collision is the pre-equilibrium stage characterized by strong gradients and possibly strong gauge fields [88], where a hydrodynamic description is not applicable. The duration of this stage is unknown since the process of equilibration in QCD at realistic values of the coupling is not understood, but it is generally assumed to last about 1 fm/c.

- Stage **II** : Is the near-equilibrium regime characterized by small gradients where hydrodynamics should be applicable if the local temperature is well above the deconfinement transition. This stage lasts about $5 - 10$ fm/c, until the system becomes too dilute for equilibrium to be maintained and enters

- stage **III** : The hadron gas regime. The hadron gas is characterized by a comparatively large viscosity coefficient [89],The above four stages described are simulated with different codes as explained in chapter 5.

2.10 Concluding Remarks

Having no a unique theoretical tool to describe the whole heavy ion collision process from the very beginning till the end. We need different tools for the description of the dramatic changes of the effective physical degrees of freedom and their interactions. This includes: generating fluctuating initial conditions, solving the relativistic hydrodynamic equations, sampling particle distribution and finally an after burner. As discussed in the next chapter our framework choice has all the best different routines to simulate the hydrodynamics. Our choice of collision energy puts us on the category of Ultra-relativistic heavy ion collision giving us room to check results both from RHIC and LHC.

Chapter 3: The Elliptic Flow Measurement

3.1 Chapter Introduction

Relativistic heavy ion collisions which at sufficient collisions energys, are theorized to produce the quark gluon plasma produce very large number of subatomic particles in all directions [115]. Two heavy nuclei can be compressed to more than ground state saturation density and heated in head−on collisions at high energy. A flow pattern will develop as the system subsquently expands. Flow refers to how energy, momentum, and number of these particles varies with direction, and elliptic flow is a measure of how the flow is not uniform in all directions when viewed along the beam line. Elliptic flow is strong evidence for the existance of the QGP, and has been described as one of the most important observations measured at the RHIC [40,41]. it describes the azimutahal momentum space anisotropy of particle emission from non-central heavy-ion collisions in the plane transverse to the beam direction, and is defined as the second harmonic coefficient of the azimuthal Fourier decomposition of the momentum distribution. Elliptic flow is a fundamental observable since it directly reflects the initial spatial anisotropy, of the nuclear overlap region in the transverse plane, directly translated into the observed momentum distribution of identified particles. Since the spatial anisotropy is largest at the beginning of the evolution, elliptic flow is especially sensitive to the early stages of system evolution. A measurement of elliptic flow thus provides access to the fundamental thermalization time scale and many more things in the early stages of a relativistic heavy-ion collision [116]. In this section we are about to discuss how the anisotropic flow calculation is developed so that it is now easy to find what ever anisotropic coefficients we desire to.

3.2 Anisotropic Flow

From Fig. 3.1 the central part are participating in the collision where the others keep flying away with nearly a speed of light. As the collision keeps being non−central, the evolved collision region happens to be elliptical, but if gets to be more central the evolution will be circular. The created initial transverse energy density profile looks as given in Fig. 3.2.

Since the location of nucleons in the incoming projectile is not well defined and explicitly known, the collision has zillion ways of creating that hot dense system called the Quark Gluon Plasma (QGP). After

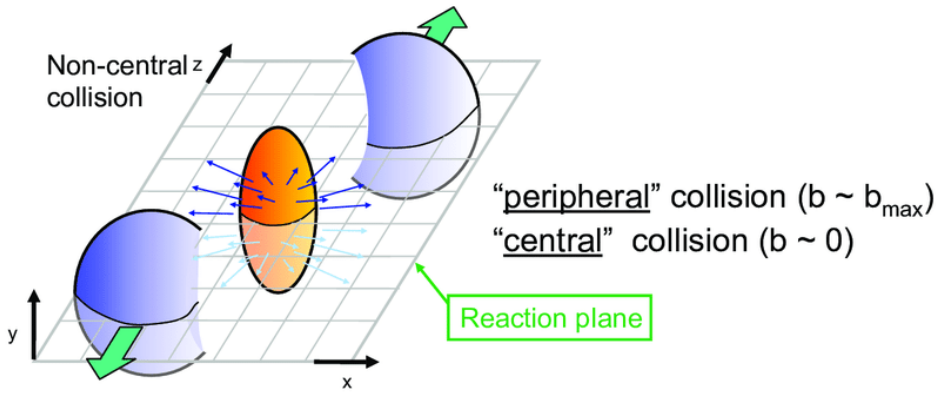

Figure 3.1: A sketch of the geometry of a heavy ion collision. The collision (or longitudinal) axis is denoted as z, while x and y are the transverse coordinates. The interaction region (the almond-shape region where the two nuclei overlap which each other) is singled out. N part is the number of nucleons in this region. The interaction region is horizontally cut by the reaction plane (x, z).The spatial anisotropy with respect to the x-z plane (reaction plane) translates into a momentum anisotropy of the produced particles (anisotropic flow).

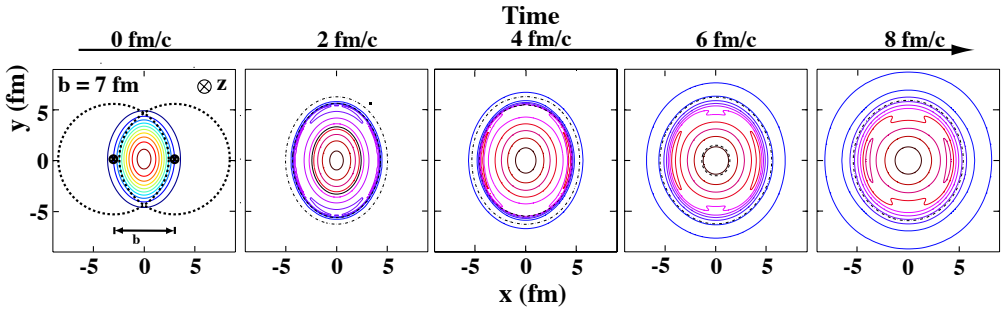

Figure 3.2: The created initial transverse energy density profile and its time dependence in coordinate space for a non-central heavy-ion collision [6]. The z-axis is along the colliding beams, the x-axis is defined by the impact parameter.

collision the created QGP has step pressure change in the transverse direction which is the x axis. This is because of the very high energy density the system hold on to during the little bang. A large gradual pressure change happens in the longitudinal direction where the z axis is taken to be the reaction axis. As the system evolution is studied, it is treated as liquid not gas [117]. As far as liquidity is considered, viscosity comes to play. So we treat the QGP as liquid; that is why it is named to be the Liquid Quark Gluon Plasma and it fabulously flows.

As we observe the pressure change, we notice that the QGP is more like water than other fluids having higher viscosity like honey. Measurements show $\eta/\mathrm{s} = 25(1/4\pi)$ where as that of QGP is $\eta/\mathrm{s} = 5(1/4\pi)$. If we model the shape changes and particle distribution, we can easily set a governing function. LHC having $15x$ bigger collision energy than that of RHIC, explicitly shows the evolution of the system we anticipated above.

Here jumps in Fourier expansion which is a beautiful tool to explain such evolving systems. Putting-in the Fourier series, in the equation of motion gives us an excellent expression for the evolving system. Because Fourier's idea is to model a complicated energy source as a superposition of simple sine and cosine waves, this simplify the problem a lot. Finally we can have the Fourier expansion of the invariant triple differential distributions as follows and the very convenient way of characterizing the various patterns is the invariant triple differential distributions is given by :

$$E\frac{\mathrm{d}^3N}{\mathrm{d}^3\mathbf{p}} = \frac{1}{2\pi}\frac{\mathrm{d}^2N}{p_\mathrm{t}\mathrm{d}p_\mathrm{t}\mathrm{d}y}\left(1 + 2\sum_{n=1}^{\infty} v_n \cos[n(\varphi - \Psi_\mathrm{RP})]\right), \tag{3.1}$$

where E : energy of the particle, p : momentum, p_t : transverse momentum, φ : azimuthal angle, y : rapidity, and Ψ_RP : reaction plane angle.

The sine terms in such an expansion vanish because of the reflection symmetry with respect to the reaction plane. The Fourier coefficients are p_T and y dependent and are given by

$$v_n(p_\mathrm{T}, y) = \langle \cos[n(\varphi - \Psi_\mathrm{RP})]\rangle, \tag{3.2}$$

where the angular brackets denote an average over the particles, summed over all events, in the (p_T, y) bin under study. In this Fourier decomposition, the coefficients v_1 and v_2 are known as directed and elliptic flow, respectively.

Flow signals the presence of multiple interactions between the constituents of the medium created in the collision. More interactions usually leads to a larger magnitude of the flow and brings the system closer to thermalization. The magnitude of the flow is therefore a detailed probe of the level of thermalization. The theoretical tools to describe flow are hydrodynamics or microscopic transport (cascade) models. In the transport models flow depends on the opacity of the medium, be it partonic or hadronic. Hydrodynamics becomes applicable when the mean free path of the particles is much smaller than the system size, and allows for a description of the system in terms of macroscopic quantities. This gives a handle on the equation of state of the flowing matter and, in particular, on the value of the sound velocity c_s.

Experimentally, the most direct evidence of flow comes from the observation of anisotropic flow which is the anisotropy in particle momentum distributions correlated with the reaction plane. The reaction plane is defined by the impact parameter and the beam direction z (see Fig. 3.1).

3.3 Flow Analysis in ALICE

ALICE (A Large Ion Collider Experiment) is a heavy-ion detector on the Large Hadron Collider (LHC) ring. It is designed to study the physics of strongly interacting matter at extreme energy densities, where a phase of matter called quark-gluon plasma forms. All ordinary matter in today's universe is made up of atoms. Each atom contains a nucleus composed of protons and neutrons (except hydrogen, which has no neutrons), surrounding by a cloud of electrons. Protons and neutrons are in turn made of quarks bound together by other particles called gluons. No quark has ever been observed in isolation. It seems that both the quark and gluons confined permanently inside composite particles.

Collisions in the LHC generate temperatures more than 100,000 times hotter than the centre of the Sun. For part of each year the LHC provides collisions between lead ions, recreating in the laboratory conditions similar to those just after the big bang. Under these extreme conditions, protons and neutrons "melt", freeing the quarks from their bonds with the gluons. This is quark-gluon plasma. The existence of such a phase and its properties are key issues in the theory of quantum chromodynamics (QCD), for understanding the phenomenon of confinement, and for a physics problem called chiral-symmetry restoration. The ALICE collaboration studies the quark-gluon plasma as it expands and cools, observing how it progressively gives rise to the particles that constitute the matter of our universe today.

The ALICE collaboration uses the 10000 tonne ALICE detector : 26 m long, 16 m high, and $16m$ wide ; to study quark-gluon plasma. The detector sits in a vast cavern 56 m below ground close to the village of St Genis−Pouilly in France, receiving beams from the LHC.

3.3.1 How a detector works

Just as hunters can identify animals from tracks in mud or snow, physicists identify subatomic particles from the traces they leave in detectors. Accelerators at CERN boost particles to high energies before they are made to collide inside detectors. The detectors gather clues about the particles including their speed, mass and charge from which physicists can work out a particle′s identity. The process requires accelerators, powerful electromagnets, and layer upon layer of complex subdetectors.

Particles produced in collisions normally travel in straight lines, but in the presence of a magnetic field their paths become curved. Electromagnets around particle detectors generate magnetic fields to exploit this

effect. Physicists can calculate the momentum of a particle −a clue to its identity − from the curvature of its path: particles with high momentum travel in almost straight lines, whereas those with very low momentum move forward in tight spirals inside the detector.

Modern particle detectors consists of layers of subdetectors which are designed to look for particular properties or specific types of particle. Tracking devices reveal the path of a particle, calorimeters stop, absorb and measure a particle's energy and particle identification detectors use a range of techniques to pin downa particl's identity.

3.3.2 Tracking devices

Tracking devices reveal the paths of electricity charged particles as they pass through and interact with suitable substances. Most tracking device do not make particle trackers directly visible, but record tiny electrical signals that particles trigger as they move through the device. A computer program than reconstracts the recorded patterns of tracks. Muon chamber tracking devices specialized for detecting muons usually make up the outermost layer of a detector. A calorimeter measures the energy particle loses as it passes through. It is usually designed to stop entirely or absorb most of the particles coming from a collision with in the detector.

Electromagnetic calorimeters measure the energy of electrons and photons as they interact with the electrically charged particles in matter. Hadronic calorimeters sample the energy of hadrons (particles containing quarks, such as protons and neutrons) as they interact with atomic nuclei. Calorimeters can stop most known particles except muons and neutrinos.

3.3.3 Particle-identification detectors

Once a particle has passed through the tracking devices and the calorimeters, physicists have two further methods of narrowing down its identity. Both methods work by detecting radiation emitted by charged particles.

When a charged particle travels faster than light does through a given medium, it emits Cherenkov radiation at an angle that depends on its velocity. The particle's velocity can be calculated from this angle. Velocity can then be combined with a measure of the particle's momentum to determine its mass, and therefore its identity.

When a fast charged particle crosses the boundary between two electrical insulators with different resistances to electric currents, it emits transition radiation. The phenomenon is related to the energy of the particle and so can distinguish different particle types.

Collating all these clues from different parts of the detector, physicists build up a snapshot of what was in the detector at the moment of a collision. The next step is to scour the collisions for unusual particles, or for results that do not fit current theories.

It has been a while since studies of particle production at the BNL Relativistic Heavy Ion Collider (RHIC) have revealed strong collective effects: in particular, the azimuthal distribution transverse to the direction of the colliding nuclei has sizable anisotropies, a phenomenon called anisotropic flow. The main component of this anisotropy, elliptic flow, has been extensively measured for several beam energies and collision systems [119–121].

Anisotropic flow is most often analyzed using the event-plane method [122]. Whether it is at the RHIC or LHC this analysis technique is plagued by systematic errors due to many sources like nonflow effects [123], fluctuations [124, 125] and many more. Yet anisotropic flow of selected produced particles, in a given part of phase-space, is defined as their azimuthal correlation with the reaction plane [127]

$$v_n \equiv \langle \cos(n(\phi - \Phi_{RP})) \rangle \tag{3.3}$$

where n is an integer (v_1 is *directed* flow, v_2 is *elliptic* flow), ϕ, Φ_{RP} and angular brackets denote respectively the azimuth of the particle under study, the azimuth of the reaction plane, and an average over particles and events. Since Φ_{RP} is not known experimentally, v_n cannot be measured directly.

The most commonly used method to estimate v_n is the event-plane method [122], which we are about to discuss here. In each event, one constructs an estimate of the reaction plane Φ_{RP}, the "event plane" Φ_{EP} [128]. The anisotropic flow coefficients are then estimated as

$$v_n\{\mathrm{EP}\} \equiv \frac{1}{R} \langle \cos(n(\phi - \Phi_{EP})) \rangle \,, \tag{3.4}$$

where $R = \langle \cos(n(\Phi_{EP} - \Phi_{RP})) \rangle$ is the event-plane resolution, which corrects for the difference between Φ_{EP} and Φ_{RP}. This resolution is determined in each class of events through a standard procedure [129].

The analogy between Eq. (3.4) and Eq. (3.3) makes the method rather intuitive, but its practical implementation has a few subtleties:

- One must remove autocorrelations: the particle under study should not be used in defining the event plane.
- Sources of correlation, other than flow
- Event-plane flattening procedures to correct azimuthal asymmetries of the detector acceptance [122].

A systematic way of suppressing nonflow effects is to use improved methods such as cumulants or Lee-Yang zeroes. Cumulants have been used at SPS and RHIC. Lee-Yang zeroes have been implemented at SIS and at RHIC. They are comparatively much less used than the event-plane method, and one reason is that the event-plane method is deemed more intuitive and handy.

3.4 The event-plane method

The corresponding estimate of v_n is defined as

$$v_n\{\mathrm{LYZ}\} \equiv \langle W_R \cos(n(\phi - \Phi_{EP}))\rangle \,, \tag{3.5}$$

where Φ_{EP} is the same as in Eq. (3.4), and W_R is an event weight as defined in this paper. The formal analogy with the event-plane method, Eq. (3.4), is obvious.

3.4.1 The flow vector

The first step of the flow analysis is to evaluate, for each event, the flow vector of the event. It is a two-dimensional vector $\mathbf{Q} = (Q_x, Q_y)$ defined as

$$\begin{aligned} Q_x = Q\cos(n\Phi_{EP}) &\equiv \sum_{j=1}^{M} w_j \cos(n\phi_j) \\ Q_y = Q\sin(n\Phi_{EP}) &\equiv \sum_{j=1}^{M} w_j \sin(n\phi_j), \end{aligned} \tag{3.6}$$

where the sum runs over all detected particles. M is the observed multiplicity of the event, ϕ_j are the azimuthal angles of the particles measured with respect to a fixed direction in the laboratory. The coefficients w_j in Eq. (3.6) are weights depending on transverse momentum, particle mass and rapidity. The best weight, which minimizes the statistical error (or, equivalently, maximizes the resolution) is v_n itself, $w_j(p_T, y) \propto v_n(p_T, y)$ [**?**]. A reasonable choice for elliptic flow measurements at RHIC (and probably LHC) is $w = p_T$.

If collective flow is present, the azimuthal angles ϕ_j and the event plane Φ_{EP} are correlated with the true reaction plane Φ_{RP}, and the goal of the flow analysis is to measure this correlation. This is usually done within a set of events belonging to the same centrality class. Integrated flow is defined as the average value of the projection of $\mathbf{Q}$ onto the true reaction plane:

$$V_n \equiv \langle Q\cos(n(\Phi_{EP} - \Phi_{RP}))\rangle \tag{3.7}$$

where angular brackets denote an average over events in the same centrality class. We use a capital letter for V_n because it is in general a dimensionful quantity: it is the weighted sum of the v_n's of individual particles, according to Eqs. (3.3) and (3.6). The flow vector fluctuates around this average value because the multiplicity is finite. These fluctuations can be modeled using the central limit theorem. The resulting distribution of Q is [123]:

$$\frac{dN}{dQ} = \frac{2\chi^2 Q}{V_n^2} \exp\left(-\chi^2\left(\frac{Q^2}{V_n^2}+1\right)\right) I_0\left(\frac{2\chi^2 Q}{V_n}\right), \tag{3.8}$$

where χ is a dimensionless quantity called the resolution parameter, which characterizes the relative magnitude of collective flow and statistical fluctuations. The resolution R in Eq. (3.4) increases from 0 to 1 as χ goes from 0 to $+\infty$. Fig. 3.3 illustrates the distribution of Q for two values of χ. For $\chi \gg 1$, this distribution is a narrow peak centered at $Q = V_n$.

Lee-Yang zeroes use the projection of the flow vector onto a fixed, arbitrary direction making an angle $n\theta$ with respect to the x-axis. We denote this projection by Q_θ:

$$Q_\theta \equiv Q_x \cos n\theta + Q_y \sin n\theta = Q\cos(n(\Phi_{EP} - \theta)). \tag{3.9}$$

3.4.2 Integrated flow

We now explain how the integrated flow V_n, defined by Eq. (3.7), is obtained. We define the complex-valued function:

$$G_\theta(r) \equiv \left\langle e^{irQ_\theta} \right\rangle \equiv \frac{1}{N_{\text{evts}}} \sum_{\text{events}} e^{irQ_\theta}. \tag{3.10}$$

If there is no collective flow, the probability distribution of Q_θ is a Gaussian due to the central limit theorem (if $M \gg 1$). Its Fourier transform $G_\theta(r)$ is also a Gaussian. Collective flow results in oscillations of $G_\theta(r)$ around zero: In the ideal case where the multiplicity is so large that fluctuations can be neglected, $\Phi_{EP} \simeq \Phi_{RP}$ and $Q \simeq V_n$.

3.4.3 Differential flow and event weight

We now derive the expression of the event weight in Eq. (3.5), which is the crucial improvement of our paper over the standard event-plane method. The goal is to measure the differential flow v_n of selected produced particles. v_n can be obtained by shifting the weights w_j of the selected particles in Eq. (3.6) by an infinitesimal quantity ε, $w_j' = w_j + \varepsilon$, and computing the integrated flow V_n' with the new weights. The

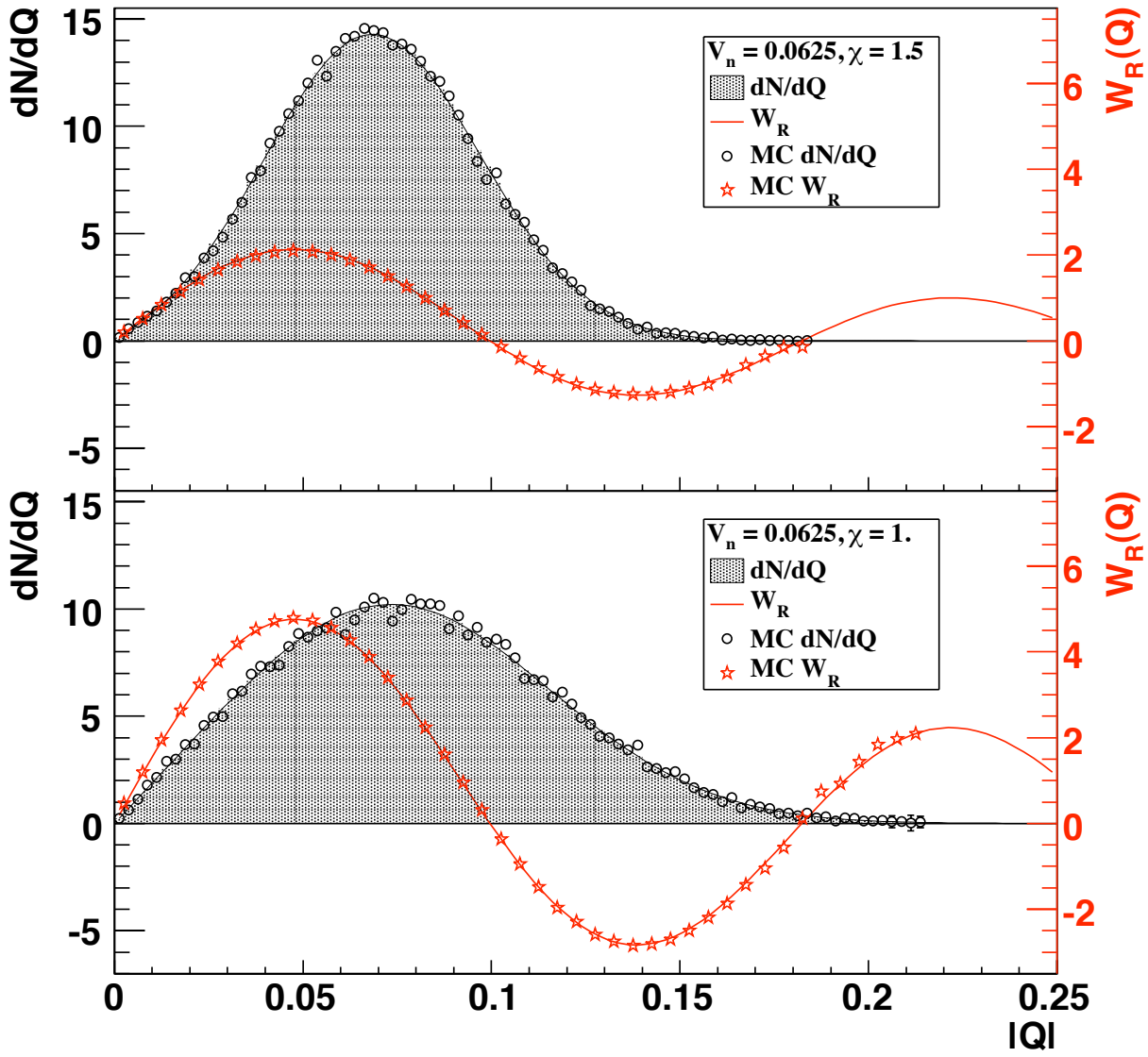

Figure 3.3: (Shaded area: probability distribution of Q [126].

differential flow is then simply given by $v_n = \delta V_n/\varepsilon$, with $\delta V_n = V_n' - V_n$. Differentiating Eq. (**??**),

$$v_n\{\mathrm{LYZ}\} = \frac{\delta \mathrm{V_n}}{\varepsilon} = -\frac{\mathrm{V_n}}{\varepsilon}\frac{\delta \mathrm{r}_\theta}{\mathrm{r}_\theta}, \tag{3.11}$$

where δr_θ denotes the shift of the zero. Differentiating the condition $\langle e^{ir_\theta Q_\theta}\rangle = 0$, one obtains

$$\delta r_\theta \left\langle Q_\theta e^{ir_\theta Q_\theta}\right\rangle + r_\theta \left\langle \delta Q_\theta e^{ir_\theta Q_\theta}\right\rangle = 0. \tag{3.12}$$

For an event containing one selected particle, Eqs. (3.6) and (3.9) give $\delta Q_\theta = \varepsilon\cos(n(\phi-\theta))$, where ϕ is the azimuth of the selected particle. Eq. (3.11) then gives

$$v_n\{\mathrm{LYZ}\} = \mathrm{V_n}\frac{\left\langle \cos(\mathrm{n}(\phi-\theta))\mathrm{e}^{\mathrm{ir}_\theta \mathrm{Q}_\theta}\right\rangle}{\langle \mathrm{Q}_\theta \mathrm{e}^{\mathrm{ir}_\theta \mathrm{Q}_\theta}\rangle}, \tag{3.13}$$

where the average in the numerator is over selected particles, and the average in the denominator is over events. In this expression, θ is an arbitrary reference angle. Both the numerator and the denominator are expected to be independent of θ, up to asymmetries in the detector acceptance, and statistical fluctuations. In practice, we recommend to first take the ratio and then average over θ, as explained in Sec.**??**. Here, we derive simple approximate expressions by assuming that r_θ is independent of θ, and by averaging the numerator and the denominator over θ *before* taking the ratio. We thus obtain:

$$v_n\{\mathrm{LYZ}\} = \mathrm{V_n}\frac{\langle \cos(\mathrm{n}(\phi-\Phi_{\mathrm{EP}}))\mathrm{J}_1(\mathrm{r}_\theta \mathrm{Q})\rangle}{\langle \mathrm{Q}\mathrm{J}_1(\mathrm{r}_\theta \mathrm{Q})\rangle}, \tag{3.14}$$

where $J_1(x)$ is the derivative of $-J_0(x)$. Identifying Eq. (3.14) with Eq. (3.5), we obtain the event weight

$$W_R \equiv \frac{1}{C} J_1(r_\theta Q), \tag{3.15}$$

where C is a normalization constant which can be computed using the distribution (3.8):

$$C = \frac{1}{V_n}\langle Q J_1(r_\theta Q)\rangle = \exp\left(-\frac{j_{01}^2}{4\chi^2}\right) J_1(j_{01}). \tag{3.16}$$

The difference with the standard event-plane analysis is that each event is given a weight (3.15) which depends on the length of the flow vector Q, a quantity which is not used in the standard analysis. Eq. (3.15) involves the integrated flow V_n through r_θ, which must be determined in a first pass through the data.

Fig. 3.3 displays the variation of W_R with Q, for two values of the resolution parameter. For $\chi \gg 1$, the distribution of Q is a narrow peak centered at $Q = V_n$. Therefore, the weight defined by Eqs. (3.15) and (3.16) is close to 1 for all events. If χ is smaller, the distribution of Q is wider, and W_R is negative for some events. These negative weights are required in order to subtract nonflow effects. On the other hand, they also subtract part of the flow. In order to compensate for this effect, the global normalization of the weight increases when χ decreases (as illustrated in Fig. 3.3 by the fact that the amplitude of the curve showing the weight changes for different values of χ). This qualitatively explains the χ dependence in Eq. (3.16).

The weight (3.15) vanishes linearly at $Q = 0$. This is physically intuitive. Given that the flow vector is obtained by summing over all particles, one increases the relative weight of collective flow over individual, random motion of the particles. If the flow vector is small in an event, it means that the random motion hides the collective motion in this particular event, which is therefore of little use for the flow analysis.

3.4.4 Nonflow effects and autocorrelations

Let us see how Lee-Yang zeroes are able to eliminate nonflow effects and autocorrelations with two examples. As a first example, we assume that each particle splits into two particles with identical momenta, roughly imitating the effect of resonance decays or track splitting in a detector. This splitting does not change the anisotropic flow v_n, defined by Eq. (3.3), but it introduces nonflow correlations, which bias standard analyses. The splitting leaves $v_n\{\text{LYZ}\}$ unchanged: it multiples both the flow vector, Eq. (3.6) and the integrated flow V_n, Eq. (3.7) by 2. Therefore r_θ in Eq. (**??**) is divided by 2, and $v_n\{\text{LYZ}\}$ defined by Eq. (3.13) is unchanged [118].

As a second example, we consider the situation where there is collective flow in the system, but the selected particles have $v_n = 0$. We further assume that the selected particles are uncorrelated with the other particles. In the standard event-plane method, one needs to subtract the selected particles from the flow vector (3.6), otherwise autocorrelations yield $v_n\{EP\} > 0$. We now show that $v_n\{LYZ\} = 0$, even if selected particles are included in the flow vector.

We separate the flow vector, Eq. (3.6), into the contribution of selected particles, $\mathbf{Q}_{\text{sel.}}$, and other particles $\mathbf{Q}_{\text{others}}$.

$$\mathbf{Q} = \mathbf{Q}_{\text{sel.}} + \mathbf{Q}_{\text{others}}. \tag{3.17}$$

Our estimate of v_n is defined by Eq.(3.13). Since the flow vector appears in an exponential, the contributions of selected particles and other particles can be written as a product of two independent factors: [118].

$$v_n = V_n \frac{\left\langle \cos(n(\phi-\theta)) e^{ir_\theta (Q_{\text{sel.}})_\theta} \right\rangle \left\langle e^{ir_\theta (Q_{\text{others}})_\theta} \right\rangle}{\left\langle Q_\theta e^{ir_\theta Q_\theta} \right\rangle}, \tag{3.18}$$

Let us define $G_{\text{others},\theta}(r)$ by replacing Q_θ with $Q_{\text{others},\theta}$ in Eq. (3.10). Following the same reasoning as in Sec. 3.4.2, the first zero of $G_{\text{others},\theta}$ depends on the integrated flow $V_{n,\text{others}}$ of other particles. We have assumed that $v_n = 0$ for selected particles, therefore $V_{n,\text{others}} = V_n$, and

$$\left\langle e^{ir_\theta (Q_{\text{others}})_\theta} \right\rangle = \left\langle e^{ir_\theta Q_\theta} \right\rangle = 0. \tag{3.19}$$

Inserting into Eq. (3.18), we find

$$v_n\{\text{LYZ}\} = 0, \tag{3.20}$$

up to statistical fluctuations. This proof can easily be generalized to the situation where each selected particle is correlated with a few additional particles (e.g. within a jet) which are not correlated with the bulk of particles producing collective flow. This examples show Lee-Yang zeroes are able to eliminate nonflow effects and autocorrelations. In actual experiments, however, flow and nonflow effects are likely to be mingled, and detailed simulations must be carried out to determine to what extent the suppression is effective [118].

3.5 Cumulant Method

Quantitatively, anisotropic flow is characterized by coefficients in the Fourier expansion of the azimuthal dependence of the invariant yield of particles relative to the reaction plane [122, 127]:

$$E\frac{d^3N}{d^3p} = \frac{1}{2\pi}\frac{d^2N}{p_t dp_t dy}\left(1+\sum_{n=1}^{\infty} 2v_n \cos\left(n(\phi-\Psi_R)\right)\right). \tag{3.21}$$

Here E is the energy of particle, p_t is the transverse momentum, ϕ is its azimuthal angle, y is the rapidity, and Ψ_R the reaction plane angle (see Fig 3.4). The first coefficient, v_1, is usually called *directed flow*, and the second coefficient, v_2, is called *elliptic flow*. In general the $v_n = \langle\cos[n(\phi - \psi rp)]\rangle$ coefficients are p_t and y dependent – in this context we refer to them as *differential flow*. The *integrated* flow is defined as a weighted average with the invariant distribution used as a weight:

$$v_n \equiv \frac{d\vec{s}\int_0^\infty v_n(p_t)\frac{d\vec{s}dN}{d\vec{s}dp_t}dp_t}{d\vec{s}\int_0^\infty \frac{d\vec{s}dN}{d\vec{s}dp_t}dp_t}. \tag{3.22}$$

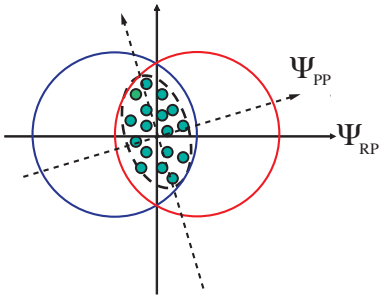

Figure 3.4: Schematic view of a non-central nucleus-nucleus collision in the transverse plane.

Since the reaction plane Ψ_R is not known experimentally, the anisotropic flow is estimated using azimuthal correlations between the observed particles. For example, using 2-particle azimuthal correlations:

$$\langle \cos(n(\phi_1 - \phi_2)) \rangle = \left\langle e^{in(\phi_1 - \phi_2)} \right\rangle = \langle v_n^2 \rangle + \delta_n, \tag{3.23}$$

where the first term, $\langle v_n^2 \rangle$, is the part due to anisotropic flow, and δ_n represents the so called non-flow contribution, that comes from correlations not related to the initial system geometry. If non-flow is small, Eq. (3.23) can be used to measure v_n, but in general the non-flow contribution is not negligible. To suppress non-flow one can exploit the collective nature of anisotropic flow using multi-particle correlations. The method based on multi-particle cumulants (*genuine* multi-particle correlations) to measure anisotropic flow was proposed in. This method allows to subtract non-flow effects from flow measurements order by order. Note that some experimental artifacts, such as track splitting, in the analysis also contribute to the two particle correlation; in this respect multi-particle techniques are also valuable, as they suppress such contributions as well.

One of the problems in using multi-particle correlations is the computing power needed to go over all possible particle multiplets, which practically prohibits calculations of correlations of order larger than $k = 3$ (three-particle correlations). To avoid this problem expressing cumulants in terms of moments of the magnitude of the corresponding flow vector Q_n, is defined as:

$$Q_n \equiv \sum_{i=1}^{M} e^{in\phi_i}\,, \tag{3.24}$$

where M is the number of particles. Unfortunately, flow estimates from cumulants constructed in such a way were systematically biased by the interference between various harmonics. An improved cumulant method using the formalism of generating functions suggested in many other studies fixed the problem of interfering

harmonics while keeping the number of operations still linear with multiplicity M. For this approach the analytical calculations become rather tedious and therefore the solutions are obtained using interpolation formulae. Unfortunately this introduces numerical uncertainties and requires tuning of interpolating parameters for different values of the flow harmonics v_n and multiplicity. More recently a Lee-Yang-Zero's sum method has been developed to suppress non-flow contribution to all orders. Closely related to that are methods of Fourier and Bessel transforms of the Q-distributions, and the method of direct fitting of the Q-distribution. All these methods, while indeed being almost insensitive to non-flow, are biased by interference of different harmonics.

3.6 Multi-Particle azimuthal correlations and cumulants

In this paper we discuss mostly 2- and 4-particle azimuthal correlations (formulae for 6-particle correlation are provided in the Appendix), but the generalization to azimuthal correlations involving more particles is straightforward. The method can be easily applied for calculations of *mixed harmonics* multi-particle correlations. In fact, mixed harmonics correlations are needed in our approach for calculations of any multi-particle correlations with order higher than 2. Presenting 4-particle correlations below, we also show how the 3-particle correlations, involving one particle of a double harmonic can be calculated. All the correlations are obtained by first averaging over all particles in a given event and then averaging over all events. The latter may involve weights depending on event multiplicity.

We define *single-event* average 2- and 4-particle azimuthal correlations in the following way:

$$\langle 2 \rangle \equiv \left\langle e^{in(\phi_1-\phi_2)} \right\rangle \equiv \frac{1}{P_{M,2}} \sum{}' p_{i,j} e^{in(\phi_i-\phi_j)}\,, \tag{3.25}$$

$$\langle 4 \rangle \equiv e^{in(\phi_i+\phi_j-\phi_k-\phi_l)}\,, \tag{3.26}$$

where $P_{n,m} = n!/(n-m)!$, and the prime in the sum $\sum' p$ means that all indices in the sum must be taken different.

The second step involves averaging over all events:

$$\begin{aligned} \mathrm{m}ean2 &\equiv \left\langle\left\langle e^{in(\phi_1-\phi_2)} \right\rangle\right\rangle \\ &\equiv \frac{d\vec{s}\sum_{\mathrm{events}}(W_{\langle 2\rangle})_i \langle 2\rangle_i}{d\vec{s}\sum_{\mathrm{events}}(W_{\langle 2\rangle})_i}\,, \end{aligned} \tag{3.27}$$

$$\begin{aligned} \mathrm{m}ean4 &\equiv \left\langle\left\langle e^{in(\phi_1+\phi_2-\phi_3-\phi_4)} \right\rangle\right\rangle \\ &\equiv \frac{d\vec{s}\sum_{\mathrm{events}}(W_{\langle 4\rangle})_i \langle 4\rangle_i}{d\vec{s}\sum_{\mathrm{events}}(W_{\langle 4\rangle})_i}\,, \end{aligned} \tag{3.28}$$

where by double brackets we denote an average, first over all particles and then over all events. $W_{\langle 2\rangle}$ and $W_{\langle 4\rangle}$ are the event weights, which are used to minimize the effect of multiplicity variations in the event sample on the estimates of 2- and 4-particle correlations. In general, the optimal choice of weights would be determined by the multiplicity dependence of v_n. The best approach might be to calculate the cumulants at fixed M and then average over the entire event sample. In our calculations, with v_n independent of multiplicity, we use:

$$W_{\langle 2\rangle} \equiv M(M-1)\,, \tag{3.29}$$

$$W_{\langle 4\rangle} \equiv M(M-1)(M-2)(M-3)\,. \tag{3.30}$$

The above choice for the event weights takes into account the number of different 2- and 4-particle combinations in an event with multiplicity M.

3.7 Reference flow

To obtain the 2$^{\rm nd}$ order cumulant it suffices to separate diagonal and off-diagonal terms in $|Q_n|^2$:

$$|Q_n|^2 = \sum_{i,j=1}^{M} e^{in(\phi_i-\phi_j)} = M + \sum p_{i,j} e^{in(\phi_i-\phi_j)}\,, \tag{3.31}$$

which can be trivially solved to obtain $\langle 2\rangle$:

$$\langle 2\rangle = \frac{|Q_n|^2 - M}{M(M-1)}\,. \tag{3.32}$$

The event averaging is being performed via Eq. (3.27). The resulting expression for $mean2$ is than used to estimate 2$^{\rm nd}$ order cumulant (see Eq. (**??**)), which in turn is used to estimate the reference flow harmonic v_n by making use of Eq. (**??**).

To obtain the 4$^{\rm th}$ order cumulant we start with the decomposition of $|Q_n|^4$ (for details, see Appendix **??**)

$$|Q_n|^4 = Q_n Q_n Q_n^* Q_n^* = \sum_{i,j,k,l=1}^{M} e^{in(\phi_i+\phi_j-\phi_k-\phi_l)}\,. \tag{3.33}$$

We have four distinct cases for the indices i, j, k and l: 1) they are all different (4-particle correlation), 2) three are different, 3) two are different or 4) they are all the same. Note, that the case of three different indices corresponds to the so-called mixed harmonics 3-particle correlations, in many analyses of great interest by itself [**?**, **?**]. Equations for 3-particle correlations are provided in Appendix **??**. Taking everything into

account, we obtain the following analytic result for the single-event average 4-particle correlation defined in Eq. (3.26):

$$\begin{aligned}\langle 4\rangle &= \frac{|Q_n|^4 + |Q_{2n}|^2 - 2\cdot\mathfrak{Re}\left[Q_{2n}Q_n^*Q_n^*\right]}{M(M-1)(M-2)(M-3)} \\ &- 2\,\frac{2(M-2)\cdot|Q_n|^2 - M(M-3)}{M(M-1)(M-2)(M-3)}\,. \end{aligned} \tag{3.34}$$

The reason why the originally proposed cumulant analysis [**?**] was biased lies in the fact that the terms consisting of Q-vectors evaluated in *different* harmonics (for instance terms $|Q_{2n}|^2$ and $\mathfrak{Re}\left[Q_{2n}Q_n^*Q_n^*\right]$) have been neglected. As seen from Eq. (3.34), such terms do appear in the analytic results and are crucial in disentangling the interference between harmonics. In particular, if a higher harmonic v_{2n} is present than $|Q_n|^4$ picks up an additional contribution depending on that harmonic, namely $v_{2n}^2 M(M–1)+v_n^2 v_{2n} 2M(M–1)(M–2)$, which is exactly canceled out with the contribution of harmonic v_{2n} to $|Q_{2n}|^2$ and $\mathfrak{Re}\left[Q_{2n}Q_n^*Q_n^*\right]$, which read $Mv_{2n}^2(M-1)$ and $M(M-1)(M-2)v_n^2 v_{2n}+M(M-1)v_{2n}^2$, respectively.

The final, event averaged 4-particle azimuthal correlation, $\langle\langle 4\rangle\rangle$, is then obtained by making use of Eqs. (3.28) and (3.30). Using $\langle\langle 4\rangle\rangle$ and $\langle\langle 2\rangle\rangle$ one can calculate the 4^{th} order cumulant from Eq. (**??**).

The reference flow is mainly used to calculate differential flow. Therefore, one can optimize the calculation of reference flow to minimize the uncertainties in the final results. This is done by using different weights (e.g. particle transverse momentum) in the definition of flow vectors used in reference flow calculations.

The equations so far are applicable for an analysis with a detector with full uniform azimuthal coverage. In a non-ideal case one needs to take into account the acceptance. Acceptance affects the cumulants in three ways: (i) contributions from additional terms, e.g. proportional to $\langle\langle\cos n\phi\rangle\rangle$ or $\langle\langle\sin n\phi\rangle\rangle$, that for a detector with full uniform azimuthal coverage are identical to zero, (ii) contributions from other flow harmonics, and (iii) the cumulant might be rescaled, which at the end can affect the final extracted flow values. We refer to Refs. [73]

The generalized 2^{nd} order cumulant which can also be used for detectors with non-uniform acceptance is:

$$\begin{aligned} c_n\{2\} &= \langle\langle 2\rangle\rangle - \mathfrak{Re}\Big\{\left[\,\langle\langle\cos n\phi_1\rangle\rangle + i\,\langle\langle\sin n\phi_1\rangle\rangle\,\right] \\ &\quad\times\left[\,\langle\langle\cos n\phi_2\rangle\rangle - i\,\langle\langle\sin n\phi_2\rangle\rangle\,\right]\Big\} \\ &= \langle\langle 2\rangle\rangle - \langle\langle\cos n\phi_1\rangle\rangle^2 - \langle\langle\sin n\phi_1\rangle\rangle^2\,, \end{aligned} \tag{3.35}$$

where for the last line we have used the fact that for instance $\langle\langle\cos n\phi_1\rangle\rangle$ and $\langle\langle\cos n\phi_2\rangle\rangle$ are the same quantities apart from the trivial relabeling. Remarkably, only two additional terms appear in Eq. (3.35), namely $\langle\langle\cos n\phi_1\rangle\rangle^2$ and $\langle\langle\sin n\phi_1\rangle\rangle^2$, which counterbalance the bias to $\langle\langle 2\rangle\rangle$ coming from very general detector inefficiencies. Further details on treating the acceptance effects, including formulae for the 4^{th} order cumulant exists.

3.8 Concluding Remarks

Elliptic flow, being the strong evidence for the existance of the QGP, and being described as one of the most important observations measured at the RHIC, it is crucial to find a way and put it to the mathematics. Fourier analysis makes it possible to describe the momentum and energy evolution. How elliptic flow is measured experimentally is explained here and we have seen how tricky defining the different planes. In doing so, since we loose valuable informations of a given particle, there are different correcting mechanisms. Theoretically the impact parameter being defined and known initially, we need a particle emission function that implements sudden decoupling from a surface element $d^3\sigma$ located on a freeze-out hyper-surface $\Sigma(x^\mu)$ and is given by the Cooper-Frye formula (chapter 5). This formula is implemented in the particle sampler routine, of the framework we have implemented, to calculate not only the elliptic flow but also all the other coefficient.

Chapter 4: The Electro-Magnetic Field

4.1 Chapter Introduction

Large magnetic fields $\vec{B}$ are produced in all non-central heavy ion collisions by the moving and positively charged spectator nucleons that "miss", flying past each other rather than colliding, as well as by the nucleons that participate in the collision. This makes it imperative to establish that the presence of an early-time magnetic field can, via Faraday's Law and the Lorentz force, have observable consequences on the motion of the final-state charged particles seen in the detectors [102]. Estimates obtained $e|\vec{B}|/m_\pi^2 \approx$ 1-3 about 0.1-0.2 fm/c after a RHIC collision with $\sqrt{s}$ = 200 AGeV and $e|\vec{B}|/m_\pi^2 \approx$ 10-15 at some even earlier time after an LHC collision with $\sqrt{s}$ = 2.76 ATeV [103, 104]. Another study founds that the maximal strength of the electromagnetic field eB_y created in relativistic heavy-ion collisions is very high $eB_y \sim 5\ m_\pi^2$ but its duration is $t \sim$0.2 fm/c for Au+Au at $\sqrt{s_{NN}}$ =200 GeV collisions and impact parameter b =10 fm. The electromagnetic fields generated by the charges and currents evolve according to the Maxwell equations [102].

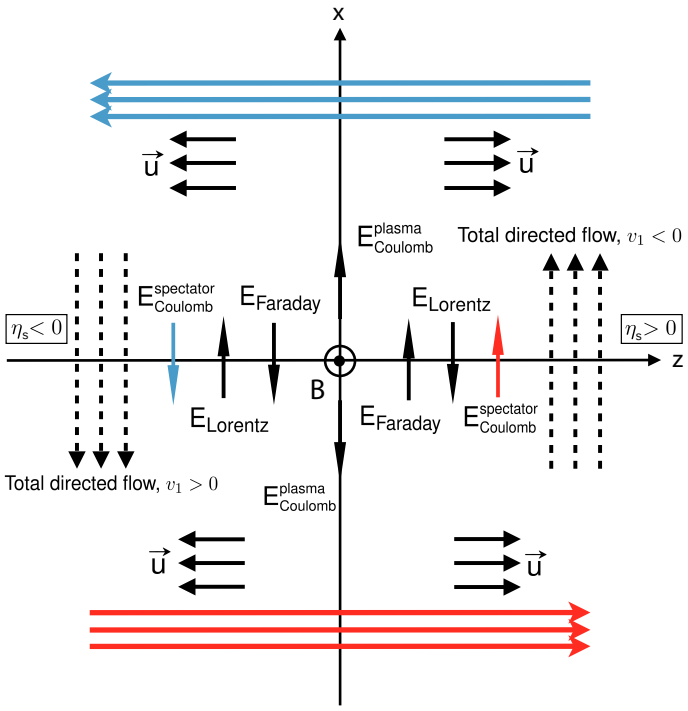

Figure 4.1: Illustration of the EM fields created

Inorder to think of computing the incremental drift velocity $\vec{v}_{\text{drift}}$ caused by the electromagnetic forces one should first computes the electric and magnetic fields $\vec{E}$ and $\vec{B}$, perhaps their origins. The possible origins of the created electric force are the flying spectators, the plasma itself and other two, of magnetic field origin. From the positively charged spectators that fly away the collision zone, there exist an electric force on the charged plasma produced; this is a direct coulomb sourced field. secondly, from the spectator nucleons and from the charge density deposited in the plasma by the nucleons participating in the collision, we have a non-vanishing outward-pointing component of the electric field already in the lab frame. thirdly, the hydrodynamic fluid exhibits a strong longitudinal flow velocity along the beam direction in the direction of which we have coulomb field; and because of the perpendicular magnetic field $\vec{B}$ created in the system there exist *Lorentz* force that can contribute to the directional pushes particles experience. Finally, there is an induced electric current because of the change in magnetic field *Faraday*. A more detailed explanation is given below from [102]. These four sources of electric forces which are of the *coulomb* ($\vec{E}_C$), *Lorentz:* ($\vec{E}_L$), *Faraday:* ($\vec{E}_F$) and *Plasma based*, are illustrated in Fig. 4.1.

1. *Faraday:* as the magnetic field decreases in time, Faraday's law dictates the induction of an electric field and, since the plasma includes mobile charges, an electric current [102]. At the beginning of the collision the only field that affect the expansion is the Coulomb electric field generated by the net charge in the plasma. We denote this electric field by $\vec{E}_F$. Since $\vec{E}_F$ curls around the (decreasing) $\vec{B}$ that points in the y-direction, the sideways component of E_F points in opposite directions at opposite rapidity.

2. *Lorentz:* since the hydrodynamic fluid exhibits a strong longitudinal flow velocity $\vec{v}_{\text{flow}}$ denoted by $\vec{u}$ in Fig. 4.1, which points along the beam direction (hence perpendicular to $\vec{B}$), the Lorentz force exerts a sideways push on charged particles in opposite directions at opposite rapidity. Equivalently, upon boosting to the local fluid rest frame in which the fluid is not moving, the lab frame $\vec{B}$ yields a fluid frame $\vec{E}$ whose effects on the charged components of the fluid are equivalent to the effects of the Lorentz force in the lab frame. We denote this electric field by $\vec{E}_L$. Both $\vec{E}_F$ and $\vec{E}_L$ are of magnetic origin.

3. *Coulomb:* The positively charged spectators that have passed the collision zone exert an electric force on the charged plasma produced in the collision, which again points in opposite directions at opposite rapidity. We denote this electric field by $\vec{E}_C$. The authors of Ref. [**?**] did identify this contribution and so did we in this work.

4. *Plasma:* There is a non-vanishing outward-pointing component of the electric field already in the lab frame, because the plasma (and the spectators) have a net positive charge. We denote this component of the electric field by $\vec{E}_P$, since its origin includes Coulomb forces within the plasma. At any collision energy considered, $\vec{E}_P$ receives contributions both from the spectator nucleons and from the charge density deposited in the plasma by the nucleons participating in the collision even though the magnitude differs. Before we dive in to working on the way to solve the Maxwell's equations lets drive back and dive in the development of the equations.

4.1.1 Static and Moving charges

In order to understand Maxwell's equations, it is necessary to understand some basic things about electricity and magnetism first. Static electricity is easy to understand, in that it is just a charge which, as its name implies, does not move until it is given the chance to "escape" by a force of repulsion or attraction with other charge(s). The force between two static charges is given by Coulomb's Law :

$$F = \frac{1}{4\pi\epsilon_0}\frac{q_1 \cdot q_2}{r^2} \tag{4.1}$$

Coulomb's Law is remarkably similar to the force of gravitational attraction, which is the same other than that charge is replaced by mass, and k is replaced with a new constant, g. That is useful for finding the attraction or repulsion between two charges, but is not as good if a third charge enters the problem. Because of this, it is useful to define electric fields.

$$E = \frac{F}{q} = \frac{1}{4\pi\epsilon_0}\frac{Q}{r^2} \tag{4.2}$$

Inorder to look at moving charges, imagine that charge was flowing through a conductor at the rate of $1C$ per second. This is defined as a current of one ampere, abbreviated amp, or A. The symbol for amps in an equation is I. From basic physics, work is defined as force times the distance moved perpendicular to the direction of the force: $W = F \times D$, and is measured in Joules. Joules are abbreviated J and are a measurement of energy, with $1J$ being a force of one Newton applied over a distance of one meter: $1J = N \cdot m$.

Electric fields are measured in Newtons per coulomb, but are not usually expressed like this; they are usually expressed in volts per meter. Voltage is a measure of electric potential - the amount of potential energy available per unit charge. Every point in space has an electric potential, with the general convention that a point infinitely far away from a charge has an electric potential of zero. If a charge of $1C$ is moved

over a potential difference of $1V$, $1J$ of work will be done, so the definition of a volt, abbreviated V, is $1V = 1J/C$. That is equivalent to $1V = N \cdot m/C$, so $1N/C = 1V/m$, and the units are equivalent.

4.2 Maxwell's Equations

4.2.1 Maxwell's Equations

The differential forms of Maxwell's equations as found by Heaviside, while completely valid, are now considered somewhat archaic, and have been replaced by the more useful (equivalent) integral forms. Each law is named according to the person(s) who originally discovered the connections represented by the equation. Here are the four equations:

$$\text{Gauss' law for electricity:} \quad \oint_{\substack{\text{closed}\\\text{surface}}} \vec{E} \cdot d\vec{A} = \frac{Q_{enc}}{\epsilon_0} \tag{4.3}$$

$$\text{Gauss' law for magnetism:} \quad \oint_{\substack{\text{closed}\\\text{surface}}} \vec{B} \cdot d\vec{A} = 0 \tag{4.4}$$

$$\text{Faraday's law:} \quad \oint \vec{E} \cdot d\vec{s} = -\frac{d\phi_B}{dt} \tag{4.5}$$

$$\text{Ampere-Maxwell law:} \quad \oint \vec{B} \cdot d\vec{s} = \mu_0\epsilon_0\frac{d\phi_E}{dt} + \mu_0 i_{enc} \tag{4.6}$$

Note: $\oint$ is used to specify a closed loop integral, also known as a line integral. It simply means that in the calculations, we must go all the way around the loop; we can't stop part way through or the equations won't be valid.

4.2.2 Gauss' law for electricity

Gauss' law for electricity, more commonly simply refered to as Gauss' law, states that the closed surface integral of $\vec{E} \cdot d\vec{A}$ is equal to the charge enclosed by the surface divided by the electric permittivity of the material the charge is in. Generally, the electric permittivity, denoted ϵ, is taken to be the electric permittivity of free (empty) space, and is written ϵ_0. ($\epsilon_0 \approx 8.85 \cdot 10^{-12} F/m$).

We are free to choose our "surface" - it's an imaginary construct for the purposes of doing the math, not a real entity. The most common surfaces chosen are spheres and cylinders, because mathematically, symmetry makes applying Gauss' law much easier, but theoretically, any closed surface can be chosen and it will give the exact same results.

Imagine a point charge of $+Q$ floating in space. Centered around this charge, construct a spherical Gaussian surface of radius R. Since the charge is centered in the sphere, the E field points radially outward and has the same magnitude at all points on the sphere. Remember that $E = \frac{1}{4\pi\epsilon_0}\frac{Q}{r^2}$. Since in this example, $r = R$, this equation becomes $E = \frac{1}{4\pi\epsilon_0}\frac{Q}{R^2}$.

From the definition of electric flux, $\phi_E = \oint\limits_{\substack{\text{closed}\\\text{surface}}} \vec{E} \cdot d\vec{A}$, so applying Gauss' law is a way of finding the electric flux through a surface due to a charge Q. $d\vec{A}$ is a unit vector normal to the surface at all points, and represents a tiny portion of the surface area of the Gaussian surface. The closed surface integral of $d\vec{A}$ is the surface area, A.

Again from the definition of electric flux,

$$\begin{aligned}
\phi_E &= \oint\limits_{\substack{\text{closed}\\\text{surface}}} \vec{E} \cdot d\vec{A} \\
E &= \frac{1}{4\pi\epsilon_0}\frac{Q}{R^2} \\
\phi_E &= \oint\limits_{\substack{\text{closed}\\\text{surface}}} \left(\frac{1}{4\pi\epsilon_0}\frac{Q}{R^2}\right) \cdot d\vec{A}
\end{aligned}$$

Since $\vec{E}$ is pointing radially outward everywhere, it is always parallel to $d\vec{A}$, and $\vec{E} \cdot d\vec{A}$ becomes $(\vec{E})d\vec{A}$. Since $\vec{E}$ is constant at all points on the sphere, it can be moved outside the integral:

$$\begin{aligned}
\phi_E &= \left(\frac{1}{4\pi\epsilon_0}\frac{Q}{R^2}\right) \oint\limits_{\substack{\text{closed}\\\text{surface}}} d\vec{A} \\
\phi_E &= \left(\frac{1}{4\pi\epsilon_0}\frac{Q}{R^2}\right) A
\end{aligned}$$

where A is the surface area of the sphere. However, the surface area of a sphere is simply $4\pi R^2$, so this becomes

$$\begin{aligned}
\phi_E &= \left(\frac{1}{4\pi\epsilon_0}\frac{Q}{R^2}\right)\left(4\pi R^2\right) \\
\phi_E &= \frac{Q}{\epsilon_0}
\end{aligned}$$

But this, of course, is simply Gauss' law! ϕ_E is independent of the radius of the sphere, which may seem strange, since $\vec{E}$ clearly decreases at a rate $\propto 1/R^2$; however, since $\vec{E}$ points away from the charge, no matter how large the radius of the sphere is, the electric field will still penetrate it at some point, and the flux will *have* to be the same. Mathematically, it works because ϕ_E is $\vec{E}$ multiplied by the surface area of the Gaussian surface; $\vec{E} \propto 1/R^2$, and $A \propto R^2$, so their product, ϕ_E must be independent of R.

Imagine that, instead placing a charge of $+Q$ inside the Gaussian surface, we placed outside. Clearly the electric field still points away from the charge, and at some point, the electric field will pass through the Gaussian surface. On one side of the surface, this will give a negative flux - the electric field is entering the surface! But the electric field will have to leave the Gaussian surface on the other side, creating a positive flux. Since all the field lines that enter the surface must leave again - they don't just stop - the net electric flux will be zero, as predicted by Gauss' law.

Using arguments of symmetry, it is also possible to prove Gauss' law for Gaussian surfaces of other shapes, such as cylinders. It can also be used "in reverse;" by dividing both sides of the equation by A after integrating, the electric field caused by various charge configurations can be found for all points in space. An example of this is finding the electric field at all points in space caused by an infinitely large plane of charge density ρ. It's done using a cylindrical Gaussian surface rather than a spherical one, and while the idea of an infinitely large plane is ridiculous, the results hold true as long as the distance from the plane at which the electric field is being calculated is significantly smaller than the size of the plane, and not near the edge.

4.2.3 Gauss' law for magnetism

Gauss' law for magnetism is remarkably similar to Gauss' law for electricity in form, but means something rather different. Imagine that a magnet was placed in space, and that a spherical Gaussian surface was constructed around it.

Remember from the section on magnetism that magnetic fields "flow," by convention, from the North pole of a magnet to the South pole. From the definition of magnetic flux, $\phi_B = \oint_{\substack{\text{closed} \\ \text{surface}}} \vec{B} \cdot d\vec{A}$. Part of the magnetic field will not pierce the Gaussian surface - this portion of the field clearly will not contribute to the flux through the surface, so it can be ignored. The rest of the magnetic field lines will leave through the surface from the North pole of the magnet, but because the field flows from the North pole to the South pole, the same field lines will enter the surface again somewhere on the surface to go to the South pole. Since the flux going out is equal to the flux coming in, the net flux is zero, as indicated by Gauss' law for magnetism.

Suppose that instead the magnet was placed outside the Gaussian surface. The same argument applies: any part of the magnetic field that enters the surface will have to leave again through the surface, since it

is closed. The positive flux will equal the negative flux, they'll cancel, and the net flux will be zero. Again, this matches what was predicted by Gauss' law.

Pretend that a special magnet with only a North pole, and no South pole, existed. This would be called a magnetic monopole. All the magnetic field lines would point away from this theoretical magnetic monopole, just like the electric field lines point away from a positive charge Q. If a Gaussian surface was constructed around this monopole, there would obviously be a positive flux going through the surface, because the magnetic field is leaving, and it isn't coming back in! Gauss' law for magnetism, however, very clearly says that the flux should be zero! This means that according to Gauss, there can be no magnetic monopoles - all magnets must have two poles. Although some people are looking for magnetic monopoles, none have ever been observed, and if one is ever found, it will mean that Gauss' law for magnetism is incorrect.

4.2.4 Faraday's law

According to the definition of magnetic flux, ϕ_B, a magnetic field passing through an area A will create magnetic flux. Imagine that a circular loop of wire of radius R is placed in a magnetic field $\vec{B}$, perpendicular to the direction of the field. The flux through the loop is clearly the strength of the magnetic field multiplied by the area of the loop: $\phi_B = \vec{B}\left(\pi R^2\right)$. Now imagine that the magnetic field began changing with time at a rate of $\frac{d\vec{B}}{dt}$. The change in flux with time would be $\frac{d\phi_B}{dt} = \left(\pi R^2\right)\frac{d\vec{B}}{dt}$. The flux could also be changed by altering the area of the loop, but since changing the area of the loop in real applications is not as practical as changing the magnetic field, and since the mathematics are largely similar, only the case of changing magnetic fields will be examined.

As was observed by Faraday, when ϕ_B through the loop is changing, a voltage is *induced* in the loop in an attempt by the system to "fight" the change. A current will then flow in the loop as determined by the Ohm's law, V=IR, where R is the resistance of the loop.

Consider again the scenario above. Faraday's law contains the integral of $\vec{E} \cdot d\vec{s}$. The $d\vec{s}$represents an infinitely small portion of the loop of wire. Recall that an electric field multiplied by a distance represents a voltage. We can go around the loop in either direction and it won't affect our results other than a change in sign - but that change in sign is to be expected, because in one direction, we would be increasing in potential as we went around, and in the other direction, we would be decreasing in potential! From Faraday's law, we have

$$\oint \vec{E} \cdot d\vec{s} \quad = \quad -\frac{d\phi_B}{dt}$$

Since $\vec{E}$ in the wire will always be parallel to $d\vec{s}$, the dot product of the two will turn into simple multiplication. Furthermore, since $\vec{E}$ is not dependent on $d\vec{s}$, we can move $\vec{E}$ outside the integral, and simply have the integral of $d\vec{s}$, which is nothing but the perimeter of the loop, $2\pi R$.

$$\begin{aligned} \vec{E} \oint d\vec{s} &= -\frac{d\phi_B}{dt} \\ \vec{E}\,(2\pi R) &= -\frac{d\phi_B}{dt} \end{aligned}$$

If, instead of having one loop of wire, we had n loops, the "area" enclosed by the loop, while harder to visualize, would be n times greater, and hence the change in flux would also be n times greater, and the equation would become

$$\vec{E}\,(2\pi R) = -n\frac{d\phi_B}{dt}$$

The negative sign in this equation is because of Lenz's Law, which essentially states that a negative sign is needed in this equation because otherwise it would be possible to violate Conservation of Energy. However, it only affects the direction of the current that flows because of the induced voltage, not the magnitude. Since the direction of the current is normally determined with a right hand rule, the negative sign can be ignored in the calculations without causing any serious consequences. The right hand rule for determining the direction of current goes as follows: point the thumb of the right hand in the direction of the changing flux. For example, if the magnetic field points up, and is decreasing, the thumb would be pointed down. If the field were increasing, the thumb would be pointed up. When this is done, the fingers of the right hand will curl in the direction of the flow of current in the loop.

4.2.5 Ampere-Maxwell law

Ampere observed that currrent flowing through a wire created a magnetic field around the wire, and formulated the equation

$$\oint \vec{B} \cdot d\vec{s} = \mu_0 i_{enc} \tag{4.7}$$

i_{enc}, meaning current enclosed, is perhaps a deceptive notation. Current can not be "enclosed;" rather, what is meant is the current that passes through the interior of the closed loop. $\mu_0$is a constant called the magnetic permeability of free space; if there is a material present instead of simply space, $\mu_0$is replaced with μ for the material.

Ampere's law is used by simply selecting any closed loop, traversing it with small elements $d\vec{s}$, and solving the resulting equation. It is key to note that *any* closed loop can be selected - a flat disc, or perhaps a shape more similar to a grocery bag - and it will give the same results.

Ampere's law predicted the magnetic field very accurately, but Maxwell noticed that there was a piece missing.

Maxwell named the missing term "displacement current," even though it is not really a current at all, but rather is the changing electric field within the capacitor. Since charge is accumulating on the plates of the capacitor, there is a changing electric field between the two plates. By introducing the term $\mu_0\epsilon_0\frac{dphie}{dt}$, Maxwell completed the equation, now called the Ampere-Maxwell law:

$$(\oint \vec{B}\cdot d\vec{s}) \quad = \quad (S\mu_0\epsilon_0\frac{d\phi_E}{dt} + \mu_0 i_e nc)$$

With his final addition to Ampere's law, and the formulation of the other three laws, Maxwell completed the theory of electricity and magnetism. Remarkably, using only the four equations known as Maxwell's equations,

4.3 Solving Maxwell's Equation

The electromagnetic fields generated by a point-like charge moving in the +z-direction with velocity v can be governed by the following wave equations [102].

$$\nabla^2\vec{B} - \partial_t^2\vec{B} - \sigma\partial_t\vec{B} = -\vec{\nabla}\times\vec{J}_{\rm ext} \tag{4.8}$$

$$\nabla^2\vec{E} - \sigma_t^2\vec{E} - \sigma\partial_t\vec{E} = \frac{1}{\epsilon}\vec{\nabla}\rho_{\rm ext} + \partial_t\vec{J}_{\rm ext} \tag{4.9}$$

Where the external charge and current sources for the electromagnetic fields [102] which are a function of the rapidity of those flying and interacting particles are then given by :

$$\rho_{\rm ext}(\vec{x}_\perp,\eta_s) = \rho^+_{\rm ext}(\vec{x}_\perp,\eta_s) + \rho^-_{\rm ext}(\vec{x}_\perp,\eta_s) \tag{4.10}$$

$$\vec{J}_{\rm ext}(\vec{x}_\perp,\eta_s) = \vec{J}^+_{\rm ext}(\vec{x}_\perp,\eta_s) + \vec{J}^-_{\rm ext}(\vec{x}_\perp,\eta_s) \tag{4.11}$$

Solving the above wave equations happens to be easy since we have considered the electrical conductivity of the QGP to be constant, but making it time varying, which in reality is, because of its dependence on

the temperature of the system would make it very hard and is what we anticipate to work on next. So we took four different σ values $\sigma = 0.023$ fm^{-1}, $\sigma = 0.4$ fm^{-1}, $\sigma = 0.66$ fm^{-1} and $\sigma = 1.1$ fm^{-1} to have a chance of analyzing its effect. And the numerical code for calculating the electromagnetic fields is same as in [102]. For the evolution of the relativistic viscous hydro-dynamics, we choose the s95p-v1-PCE equation of state from Ref. [114]. After having the field evolution known the next imediate step is to work on what drift velocity this field causes and this can be done by solving the force balance equation.

4.4 The Equation of Motion

The drift velocity at each point on the freeze-out surface from the electromagnetic field evolution can be calculated after solving the force balance equation [102]:

$$m\frac{d\vec{v}^{\,\mathrm{lrf}}_{\mathrm{drift}}}{dt} = q\vec{v}^{\,\mathrm{lrf}}_{\mathrm{drift}} \times \vec{B}^{\,\mathrm{lrf}} + q\vec{E}^{\,\mathrm{lrf}} - \mu m\vec{v}^{\,\mathrm{lrf}}_{\mathrm{drift}} = 0 \tag{4.12}$$

The last term in (4.12) describes the drag force on a fluid element with mass m on which some external (in this case electromagnetic) force is being exerted, with μ the drag coefficient. Even−though the drag coefficient still is not clear, at present its value is known precisely only for heavy quarks in $\mathcal{N} = 4$ SYM theory; following [102, 114]. We investigate the force balance equation from which we get the drift velocity $\vec{v}^{\,\mathrm{lrf}}_{\mathrm{drift}}$ in every fluid cell along the freeze-out surface. After having the drift velocity we are expected to mesh it up with the usual hydrodynamic flow velocity and feed that to get the particles increase or just change in velocity from the particle sampler.

4.5 Concluding Remarks

The code for calculating the electromagnetic fields solves the Maxwell's equation and needs to know the initial information about the spectators density from the initial condition generator, nuclear thickness and the surface freezout from the hydro code so that it gets all the information to calculate the fields and then evaluate the force balance equation to give us the net drift velocity generated by the field forces. Then the outputs from both the hydro and field calculator serve as input for the particle sampler.

Chapter 5: The Model Setup Description

5.1 Chapter Introduction

A nucleus-nucleus collision at relativistic energy passes through different stages [105]. Inorder to simulate this dynamical evolution of the medium produced in heavy ion collision, we have used the iEBE-VISHNU framework as in [106]. This Frame work includes all the evolution from pre-equilibrium dynamics to the free streaming but here in our current work there sure is a clear need to find out the electromagnetic fields generated by both the spectators and participant particles as in [13, 68, 102, 104]. In this chapter we will be going through the packages in detail. In this hybrid package, there is a specific code simulating each stage of the evolution and a script to link all the individual programs together. There are four major components of the package and in our case as in [102], we need to add electromagnetic field simulator and blend it with the rest: So the major components would be

1. `superMC` : the initial condition generator
2. `VISHNew` : a (2+1)-d viscous hydrodynamic simulator
3. Electromagnetic field simulator
4. `iSS` : a particle sampler and
5. `UrQMD` : a hadron cascade simulator

The hydrodynamic framework which is the Israel-Stewart 2nd order formalism has started being used for relativistic dissipative fluid dynamics in just the past ten years. Currently the available viscous hydrodynamics codes ranges from $1 + 1$s dimensions (2+1) dimensions and (3+1)-d viscous hydrodynamics. Here the first number indicates the number of spatial dimensions in which the code solves numerically for the evolution of the hydrodynamic fields, and the +1 stand for time. All existing codes assume longitudinal boost invariance, which allows to treat the longitudinal expansion along the beam direction analytically. This is a good approximation at RHIC and LHC energies for particle production near midrapidity. (1+1)-d codes assume additionally azimuthal symmetry around the beam axis, allowing spatial expansion in the radial direction. With them, we can only simulate heavy ion collisions with zero impact parameter. To describe

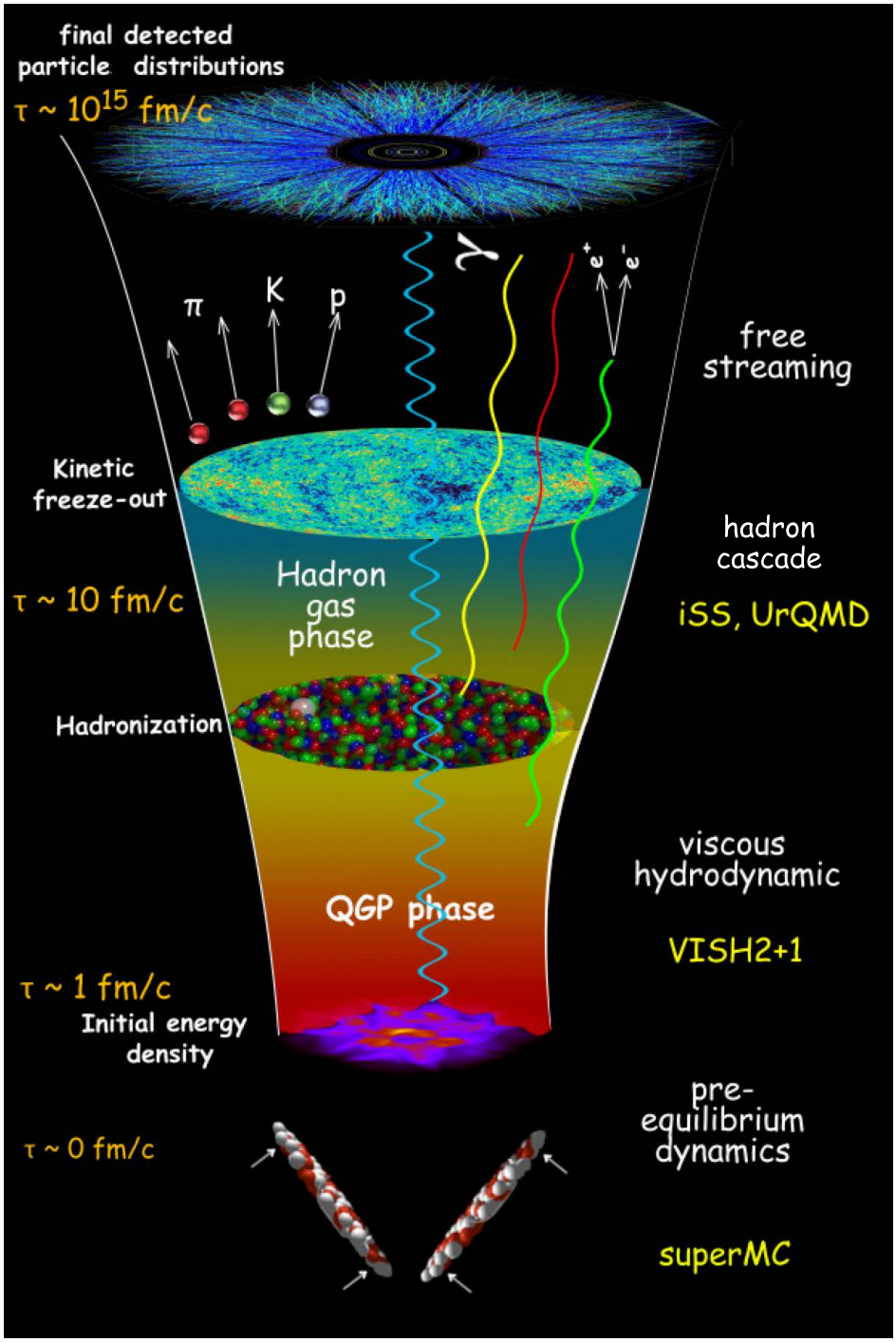

Figure 5.1: Illustration of the evolution of the fireball created in relativistic heavy-ion collisions, together with the theoret- ical model used in each stage [106].

non-central collisions, and in particular anisotropic (elliptic) flow, requires a (2+1)-d code, which allows for anisotropic expansion in the two dimensions transverse to the beam. Let′s have a look in to the ingredients

5.2 Initial conditions

The initialization of a hydrodynamic simulation requires a starting time τ_0 and initial profiles for the energy momentum tensor $T^{\tau\tau}$, $T^{\tau x}$ and $T^{\tau y}$, which are given by the initializations for the energy density, velocity and stress stress tensor π^{mn}. Through all of this thesis, we set $\tau_0 = 0.6$ fm/c, following the "standard" thermalization time used in most ideal hydrodynamic simulations [6], and we use zero initial transverse flow velocity. We have not explored the need for rescaling τ_0 when including viscosity; this awaits a careful comparison with the experimental data. The initializations for energy density and π^{mn} profiles are described below.

5.2.1 Initializations for the energy density

Glauber model initialization

A simple Glauber model initialization assumes that the initial energy density in the transverse plane is proportional to the wounded nucleon density:

$$\begin{aligned} e_0(x,y;b) &= K n_{\mathrm{WN}}(x,y;b) \\ &= K\Big\{ T_A\big(x+\tfrac{b}{2},y\big)\Big[1-\Big(1-\frac{1-\sigma T_B\left(x-\frac{b}{2},y\right)}{B}\Big)^B\Big] \\ &\quad + T_B\big(x-\tfrac{b}{2},y\big)\Big[1-\Big(1-\frac{1-\sigma T_A\left(x+\frac{b}{2},y\right)}{A}\Big)^A\Big]\Big\}. \end{aligned} \tag{5.1}$$

Here σ is the total inelastic nucleon-nucleon cross section for which we take $\sigma = 40\,\mathrm{mb}$. $T_{A,B}$ is the nuclear thickness function of the incoming nucleus A or B, defined as $T_A(x,y) = \int_{-\infty}^{\infty} dz \rho_A(x,y,z)$; $\rho_A(x,y,z)$ is the nuclear density given by a Woods-Saxon profile: $\rho_A(\boldsymbol{r}) = \frac{\rho_0}{1+\exp[(r-R_A)/\xi]}$. We take $R_{\mathrm{Cu}} = 4.2\,\mathrm{fm}$, $\xi = 0.596\,\mathrm{fm}$ for Cu+Cu collisions and $R_{\mathrm{Au}} = 6.37\,\mathrm{fm}$, $\xi = 0.56\,\mathrm{fm}$ for Au+Au collisions (these two parameter sets for Au and Cu nuclei correspond to a nuclear density $\rho_0 = 0.17\,\mathrm{fm}^{-3}$). The proportionality constant K does not depend on collision centrality but on collision energy; it fixes the overall scale of the initial energy density and, via the associated entropy, the final hadron multiplicity to which it must be fitted as a function of collision energy. The energy density profile for specific collision energy is therefore normalized by a parameter $e_0(\tau = \tau_0, r = b = 0)$ giving the peak energy density in the center of the fireball for central collisions (impact parameter b = 0). For central Au+Au collisions at top RHIC energies, one sets $e_0 \equiv e(0,0;b{=}0) = 30$ GeV/fm^3 and $\tau_0 = 0.6$ fm/c to reproduce the final multiplicity in ideal hydrodynamic

calculations. In the viscous hydrodynamics comparison runs, we use the same initialization as for ideal hydrodynamics. Viscous entropy production then leads to slightly larger final multiplicities than in ideal hydrodynamics. Again, we leave a corresponding retuning of initial conditions to a careful comparison study with experimental data. The Glauber initialization (5.1) does not correctly reproduce the measured centrality dependence of dN_{ch}/dy [64]. To fix this problem, more sophisticated initialization schemes have been developed [64], where one uses a superposition of wounded nucleon and binary collision densities. We also leave this for future data comparisons.

Color glass condensate (CGC) initialization

The CGC initialization based on the Kharzeev-Levin-Nardi (KLN) approach and its more recent fKLN improvement has been applied in earlier ideal hydrodynamic calculations and recently also in viscous hydrodynamic calculations. Details of the CGC initialization can be found in Ref. [60].

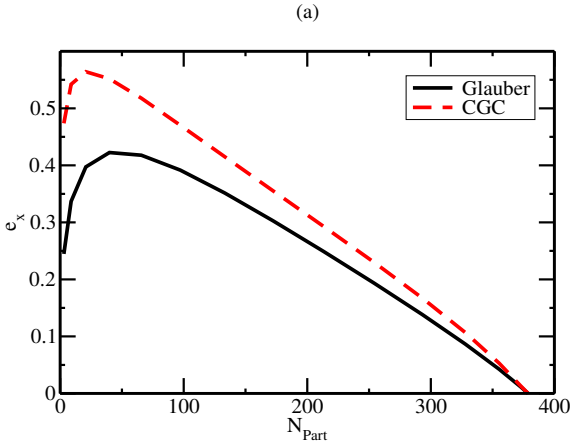

Figure 5.2: The initial eccentricity ε_x from Glauber and CGC initializations, for Au+Au collisions at different centrality [60].

Compared with the Glauber initialization, the CGC initialization gives a more "plateau-like" initial profile for the energy density, which leads to larger initial eccentricity $\varepsilon_x = \frac{\langle y^2 - x^2 \rangle}{\langle x^2 + y^2 \rangle}$ than for the Glauber model. Fig.5.2 shows the initial eccentricity ε_x from the Glauber and fKLN initializations. One finds that the CGC initialization predicts $20 - 50\%$ larger initial eccentricity than the Glauber one, especially at small impact parameters, where the eccentricity is small but the discrepancy between models is large [60] .

5.2.2 Initializations for π^{mn} and Π

Lacking a microscopic dynamical theory for the early pre-equilibrium stage, initializing the viscous pressure tensor π^{mn} requires some guess-work. We here explore two options: (i) zero initialization, which sets $\pi_0^{mn}=0$ at initial time τ_0 [50, 65]. (ii)(Navier- Stokes) N-S initialization: $\pi_0^{mn}=2\eta\sigma_0^{mn}$, where the shear tensor σ_0^{mn} is calculated from the initial velocity profile $u^m=(1,0,0,0)$. The second option is the default choice for most of the results shown in this thesis. It gives $\tau^2\pi_0^{\eta\eta}=-2\pi_0^{xx}=-2\pi_0^{yy}=-\frac{4\eta}{3\tau_0}$, i.e. a negative contribution to the longitudinal pressure and a positive contribution to the transverse pressure.

5.3 The equation of state (EOS)

The equation of state (EoS), which relates the pressure p to energy density e and net baryon density n_B: $p=p(n_B,e)$ (or equivalently relates it to temperature T and net baryon chemical potential μ_B, $p=p(T,\mu_B)$) is a necessary input for both ideal and viscous hydrodynamic simulations. In this section, we will describe the different EoS used in this thesis. Currently, all of the existing viscous hydrodynamics calculation neglect net baryon density and set $n_B=0$. The EoS described below thus reduces to a simple one dimensional EOS: $p=p(e)$.

EOS I:

EOS I models a non-interacting gas of massless quarks and gluons, with $p=\frac{1}{3}e$. It has no phase transition. Where needed, the temperature is extracted from the energy density via the relation $e=\left(16+\frac{21}{2}N_f\right)\frac{\pi^2}{30}\frac{T^4}{(\hbar c)^3}$, corresponding to a chemically equilibrated QGP with $N_f=2.5$ effective massless quark flavors.

EOS Q:

EOS Q connects a noninteracting massless QGP gas to a chemically equilibrated hadron resonance gas through a first order phase transition. The EOS in the QGP phase is defined by $p=\frac{1}{3}e-\frac{4}{3}B$ (i.e. $c_s^2=\frac{\partial p}{\partial e}=\frac{1}{3}$). The vacuum energy (bag constant) $B^{1/4}=230\,\mathrm{MeV}$ is a parameter that is adjusted to yield a critical temperature $T_c=164\,\mathrm{MeV}$. The hadron resonance gas below T_c can be approximately characterized by the relation $p=0.15\,e$ (i.e. $c_s^2=0.15$). The two sides are matched through a Maxwell construction, yielding a relatively large latent heat $\Delta e_{\mathrm{lat}}=1.15\,\mathrm{GeV/fm^3}$. For energy densities between $e_{\mathrm{H}}=0.45\,\mathrm{GeV/fm^3}$ and $e_{\mathrm{Q}}=1.6\,\mathrm{GeV/fm^3}$ one has a mixed phase with constant pressure (i.e. $c_s^2=0$).

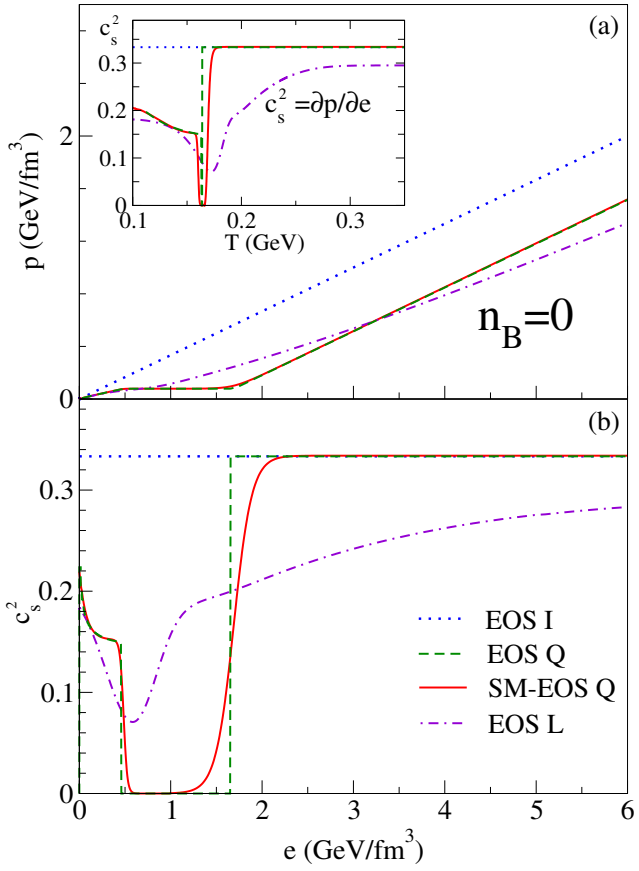

Figure 5.3: The equation of state. Panel (a) shows the pressure p as a function of energy density e and (in the inset) the squared speed of sound $c_s^2 = \frac{\partial p}{\partial e}$ as a function of temperature T, for EOS I, EOS Q, SM-EOS Q and EOS L. Panel (b) shows c_s^2 as a function of energy density e for different EOS.

SM-EOS Q:

SM-EOS Q is a smoothed version of EOS Q. The discontinuous jumps of c_s^2 in EOS Q from a value of 1/3 to 0 at $e_{\rm Q}$ and back from 0 to 0.15 at $e_{\rm H}$ generate propagating numerical errors in VISH2+1 which grow with time and cause problems. We avoid these by smoothing the function $c_s^2(e)$ with a Fermi distribution of width $\delta e = 0.1\,{\rm GeV/fm^3}$ centered at $e = e_{\rm Q}$ and another one of width $\delta e = 0.02\,{\rm GeV/fm^3}$ centered at $e = e_{\rm H}$ [60].

EOS L:

EOS L matches the hadron resonance gas below T_c smoothly in a rapid cross-over transition to lattice QCD data above T_c. For the fit, the lattice data were plotted in the form $p(e)$, interpolated and then smoothly joined to the $p(e)$ curve of the HRG with a cross-over transition near $T_c \sim 175MeV$. As can be seen in the upper panel of Fig. 5.3 in the inset, our procedure is not fully thermodynamically consistent and leads to a somewhat different temperature dependence of c_s^2 below T_c than for EOS Q and SM-EOS Q. Since

this only affects the flow dynamics below our decoupling temperature of $T_{dec} = 130\,\mathrm{MeV}$, we have not put any effort into correcting this [60].

PCE-EOS for the HRG phase:

EOS Q assumes that chemical and thermal freeze-out happen at the same temperature $T_{\mathrm{th}} \sim 130$ MeV. However, the experimental data indicate that chemical freeze-out happens earlier near $T_c \sim 165$ $mathrmMeV$. The unrealistic implementation of chemical freeze-out in EOS Q leads to wrong predictions for the particle ratios which need to be fixed by hand using normalization factors. Microscopically, chemical and thermal freeze-out are related to inelastic and total (elastic + quasi-elastic + inelastic) scattering rates between particles, respectively. The cross sections of the inelastic, particle number changing processes, are smaller than the elastic and quasi-elastic ones, which leads to an earlier chemical than thermal freeze-out [66]. A complete chemical freeze-out corresponds to a picture where all hadron numbers are fixed below T_{ch}. However, quasi-elastic resonant scatterings constantly change resonances and their daughter particles (e.g. $\pi\pi \to \rho \to \pi\pi$, $\pi N \to \Delta \to \pi N$, $\pi K \to K^* \to \pi K$, etc.), such that the resonances are in relative chemical equilibrium with their decay products and their abundances only freeze out at thermal decoupling. This partial chemical equilibrium picture is naturally incorporated in any hadron cascade model, that solves the Boltzmann equations with elastic, quasi-elastic and inelastic cross sections for different hadron species. In pure hydrodynamic simulations it is realized by introducing an EOS describing partially chemical equilibrium (PCE-EOS) with effective chemical potentials adjusted to conserve the relative hadron abundances after resonance decays in the HRG phase. Although the effective chemical potentials only slightly change the equation of state $p(e)$, they affect significantly the relation between temperature and energy density $T(e)$ in the HRG phase, since a larger portion of the energy density is stored in particle rest masses, reducing the thermal energy and temperature. As a result, the typical freeze-out temperature drops from 130 MeV (EOS Q) to 100 MeV (PCE-EOS) for the same freeze-out energy density $e_{dec} = 0.085$ GeV/fm^3.

5.4 The equations of motion

For ease of numerical implementation, the current viscous hydrodynamic calculations focus on boost-invariant systems, realized by assuming a specific "scaling" velocity profile $v_z = z/t$ along the beam direction. As given by Bjorken, this profile is a solution of the hydrodynamic equations (ideal or viscous) if the initial conditions are independent of the longitudinal reference frame (boost invariance), i.e. do not depend on

space-time rapidity η. After implementing the Bjorken approximation, the (3+1)-d viscous hydrodynamics reduces to (2+1)-d viscous hydrodynamics with boost invariance. Currently, all of the existing (2+1)-d viscous hydrodynamic codes also assume zero net baryon density and zero heat conductivity. These conditions are approximately realized in experiments at top RHIC and LHC energies and simplify the implementation further by eliminating the need to solve for the flows of baryon number and heat.

Longitudinally boost-invariant systems are conveniently described in curvilinear coordinates $x^m = (\tau, x, y, \eta)$, where $\tau = \sqrt{t^2 - z^2}$ is the longitudinal proper time, $\eta = \frac{1}{2}\ln\left(\frac{t+z}{t-z}\right)$ is the space-time rapidity, and (x, y) are the usual Cartesian coordinates in the plane transverse to the beam direction z. In this coordinate system, the transport equations for the full energy momentum tensor $T^{\mu\nu}$ are written as [2]:

$$\partial_\tau \widetilde{T}^{\tau\tau} + \partial_x(v_x \widetilde{T}^{\tau\tau}) + \partial_y(v_y \widetilde{T}^{\tau\tau}) = \mathcal{S}^{\tau\tau}, \tag{5.2a}$$

$$\partial_\tau \widetilde{T}^{\tau x} + \partial_x(v_x \widetilde{T}^{\tau x}) + \partial_y(v_y \widetilde{T}^{\tau x}) = \mathcal{S}^{\tau x}, \tag{5.2b}$$

$$\partial_\tau \widetilde{T}^{\tau y} + \partial_x(v_x \widetilde{T}^{\tau y}) + \partial_y(v_y \widetilde{T}^{\tau y}) = \mathcal{S}^{\tau y}. \tag{5.2c}$$

Here $\widetilde{T}^{mn} \equiv \tau(T_0^{mn} + \pi^{mn} - \Pi\Delta^{mn})$, $T_0^{mn} = eu^m u^n - p\Delta^{mn}$ being the ideal fluid contribution, $u^m = (u^\tau, u^x, u^y, 0) = \gamma_\perp(1, v_x, v_y, 0)$ is the flow profile (with $\gamma_\perp = \frac{1}{\sqrt{1-v_x^2-v_y^2}}$), and $g^{mn} = \mathrm{diag}(1, -1, -1, -1/\tau^2)$ is the metric tensor for our coordinate system. The source terms $\mathcal{S}^{mn}$ on the right hand side of Eqs. (5.2) are given explicitly as

$$\begin{aligned}\mathcal{S}^{\tau\tau} = &-(p + \Pi) - \tau^2\pi^{\eta\eta} - \tau\partial_x(pv_x + \Pi v_x + \pi^{x\tau} - v_x\pi^{\tau\tau}) \\ &- \tau\partial_y(pv_y + \Pi v_y + \pi^{y\tau} - v_y\pi^{\tau\tau}),\end{aligned} \tag{5.3a}$$

$$\mathcal{S}^{\tau x} = -\tau\partial_x(p + \Pi + \pi^{xx} - v_x\pi^{\tau x}) - \tau\partial_y(\pi^{xy} - v_y\pi^{\tau x}), \tag{5.3b}$$

$$\mathcal{S}^{\tau y} = -\tau\partial_x(\pi^{xy} - v_x\pi^{\tau y}) - \tau\partial_y(p + \Pi + \pi^{yy} - v_y\pi^{\tau y}). \tag{5.3c}$$

The transport equations for the shear pressure tensor and bulk pressure in 2+1 dimensions are written as [**?**, **?**]:

$$D\tilde{\pi}^{mn} = -\frac{1}{\tau_\pi}(\tilde{\pi}^{mn} - 2\eta\tilde{\sigma}^{mn}) - (u^m\tilde{\pi}^{nk} + u^n\tilde{\pi}^{mk})Du_k - \frac{1}{2}\tilde{\pi}^{mn}\frac{\eta T}{\tau_\pi}d_k\left(\frac{\tau_\pi}{\eta T}u^k\right), \tag{5.4a}$$

$$D\Pi = -\frac{1}{\tau_\Pi}(\Pi - \zeta\theta) - \frac{1}{2}\Pi\frac{\eta T}{\tau_\Pi}d_k\left(\frac{\tau_\Pi}{\eta T}u^k\right), \tag{5.4b}$$

Here, the explicit (2+1)-d form for the full "I-S equations" is written out. Even though several components of the symmetric shear pressure tensor π^{mn} are redundant [63] on account of its tracelessness and transversality to the flow velocity u^m, VISH2+1 propagates all 7 non-zero components and uses the tracelessness and transversality conditions as checks of the numerical accuracy.

5.5 Freeze-out procedure and calculation of spectra

The hadron spectra are computed from the hydrodynamic output via a modified Cooper-Frye procedure. We here compute spectra only for directly emitted particles and do not include feeddown from resonance decays after freeze-out. We first determine the freeze-out surface $\Sigma(x)$, by postulating (as common in hydrodynamic studies) that freeze-out from a thermalized fluid to free-streaming, non-interacting particles happens suddenly when the temperature drops below a critical value. As in the ideal fluid case with EOS Q we choose $T_{\rm dec} = 130\,\mathrm{MeV}$. The particle spectrum is then computed as an integral over this surface [60],

$$\begin{aligned} E\frac{d^3N_i}{d^3p} &= \frac{g_i}{(2\pi)^3}\int_\Sigma p\cdot d^3\sigma(x)\, f_i(x,p) \\ &= \frac{g_i}{(2\pi)^3}\int_\Sigma p\cdot d^3\sigma(x)\, [f_{{\rm eq},i}(x,p) + \delta f_i(x,p)]\,, \end{aligned} \tag{5.5}$$

where g_i is the spin-isospin degeneracy factor for particle species i, $d^3\sigma^\mu(x)$ is the outward-pointing surface normal vector on the decoupling surface $\Sigma(x)$ at point x, which for boost-invariant freeze-out at longitudinal proper time τ_f(r) reads

$$p\cdot d^3\sigma(x) = \left[m_T\cosh(y-\eta) - \boldsymbol{p}_\perp\cdot\boldsymbol{\nabla}_\perp\tau_f(\boldsymbol{r})\right]\times\tau_f(\boldsymbol{r})\, r dr\, d\phi\, d\eta, \tag{5.6}$$

(with $\boldsymbol{r} = (x,y) = (r\cos\phi, r\sin\phi)$ denoting the transverse position vector), and $f_i(x,p)$ is the local distribution function for particle species i, computed from the hydrodynamic output. Equation (5.5) generalizes the usual Cooper-Frye prescription for ideal fluid dynamics by accounting for the fact that in a viscous fluid the local distribution function is never exactly in local equilibrium, but deviates from its local equilibrium form by small terms proportional to the non-equilibrium viscous flows. Both contributions can be extracted from hydrodynamic output along the freeze-out surface. The equilibrium contribution is

$$f_{{\rm eq},i}(p,x) = f_{{\rm eq},i}\Big(\frac{p\cdot u(x)}{T(x)}\Big) = \frac{1}{e^{p\cdot u(x)/T(x)}\pm 1}, \tag{5.7}$$

where the exponent is computed from the temperature $T(x)$ and hydrodynamic flow velocity $u^\mu = \gamma_\perp(\cosh\eta, v_x, v_y, \sinh\eta)$ along the surface $\Sigma(x)$:

The viscous correction is proportional to $\pi^{\mu\nu}(x)$ on the freeze-out surface (normalized by the equilibrium enthalpy $e+p$) and increases quadratically with the particle's momentum (normalized by the temperature T). At large p_T, the viscous correction can exceed the equilibrium contribution, indicating a breakdown of viscous hydrodynamics. In that domain, particle spectra can not be reliably computed with viscous fluid dynamics. The limit of applicability depends on the actual value of $\pi^{\mu\nu}/(e+p)$ and thus on the specific dynamical conditions encountered in the heavy-ion collision.

The final expression for viscous correction to the spectrum are written explicitly as:

$$\begin{aligned} p_\mu p_\nu \pi^{\mu\nu} &= m_T^2\big(\cosh^2(y-\eta)\pi^{\tau\tau} + \sinh^2(y-\eta)\tau^2\pi^{\eta\eta}\big) \\ &- 2m_T\cosh(y-\eta)\big(p_x\pi^{\tau x} + p_y\pi^{\tau y}\big) \\ &+ \big(p_x^2\pi^{xx} + 2p_xp_y\pi^{xy} + p_y^2\pi^{yy}\big). \end{aligned} \tag{5.8}$$

Due to longitudinal boost-invariance, the integration over space-time rapidity η in Eq. (5.5) can be done analytically, resulting in a series of contributions involving modified Bessel functions. VISH2+1 does not exploit this possibility and instead performs this and all other integrations for the spectra numerically [60].

Once the spectrum (5.5) has been computed, a Fourier decomposition with respect to the azimuthal angle ϕ_p yields the anisotropic flow coefficients. For collisions between equal spherical nuclei followed by longitudinally boost-invariant expansion of the collision fireball, only even-numbered coefficients contribute, the "elliptic flow" v_2 being the largest and most important one:

$$E\frac{d^3N_i}{d^3p}(b) = \frac{dN_i}{dy\,p_T dp_T\,d\phi_p}(b) = \frac{1}{2\pi}\frac{dN_i}{dy\,p_T dp_T}\big[1 + 2v_2(p_T;b)\cos(2\phi_p) + \ldots\big]. \tag{5.9}$$

In practice it is evaluated as the $\cos(2\phi_p)$-moment of the final particle spectrum,

$$v_2(p_T) = \langle\cos(2\phi_p)\rangle \equiv \frac{\int d\phi_p\,\cos(2\phi_p)\,\frac{dN}{dy\,p_T dp_T\,d\phi_p}}{\int d\phi_p\,\frac{dN}{dy\,p_T dp_T\,d\phi_p}}\,, \tag{5.10}$$

where, according to Eq. (5.5), the particle spectrum is a sum of a local equilibrium and a non-equilibrium contribution (to be indicated symbolically as $N = N_{\rm eq} + \delta N$).

5.6 Additional viscous inputs

The shear viscosity η, bulk viscosity ζ and their relaxation times τ_π and τ_Π are free inputs in viscous hydrodynamic calculations.

Although the future trend for viscous hydrodynamic calculations will be to input a temperature dependent η/s to consider the fact that η/s is small in the QGP phase, reaches a minimum during the phase transition and rises again to much larger values in the hadronic phase (see Chap. 1.4 for details), all of the presently existing viscous hydrodynamic calculations (including those presented here) use a constant η/s as input: $\eta/s = C \times \frac{1}{4\pi}$, with $C = 0,\ 1,\ 2,\ 3$ ... ($\frac{1}{4\pi}$ is the minimal KSS bound from AdS/CFT [43]). Typically, we set $\tau_\pi = \frac{3\eta}{sT}$, except where mentioned otherwise. This expression is very close to the AdS/CFT prediction $\tau_\pi = \frac{2-\ln 2}{2\pi T}$, and is half of the kinetic theory prediction for massless Boltzmann particles.

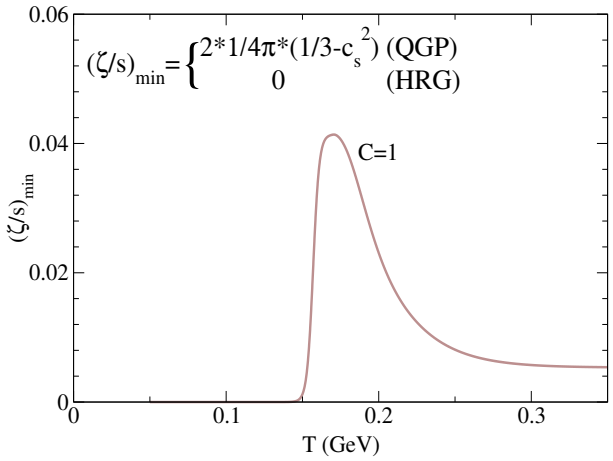

Figure 5.4: Minimally constructed bulk viscosity to entropy ratio, ζ/s, as a function of temperature.

The bulk viscosity of the QCD matter is still under theoretical development (see Chap. 1.4, 1.5 for details). It is generally believed that ζ/s peaks near the phase transition. However, one finds that the minimal peak value from AdS/CFT predictions is more than 10 times smaller than the one extracted from lattice QCD data. When neglecting hadron masses, chiral perturbation theory predicts a rising $(\zeta/s)(T)$ below T_c. In contrast, a theory with non-zero hadron masses shows a decreasing $(\zeta/s)(T)$ below T_c. Considering these theoretical uncertainties, ζ/s here is treated as a free input. We concentrate on the bulk viscosity effects near the phase transition, but totally neglect bulk viscosity effects in the hadronic matter. Fig. 5.4 shows the minimally constructed $(\zeta/s)_{min}$, which is obtained by connecting the minimal strong coupling AdS/CFT result $\zeta/s = 2(\eta/s)(1/3 - c_s^2)$ above T_c through a Gaussian function peaked at T_c with a zero value in the

hadronic phase (the speed of sound, $c_s^2(T)$, is evaluated from the same lattice QCD data [**?**] that are used in our EOS L). To simulate effects from larger bulk viscosity, we multiply the entire function $(\zeta/s)_{min}(T_c)$ by a constant $C > 1$. For the bulk relaxation time τ_Π, there are no standard theoretical results [60].

5.7 Details of the viscous hydro code VISH2+1

5.7.1 Expressions for $\tilde{\pi}^{mn}$ and $\tilde{\sigma}^{mn}$

The expressions for $\tilde{\pi}^{mn}$ and $\tilde{\sigma}^{mn}$ in eq. (5.4) are

$$\tilde{\pi}^{mn} = \begin{pmatrix} \pi^{\tau\tau} & \pi^{\tau x} & \pi^{\tau y} & 0 \\ \pi^{\tau x} & \pi^{xx} & \pi^{xy} & 0 \\ \pi^{\tau y} & \pi^{xy} & \pi^{yy} & 0 \\ 0 & 0 & 0 & \tau^2\pi^{\eta\eta} \end{pmatrix}, \tag{5.11}$$

$$\begin{aligned} \tilde{\sigma}^{mn} \quad = \quad & \begin{pmatrix} \partial_\tau u^\tau & \frac{\partial_\tau u^x - \partial_x u^\tau}{2} & \frac{\partial_\tau u^y - \partial_y u^\tau}{2} & 0 \\ \frac{\partial_\tau u^x - \partial_x u^\tau}{2} & -\partial_x u^x & -\frac{\partial_x u^y + \partial_y u^x}{2} & 0 \\ \frac{\partial_\tau u^y - \partial_y u^\tau}{2} & -\frac{\partial_x u^y + \partial_y u^x}{2} & -\partial_y u^y & 0 \\ 0 & 0 & 0 & -\frac{u^\tau}{\tau} \end{pmatrix} \\ & -\frac{1}{2}\begin{pmatrix} D\left((u^\tau)^2\right) & D(u^\tau u^x) & D(u^\tau u^y) & 0 \\ D(u^\tau u^x) & D\left((u^x)^2\right) & D(u^x u^y) & 0 \\ D(u^\tau u^y) & D(u^x u^y) & D\left((u^y)^2\right) & 0 \\ 0 & 0 & 0 & 0 \end{pmatrix} \\ & +\frac{1}{3}(\partial\cdot u)\begin{pmatrix} (u^\tau)^2{-}1 & u^\tau u^x & u^\tau u^y & 0 \\ u^\tau u^x & (u^x)^2{+}1 & u^x u^y & 0 \\ u^\tau u^y & u^x u^y & (u^y)^2{+}1 & 0 \\ 0 & 0 & 0 & 1 \end{pmatrix}. \end{aligned} \tag{5.12}$$

Here $D = u^\tau\partial_\tau + u^x\partial_x + u^y\partial_y$ and $\partial\cdot u = \partial_\tau u^\tau + \partial_x u^x + \partial_y u^y + \frac{u^\tau}{\tau}$ [60].

5.7.2 Velocity finding

As shown in [63], since we evolve all three components $\pi^{\tau\tau}$, $\pi^{\tau x}$, and $\pi^{\tau y}$ (one of which is redundant due to the constraint $\pi^{\tau m}u_m = 0$), the flow velocity and energy density can be found from the energy-momentum tensor components with the same efficient one-dimensional zero-search algorithm employed in ideal hydrodynamics. This is important since this step has to be performed after each time step at all spatial grid points in order to evaluate the EOS $p(e)$.

Using the output from the numerical transport algorithm, one defines the two-dimensional vector $\boldsymbol{M} = (M_x, M_y) \equiv (T^{\tau x} - \pi^{\tau x}, T^{\tau y} - \pi^{\tau y})$. This is (up to the substitution $p + \Pi \to p$) the ideal fluid part of the transverse momentum density vector; as such it is parallel to the tranverse flow velocity $\boldsymbol{v}_\perp = (v_x, v_y)$. Introducing further $M_0 \equiv T^{\tau\tau} - \pi^{\tau\tau}$, one can write the energy density as

$$e = M_0 - \boldsymbol{v}_\perp \cdot \boldsymbol{M} = M_0 - v_\perp M, \tag{5.13}$$

where $v_\perp = \sqrt{v_x^2 + v_y^2}$ is the transverse flow speed and $M \equiv \sqrt{M_x^2 + M_y^2}$. One sees that solving for e requires only the magnitude of $\boldsymbol{v}_\perp$ which is obtained by solving the implicit relation [60]

$$v_\perp = \frac{M}{M_0 + p(e = M_0 - v_\perp M) + \Pi}. \tag{5.14}$$

by a one-dimensional zero-search. The flow velocity components are then reconstructed using

$$v_x = v_\perp \frac{M_x}{M}, \qquad v_y = v_\perp \frac{M_y}{M}. \tag{5.15}$$

Note that this requires direct numerical propagation of all three components ($\pi^{\tau\tau}$, $\pi^{\tau x}$ and $\pi^{\tau y}$) since the flow velocity is not known until after the velocity finding step has been completed. Hence the transversality constraint $\pi^{\tau m}u_m = 0$ cannot be used to determine, say, $\pi^{\tau\tau}$ from $\pi^{\tau x}$ and $\pi^{\tau y}$. However, it can be used after the fact to test the numerical accuracy of the transport code.

5.8 Cooper-Frye freezeout using `iS` and particle sampler `iSS`

The name "`iS`" stands for "`iSpectra`"; `iS` is a fast Cooper-Frye particle momentum distribution calculator along the conversion surface. Its output is a continuous function, evaluated at discrete momenta provided by the user, for the invariant momentum distributions of the desired hadron species. The code

"iSS", whose name stands for "iSpectraSampler", goes one step further to generate individual particles samples, using the calculated particle momentum distributions as the relative emission probability. iSS is an "event generator" which generates a complete collision event of emitted hadrons, similar to the events created in the experiment. Both codes are written keeping the following factors in mind:

- **Readability and extendability.** The most important goal is to create a cleanly written framework that calculates particle momentum distributions and performs sampling, whose components and output can be used easily for further physics analyses and tests of new physical ideas. To achieve this, the entire program is divided into modules according to their functionalities, the structures and the algorithms are documented with comments, and long but informative names are chosen for variables and function names.

- **Efficiency.** Both the iS and iSS codes are written aiming for intensive event-by-event calculations where every CPU cycle counts. To achieve the necessary degree of efficiency, much effort is put into optimizing the algorithms at different levels of the calculations.

- **Easy maintainability and re-usability.** The framework is divided into different carefully chosen functionality modules, for better interoperability and to maximize re-usability.

5.8.1 Cooper-Frye freeze-out

The particle emission function that implements sudden decoupling from a surface element $d^3\sigma$ located on a freeze-out hyper-surface $\Sigma(x^\mu)$ is given by the Cooper-Frye formula,

$$E\frac{dN}{d^3p}(x^\mu, p^\mu) = \frac{g}{(2\pi)^3} p^\mu d^3\sigma_\mu \left(f_0(x^\mu, p) + \delta f(x^\mu, p^\mu)\right), \tag{5.16}$$

where g is the spin degeneracy, $d^3\sigma_\mu = (\cosh\eta_s, -\partial\tau/\partial x, -\partial\tau/\partial y, -\sinh\eta_s)\tau dx dy d\eta_s$ is the infinitesimal surface element on $\Sigma(x^\mu)$ for systems with longitudinal boost-invariance, and $f_0(x^\mu, p)$ is local thermal equilibrium distribution function. $\delta f(x^\mu, p^\mu)$ represents the deviation from local thermal equilibrium due to viscous effect and takes the following form,

$$\delta f(x^\mu, p^\mu) = f_0(x^\mu, p)(1 \pm f_0(x^\mu, p))\frac{\pi_{\mu\nu}\hat{p}^\mu\hat{p}^\nu}{2(e+P)}\chi\left(\frac{p\cdot u}{T}\right), \tag{5.17}$$

where $\hat{p}^\mu = p^\mu/(p\cdot u)$ and $\chi(p\cdot u/T) = (p\cdot u/T)^\alpha$ with $1 \le \alpha \le 2$. Integrating the emission function over the freeze-out surface we obtain particle momentum distribution

$$\frac{dN}{dy p_T dp_T d\phi_p} = \int_\Sigma \frac{g}{(2\pi)^3} p^\mu d^3\sigma_\mu (f_0(x^\mu, p) + \delta f(x^\mu, p^\mu)). \tag{5.18}$$

The azimuthally averaged p_T-spectrum is given by,

$$\frac{dN}{2\pi dy p_T dp_T} = \int \frac{d\phi_p}{2\pi} \frac{dN}{dy p_T dp_T d\phi} \tag{5.19}$$

while the anisotropic flow coefficients are computed from,

$$V_n \equiv v_n e^{in\Psi_n} = \frac{\int p_T dp_T d\phi_p e^{in\phi_p} dN/(dy p_T dp_T d\phi_p)}{\int p_T dp_T d\phi_p dN/(dy p_T dp_T d\phi_p)}, \tag{5.20}$$

$$V_n(p_T) \equiv v_n(p_T) e^{in\Psi_n} = \frac{\int d\phi_p e^{in\phi_p} dN/(dy p_T dp_T d\phi_p)}{\int d\phi_p dN/(dy p_T dp_T d\phi_p)}. \tag{5.21}$$

To optimize the efficiency of the numerical calculations, gaussian quadrature points are used for the variables p_T, ϕ_p, and η_s. Further optimization for performing the numerical integral in Eq. (5.18) involves adjusting the order of the integration loops, using local variables, pre-tabulating mathematical functions, etc. The resulting code `iS` is ~ 7 times faster compared to its ancestor `AZSpectra` [6].

5.8.2 Methodology for particle sampling

The particle emission function from the Cooper-Frye formula Eq.(5.16) can be regarded as the probability of emitting particle from a given freeze-out fluid cell with specified momentum. The program `iSS` uses this probability to generate sets of momenta and positions for actual particles emitted at the end of the hydrodynamic simulation. This information is then used as input for the following microscopic hadron cascade simulation. In the sampling procedure, we employ two well-known statistical sampling methods, the inverse cumulative distribution function (CDF) method and the direct probability distribution function (PDF) method, the latter is also known as the acceptance and rejection method [60].

Purely numerical approach

The straightforward (although not necessarily the fastest) approach is to compute all the required quantities numerically.

For a given particle species, the average total number of particles per unit rapidity, dN/dy, is calculated by numerically integrating Eq. (5.16) over all freeze-out fluid cells and all particle transverse momenta $\vec{p}_T$. During the numerical integration, an inverse CDF can be built up with negligible numerical cost for latter efficient sampling. However, in practice, the inverse CDF for a full set of spatial and momentum variables is memory demanding. In order to sample such a multi-dimensional probability distribution function, we divide the random variables into two groups and use efficient specific sampling methods to handle each of them. It is natural to group the spatial information $(\tau, \vec{x}_\perp, \eta_s)$ for the sampled particles into one set of random variables, and their momenta $(p_\perp, \phi_p, y)$ into the other. Dividing the random variables into two groups allows us to perform the sampling in different order and with different methods.

One way to proceed is to first sample the spatial information, $(\tau, \vec{x}_\perp, \eta_s)$, using the inverse CDF method. Along with calculating the particle yield dN/dy, (see above) we build up the inverse CDF for the particle's spatial variables, $(\tau, \vec{x}_\perp, \eta_s)$, by integrating Eq. (5.16) over the transverse momentum, $(p_\perp, \phi_p)$. For a collision event at top RHIC energy, the typical size of the array to store the inverse CDF is about 30,000 freeze-out fluid cells in the transverse plane times 40 points along the η_s direction. Once we have the particles' spatial information, we can evaluate Eq. (5.16) at any given point $(\tau, \vec{x}_\perp, \eta_s)$ for the particle's probability distribution in momentum space. To sample the particle's transverse momentum (p_T, ϕ_p) from this distribution we use the the direct PDF method. In the end, since we assume longitudinal boost-invariance, the particle's rapidity can be sampled uniformly within given rapidity range. By sampling particles in this order, we optimize the sampling of the particle's spatial coordinates since the inverse CDF method has zero rejection rate. The direct PDF method used in momentum space, on the other hand, allows us to use continuous random variables for $p_\perp$ and ϕ_p instead of sampling them at some discrete lattice points. [60]

A second way to proceed is to first sample the particle's momentum information with the inverse CDF method. To this end we first build the inverse CDF for the particle's momentum variables, $(p_\perp, \phi_p)$. Using 15 points in $p_\perp$ and 48 points in ϕ_p. Once we have $(p_\perp, \phi_p)$, Eq.(5.16) is used as a probability distribution for the particle's spatial coordinates $(\tau, \vec{x}_\perp, \eta_s)$ which is then sampled with the direct PDF method.

Semi-analytic approach

In a given collision event the number of particles of species a being emitted from a given fluid cell at x^μ can be calculated analytically as follows:

$$\Delta N_a(\tau_f, \vec{x}_\perp, \eta_s) = \frac{g_a}{(2\pi)^3}\Delta^3\sigma_\mu \int \frac{d^3p}{E} p^\mu (f_0(p) + \delta f(p)). \tag{5.22}$$

Here the surface element of the given fluid cell is $\Delta^3\sigma_\mu = \sigma_\mu \Delta^2 x_\perp \tau \Delta\eta_s$ with $\sigma_\mu = (\cosh\eta_s, -\partial\tau/\partial x, -\partial\tau/\partial y, -\sinh\eta_s)$. The off-equilibrium correction δf originating from the shear stress tensor does not contribute to the total particle yield, due to the properties that $\pi^{\mu\nu}$ is traceless and orthogonal to the flow velocity.

$$\int \frac{d^3p}{E} p^\mu \delta f(p) = \int \frac{d^3p}{E} p^\mu f_0(p)(1 \pm f_0(p)) \frac{\pi_{\alpha\beta}\hat{p}^\alpha \hat{p}^\beta}{2(e+P)} \chi\left(\frac{p}{T}\right) = A u^\mu, \tag{5.23}$$

where $A = u_\mu \int \frac{d^3p}{E} p^\mu \delta f(p) = \frac{\pi_{\alpha\beta}}{2(e+P)} \int \frac{d^3p}{E} (u\cdot p) \frac{p^\alpha p^\beta}{(u\cdot p)^2} \chi(\frac{p}{T}) f_0(p)(1 \pm f_0(p))$. In the local rest frame of the fluid cell, it is easy to see that the integrand is proportional to $\delta^{\alpha\beta}$, hence

$$A = \int d^3p f_0(p)(1 \pm f_0(p)) \frac{p^2}{3E^2} \frac{\pi^\alpha{}_\alpha}{2(e+P)} \chi\left(\frac{p}{T}\right) = 0. \tag{5.24}$$

Thus the particle yield is totally determined by its equilibrium distribution,

$$\begin{aligned} \Delta N_a(\tau_f, \vec{x}_\perp, \eta_s) &= \frac{g_a}{(2\pi)^3} \Delta^3\sigma_\mu \int \frac{d^3p}{E} p^\mu f_0(p) \\ &= \frac{g_a}{(2\pi)^3} \Delta^3\sigma_\mu u^\mu \int p^2 dp\, d\phi\, d\cos\theta \frac{1}{e^{\beta(E-\mu_a)} \pm 1} \\ &= \frac{g_a}{2\pi^2} \Delta^3\sigma_\mu u^\mu \frac{m_a^2}{\beta} \sum_{n=1}^{\infty} \frac{(\mp 1)^{n-1}}{n} e^{n\beta\mu_a} K_2(n\beta m_a). \end{aligned} \tag{5.25}$$

With the assumption of boost invariance, the particle's rapidity y and its space-time rapidity η_s only enters in the combination $y - \eta_s$, and therefore $\frac{dN}{d\eta_s} = \frac{dN}{dy}$. This leads to the following relation:

$$\begin{aligned} \Delta N_a(\tau_f, \vec{x}_\perp, \eta_s) &= \frac{g_a}{(2\pi)^3} \Delta^3\sigma_\mu \int dy \int d^2p_\perp p^\mu f_0(p) \\ &= \frac{g_a}{(2\pi)^3} \int dy \Delta^2 x_\perp \tau \Delta\eta_s \int d^2p_\perp (m_\perp \cosh(y-\eta_s) - \vec{p}_\perp \cdot \vec{\nabla}_\perp \tau) f_0(p) \\ &= \Delta\eta_s \frac{g_a}{(2\pi)^3} \int \tau d\tilde{y} \Delta^2 x_\perp \int d^2p_\perp (m_\perp \cosh(\tilde{y}) - \vec{p}_\perp \cdot \vec{\nabla}_\perp \tau) f_0(p) \end{aligned} \tag{5.26}$$

This integral is independent of η_s, so

$$\Delta N_a(\tau_f, \vec{x}_\perp, \eta_s) = \Delta\eta_s \frac{\Delta N}{\Delta y}(\tau, \vec{x}_\perp). \tag{5.27}$$

In the numerical sampling procedure, we first consider all freeze-out fluid cells $(\tau, \vec{x}_\perp)$ in the transverse plane and use (5.25) (together with (5.27)) to compute the total particle yield per unit rapidity for particle species a, $\Delta N/\Delta y$, for each cell. If freeze-out occurs on a surface of constant inverse temperature β and chemical

potential μ_a, as will be the assumed in the rest of this thesis, Eq. (5.25) can be written as,

$$\Delta N_a(\tau_f, \vec{x}_\perp, \eta_s) = n_a u_\mu(\tau_f, \vec{x}_\perp, \eta_s)\Delta^3\sigma_\mu(\tau_f, \vec{x}_\perp, \eta_s). \tag{5.28}$$

where $n_a = \frac{g_a}{2\pi^2}\frac{m_a^2}{\beta}\sum_{n=1}^{\infty} e^{n\beta\mu_a}K_2(n\beta m_a)$ is the freeze-out density of particle species a, which is the same for all freeze-out cells. In this case, $\Delta N_a/\Delta y$ depends on the position of the fluid cell only through its freeze-out volume,

$$\Delta V(\tau_f, \vec{x}_\perp, \eta_s) = u^\mu\Delta^3\sigma_\mu(\tau_f, \vec{x}_\perp, \eta_s). \tag{5.29}$$

The we use $(\Delta N_a/\Delta y)(\tau_f, \vec{x}_\perp)$ to build up an inverse CDF for the spatial variables $(\tau_f, \vec{x}_\perp)$. Their sum over all $(\tau_f, \vec{x}_\perp)$ points gives the total rapidity density $\frac{dN_a}{dy}$ of particle species a in a given collision event. The constructed inverse CDF is then used to sample the positions $(\tau_f, \vec{x}_\perp)$ of the particles of species a. Finally, we use the Cooper-Frye formula Eq. (5.16) at these sampled positions $(\tau_f, \vec{x}_\perp)$ as the relative probability distribution for sampling the particle's momentum $(p_T, \phi_p, y - \eta_s)$ using the direct PDF method:

$$\begin{aligned} P(p_\perp, \phi_p, y-\eta_s; \tau_f, \vec{x}_\perp) &= \frac{g_i}{(2\pi)^3}\Delta^3\sigma_\mu p^\mu(f_0(p) + \delta f(p)) \\ &= \frac{g_i}{(2\pi)^3}\tau_f\Delta^2 x_\perp \Delta\eta_s(m_\perp\cosh(y-\eta_s) - \vec{p}_\perp\cdot\vec{\nabla}_\perp\tau) \\ &\quad \times(f_0(p) + \delta f(p)). \end{aligned} \tag{5.30}$$

Having obtained $(y - \eta_s)$ by sampling Eq. (5.30), we use boost-invariance and sample y uniformly from a given range specified by the user (e.g., -4 to 4) and then obtain η_s from the previously determined $y - \eta_s$.

Since for every $(\tau, \vec{x}_\perp)$, the probability Eq. (5.30) for $(p_T, \phi_p, y - \eta_s)$ is only sampled once, building an inverse CDF for Eq. (5.30) would be excessively expensive, which is why we choose to use the direct PDF method to sample $(p_\perp, \phi_p, y - \eta_s)$. However, the direct PDF method requires one to estimate the maximum value of the probability distribution function given in Eq. (5.30) which is closely related to the function

$$G(E; A) = \frac{E^A}{e^{\beta(E-\mu)} \pm 1},\ A > 0. \tag{5.31}$$

By setting its derivative to zero, the extrema can be found by solving

$$(1 \mp f_0) = \frac{A}{\beta E} \Longleftrightarrow \begin{cases} xe^x = y;\ x = \beta E - A,\ y = Ae^{\beta\mu - A}, \text{fermions (upper)}, \\ xe^{-x} = y;\ x = A - \beta E,\ y = Ae^{\beta\mu - A}, \text{bosons (lower)}. \end{cases} \tag{5.32}$$

This equation is transcendental and cannot be solved algebraically; however, the solutions to the equations $xe^{\pm x} = y$ in Eq. (5.32) can be pre-calculated and tabulated. For fermions (upper sign), a solution always exists and it is expressed by the Lambert W-function; for bosons (lower sign) the equation has real solutions only when $y < 1/e$, and the it yields two solutions; the physical solution must satisfy $x \in [0, 1]$. In the following, the solution to Eq. (5.32) will be denoted as $E^{\pm}_{\rm max}$ when it exists.

The maximum of $G(E; A)$ with constraint $E \geq m$ will be denoted as $G^{(A)}_{\rm max}$. It depends on several conditions:

1. For fermions (upper sign), $G(E)$ has a single peak at $E^{+}_{\rm max}$ and the constraint maximum is taken as $G(E^{+}_{\rm max})$ if $E^{+}_{\rm max} > m$ and as $G(m)$ otherwise.

2. For bosons (lower sign) with $Ae^{\beta\mu - A} > 1/e$, Eq. (5.32) has no solution and the maximum takes $G(m)$.

3. For bosons (lower sign) with $Ae^{\beta\mu - A} \leq 1/e$, $G(E)$ has two extrema in (μ, ∞), with the larger one being the maximum and given by $E^{-}_{\rm max}$. If $E^{-}_{\rm max} < m$ then the maximum is taken as $G(m)$; otherwise the maximum is taken as the larger one of the two numbers $G(m)$ and $G(E^{-}_{\rm max})$.

In Eq. (5.30), an upper limit for the factor $p^\mu \Delta^3 \sigma_\mu$ can obtained using the Hölder inequality,

$$p^\mu \Delta^3 \sigma_\mu = E\Delta^3\sigma_0 + p^i \Delta\sigma_i \leq (p \cdot u)(|\Delta^3 \sigma_\mu u^\mu| + \sqrt{|\Delta^3\sigma_\mu \Delta^3 \sigma_\nu \Delta^{\mu\nu}|}). \tag{5.33}$$

For the equilibrium contribution, it is clear that the remaining part is to calculate the maximum of the function

$$Ef_0 = \frac{E}{e^{(E-\mu)/T} \pm 1} = G(E; 1); \tag{5.34}$$

the solution to this problem is $G^{(1)}_{\rm max}$.

For the off-equilibrium correction, it is convenient to estimate its maximum in the local rest frame of the fluid cell. We can further rotate the shear stress tensor in the transverse plane such that $\pi^{xy} = 0$. In such a coordinate system

$$\begin{aligned} p^\mu p^\nu \pi_{\mu\nu} &= (p^x)^2 \pi_{xx} + (p^y)^2 \pi_{yy} + (p^z)^2 \pi_{zz} \leq E(|p^x \pi_{xx}| + |p^y \pi_{yy}| + |p^z \pi_{zz}|) \\ &\leq E^2 \sqrt{\pi^2_{xx} + \pi^2_{yy} + \pi^2_{zz}} = E^2 \sqrt{\pi^{\mu\nu}\pi_{\mu\nu}}. \end{aligned} \tag{5.35}$$

In the last step, we rewrote the expression again in Lorentz invariant form such that it is now valid in any frame. With the form of δf in Eq. (5.17) and assuming $f_0 < 1$,

$$E^{\alpha+1} f_0(1 \mp f_0) \leq \lambda E^{\alpha+1} f_0 = \lambda G(E; \alpha+1) \leq \lambda G_{\max}^{(\alpha+1)}, \tag{5.36}$$

where $\lambda = 1$ for fermions and $\lambda = 2$ for bosons. To summarize, the maximum of the PDF Eq. (5.30) for $(p_\perp, \phi_p, y - \eta_s)$ can be estimated as

$$P \leq P_{\max} = \frac{g_a}{(2\pi)^3}\tau \left(|\Delta^3 \sigma_\mu u^\mu| + \sqrt{\Delta^3\sigma_\mu \Delta^3 \sigma_\nu \Delta^{\mu\nu}} \right) \left(G_{\max}^{(1)} + \frac{\sqrt{\pi^{\mu\nu}\pi_{\mu\nu}}}{2(e+P)T^\alpha} \lambda G_{\max}^{(\alpha+1)} \right). \tag{5.37}$$

For light mesons, the validity of the assumption $f_0 < 1$ depends on the value of the freeze-out temperature and chemical potential. Especially, kinetic freeze-out at temperature much below the chemical decoupling temperature can lead to large non-equilibrium chemical potentials that can cause this assumption to break down in some of the fluid cells. We found that $f_0 < 1$ almost all the time, although there were some instances where it was violated. If a more rigorous result is desired, the inequality (5.36) can be replaced by the following one:

$$E^{\alpha+1} f_0(1 + f_0) \quad \leq \quad |E^{\alpha+1} f_0| + |E^\gamma f_0||E^{\alpha+1-\gamma} f_0| \leq G_{\max}^{(\alpha+1)} + G_{\max}^{(\gamma)} G_{\max}^{(\alpha+1-\gamma)}, \tag{5.38}$$

where $0 \leq \gamma \leq \alpha + 1$.

The negative probability issue

For hyper-surface of constant temperature, the Cooper-Frye formula in Eq. (5.16) is not positive semi-definite. This is because on an isothermal hyper-surface Σ, $d^3\sigma_\mu$ can be a space-like vector. So $p^\mu d^3\sigma_\mu$ can be negative in certain regions. Physically, such regions represent parts of the switching surface through which more particles are flying into the fireball instead of being emitted. These negative contributions to the Cooper-Frye integral are essential to ensure the conservation of energy across the hyper-surface. However, they become problematic when one wants to use Eq. (5.16) as a probability distribution (which should always be positive). In the practical sampling procedure, we insert a θ-function by hand to enforce positivity of the probability distribution function. Since we group the random variables differently in the different sampling approaches discussed above, insertion of the θ-function will be done slightly differently in each case, with different consequences. In each case, a slight violation of energy-momentum conservation will occur. Let us therefore explore the implications of the θ-function in some detail, we first sample particle's

spatial information using the purely numerical approach, we use a θ-function $\theta(u^\mu d\sigma_\mu)$ to enforce positivity of the $p_\perp$-integrated distribution function. This means that none of our sampled particles will come from the spatial regions where $u^\mu d\sigma_\mu < 0$. In the second step, when sampling the momenta we enforce the positivity of Eq. (5.16) at the already sampled spatial coordinates. In this step, there are two possible quantities that can become negative. First, $p^\mu \sigma_\mu$ may be negative for some values of p^μ. This represents the situation where a net number of particles with momentum p^μ flies into the fireball. Secondly, in the viscous case, when the off-equilibrium correction δf becomes large, it may overwhelm the equilibrium term and turn the entire distribution function to negative. This situation represents a breakdown of the Chapman-Enskog expansion keeping only terms of first order in δf, Eq. (5.16) should not be trusted in such regions of momentum space. With $\eta/s = 0.20$, we find that this problem usually occurs at high $p_T > 2.5\,\mathrm{GeV}$. In the sampling procedure, we enforce both terms to be always positive, by inserting a product of theta functions, $\theta(f_0 + \delta f)\theta(p^\mu d^3\sigma_\mu)$. $\theta(f_0 + \delta f)$ should be always kept in the calculation, even for the analytic results. The second factor $\theta(p^\mu d\sigma_\mu)$ causes a deviation of the sampled momentum distribution from the analytical result which will be studied below.

If we first sample the particle's momentum information, we enforce positivity of the momentum distribution $dN/(dyp_\perp dp_\perp d\phi_p) \geq 0$. In most cases, the total number of emitted particles with given transverse momentum $\vec{p}_\perp$, integrated over the entire freeze-out surface, is positive. The positivity constraint on $dN/(dyp_T dp_T d\phi_p)$ therefore has almost no effect at all. The set of momentum configurations obtained from this sampling procedure will reproduce momentum distributions and flow coefficients that agree most closely with the analytical Cooper-Frye formalism. In the second step, when we then additionally sample particle's spatial information, we need to enforce positivity of Eq. (5.16) at a given momentum $\vec{p}_\perp$. Regions on the hypersurface where Eq. (5.16) is negative will thus not contribute to particle emission at that $\vec{p}_\perp$. The sampled spatial distribution will therefore show some deviation from the analytic result.

For the semi-analytic approach, the situation is similar to the purely numerical approach when sampling the positions first and the momenta second.

Multiplicity fluctuations at freeze-out

The Cooper-Frye formula only yields the average number of particles emitted from a given hydrodynamic event. Each sampling of the Cooper-Fyre formula will, however, result in a number of emitted particle that fluctuates around that mean value. In principle, these sampling fluctuations are constrained by energy-momentum, baryon number and charge conservation. However, exact implementation of these constraints is non-trivial and will have to be left for future studies.

We use an approximation based on the following procedure: We compute the integer value of the number of particles of species as predicted by Cooper-Frye, sample such particles until that number is exhausted, and then use the non-integer part of the predicted number to uniformly sample for one additional particle. This sampling procedure introduces minimum fluctuations in the total number of particles. In the current version of `iSS`, there are options for users to instead fluctuate the particle number according to Poisson or negative Binomial distributions.

5.9 Concluding Remarks

Using the iEBE-VISHNU framework starts with superMC. As one can see on the framework which is an open-sourced on github site. All the different stage simulators gives different options to get fullfiled and get started. For example the starting routine, superMC gives many options as : Model options , Sub-Model optionss, Glauber optns, Nucleus Optns, Nucleon optns, Collision optns, Monte Carlo optns, P−T spectra optns, Grid optns and some other so that the user predefined how to evolve the system. After the initial condition generator, VISHNew proceeds. It is the $(2+1)$-d viscous hydrodynamic simulation for relativistic heavy-ion collisions. Followed by the particle sampler iSS routine. Here, we have used the outputs from the VISHNew to calculate the electromagnetic fields. The outputs from the Electromagnetic field calculator and pure VISHNew together are fed to the particle sampler, iSS. This is done after finding the velocities outside the framework. The iSS the generates the particle samples wit the full flow information. The additional code written to blend the two outputs explaind above was our duty to write, and we did.

Chapter 6: Result and Discussion

This thesis focused on including the electromagnetic field evolution calculation to the well known iEBE-VISHNU code package for relativistic heavy-ion collisions [60]. We studied the effects from electromagnetic force on the hydrodynamic evolution of the final hadron spectra and their elliptic flow coefficient v_2 using a similar model set up as [102]. We found that electromagnetic force has insignificant effect at the start of the evolution but as the system evolves its effect happens to reduces the elliptic flow at higher transverse momentum, which leads to a bent spectra when compared with no considering the effect. In heavy ion collision the magnetic field is expected to be solenoidal fields from those flying charges. During the beginning of the collision time, the dominant magnetic field is from the spectator and yet the participants of both incoming projectile ions contribute to the evolution of the electric and magnetic field created. Let's see this in more detail in the coming sections.

6.1 The Electromagnetic field evolution

Top left of Fig. 6.1 presents the evolved electric field of Pb-Pb collision with $20-30\%$ centrality and collision energy of $\sqrt{s} = 2.76TeV$ from the hyper surface. As explained in the previous sections the total electric field comes from Coulomb field of the spectators and the plasma it self, the Faraday and also the Lorentz field from the moving charges. The created electric field seen above and below of the reaction axis is quite different which is because of the coulomb electric field created by the positively charged spectator particles at the beginning of the collision. This field created from the spectators is the very reason for the current created in the plasma. The z-direction being the axis of collision, the electric field in its direction is not as wide and broad as that of the other two axises which is a direct evidence of the two projectiles creating fields in opposite direction and the complex multi-directional expansion of the system puts the created fields down as the system evolves. The coulomb force between the particles in the plasma creates an electric field which is against the coulomb electric field. The decreasing of the electric field in the reaction plane inturn drops the magnetic field causing Faraday electric field to evolve. The multidirectionality of the electric force here, contributes to the even flow harmonics than the odd once as discussed below.

One can note that the magnetic field eB reaches the value about $0.4GeV^2$ which joins the manifestation of Chiral Magnetic Effect (CME). And this magnetic field has the ability to affect chirality at the early stage of

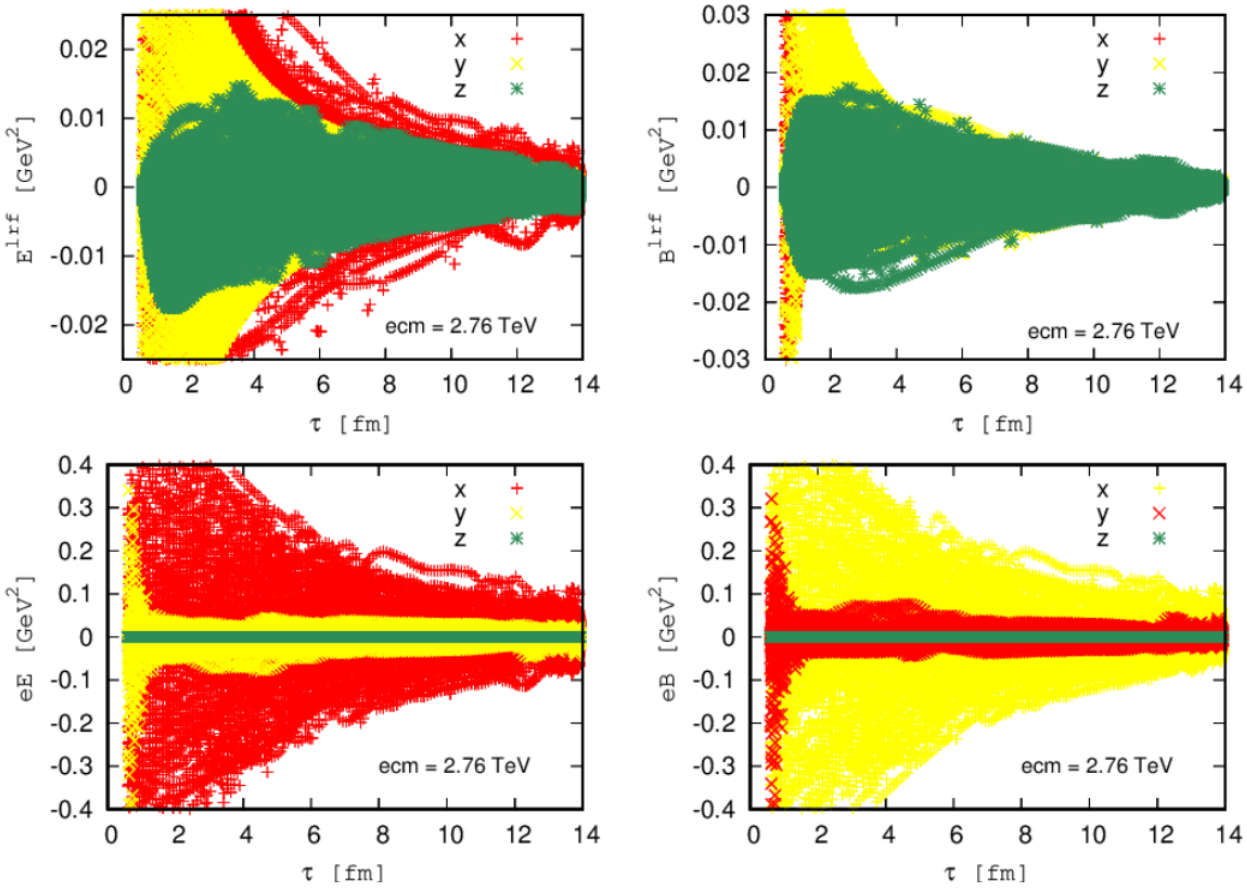

Figure 6.1: Illustration of the evolution of the electromagnetic field evolution created in relativistic heavy-ion collision, (top-left): The three components of the electric field in the local fluid rest frame at points on the freeze-out surface. (top-right) Contributions to the electric field in the local rest frame of a unit cell in the fluid on the freeze-out surface. (bottom-left): The three components of the magnetic field in the local fluid rest frame at points on the freeze-out surface. (top-right): Contributions to the magnetic field in the local rest frame of a unit cell in the fluid on the freeze-out surface.

the QGP evolution. The electromagnetic field created in such relativistic energy is strong enough to create changes for the behavior of every light or heavy particles making it so complex to understand how it gives us information about the QGP.

6.2 Electrical conductivity on electromagnetic field evolution

The electrical conductivity governs how fast the magnetic fields sourced initially. When it is large, the magnetic field in the plasma decays more slowly and this gives a large magnetic field for drifting particles away.

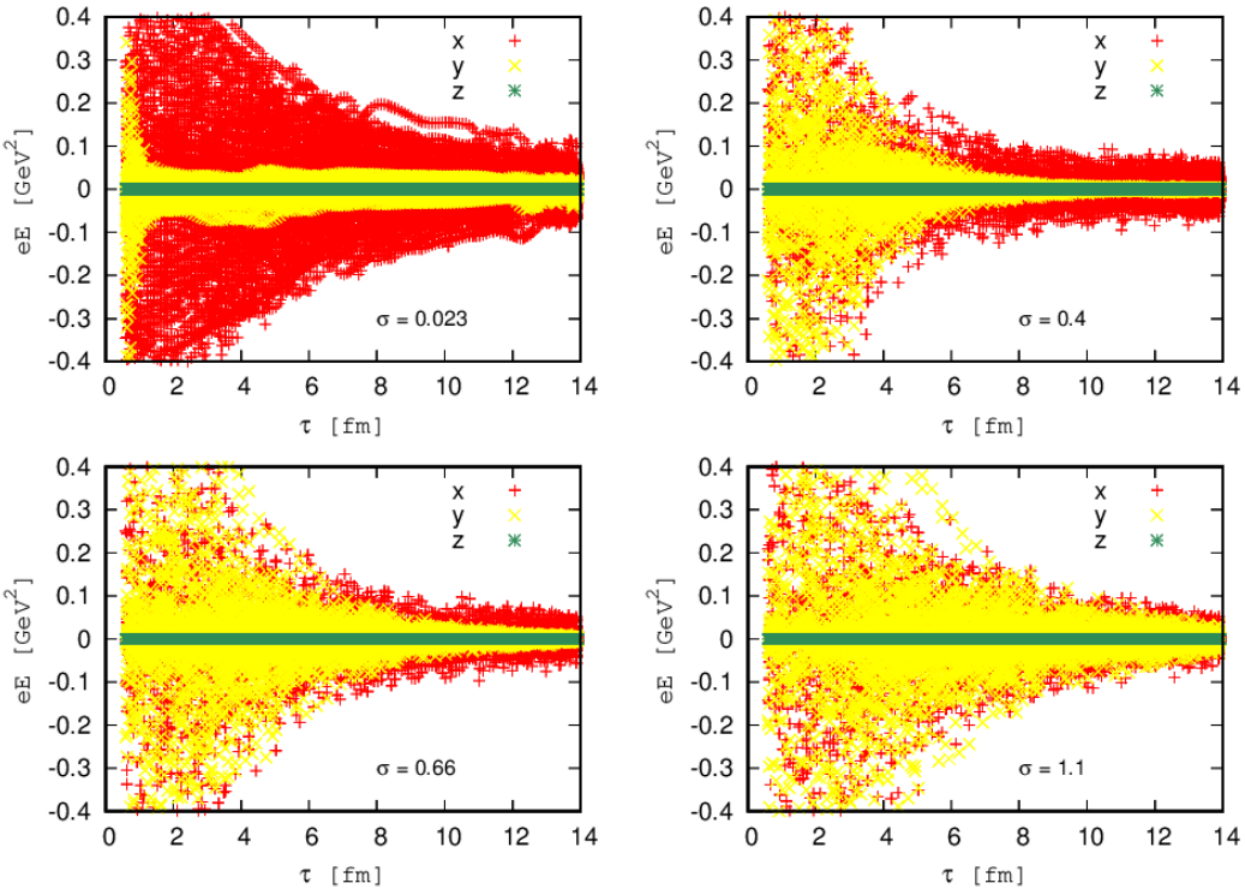

Figure 6.2: Illustration of the dependence of the electric field evolution created in relativistic heavy-ion collision on the electrical conductivity in the Maxwell equations; each are labeled with the corresponding conductivity value (participant contribution ignored).

In practical: since the electrical conductivity is highly sensitive to temperature, a temperature dependent function should have been used. For now as given by Fig. 6.2, our analysis has used four different values of conductivity to see the order of estimate of its effect on the electromagnetic field evolution which potentially can be seen on the flow patterns. At the lower conductivity, It is easy to see that the evolution of the electric field happens to be dominated by the x component of the electric field meaning that the evolved electric field contributes to the side flow rather than vertical and this is due to the coulomb electric field created by the positively charged spectator particles at the beginning of the collision This spectators should have found enough time to evolve before the wounded and the fluid build up the field evolution. As the conductivity increases, the electromagnetic field evolution in both transverse and longitudinal direction become similar. The two components of electric fields are indistinguishable at higher conductivity which is because, the

conductivity suppresses the fields letting them propagate slowly. The maximum rapidity, 1.1, shows totally different evolution from the lowest one which is 0.023. The evolution of electric field is not uniform in x and y direction which can play a great role on the elliptic flow because the electrical conductivity plays a significant role in changing the evolution of the electric and magnetic field as shown in Fig. 6.2.

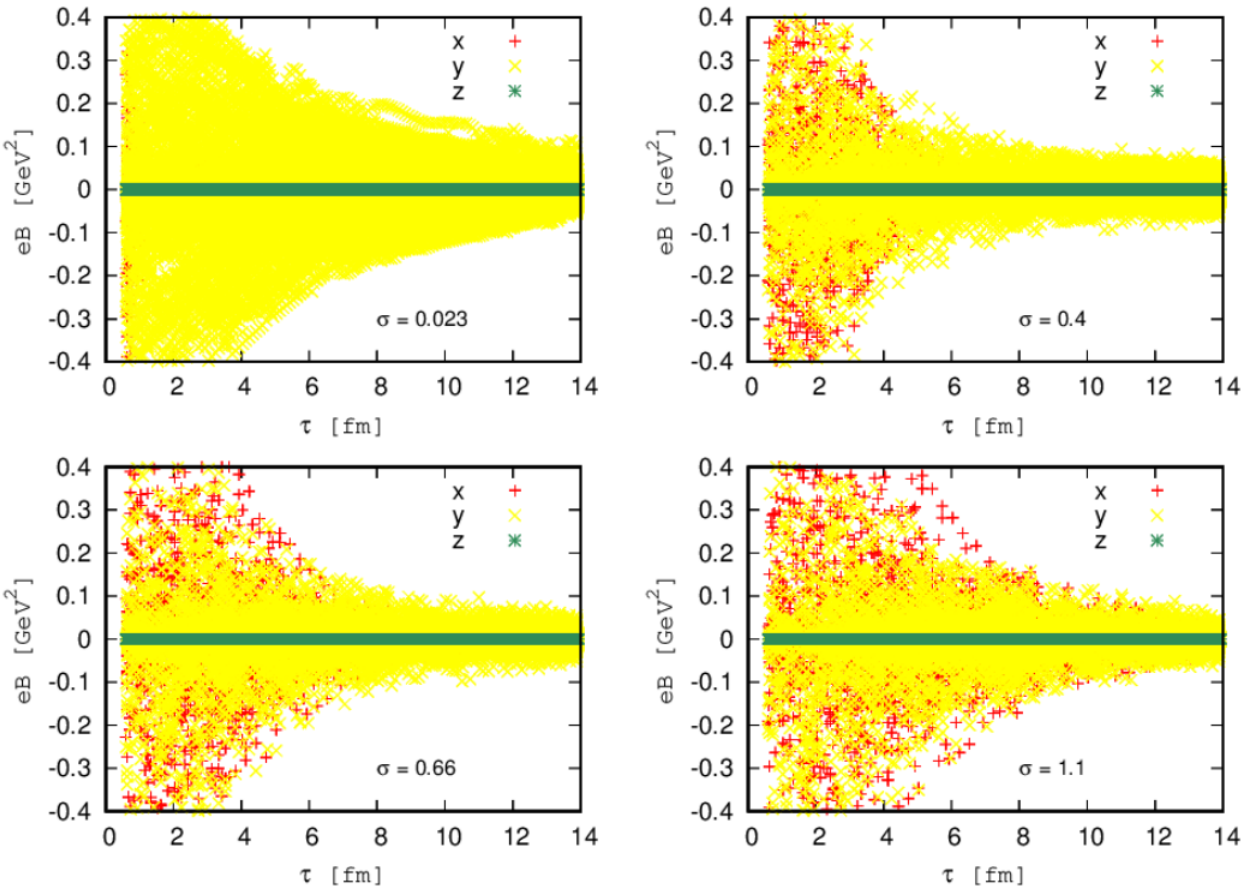

Figure 6.3: Illustration of the dependence of the magnetic field evolution created in relativistic heavy-ion collision on the electrical conductivity in the Maxwell equations; each are labeled with the corresponding conductivity value (participant contribution ignored).

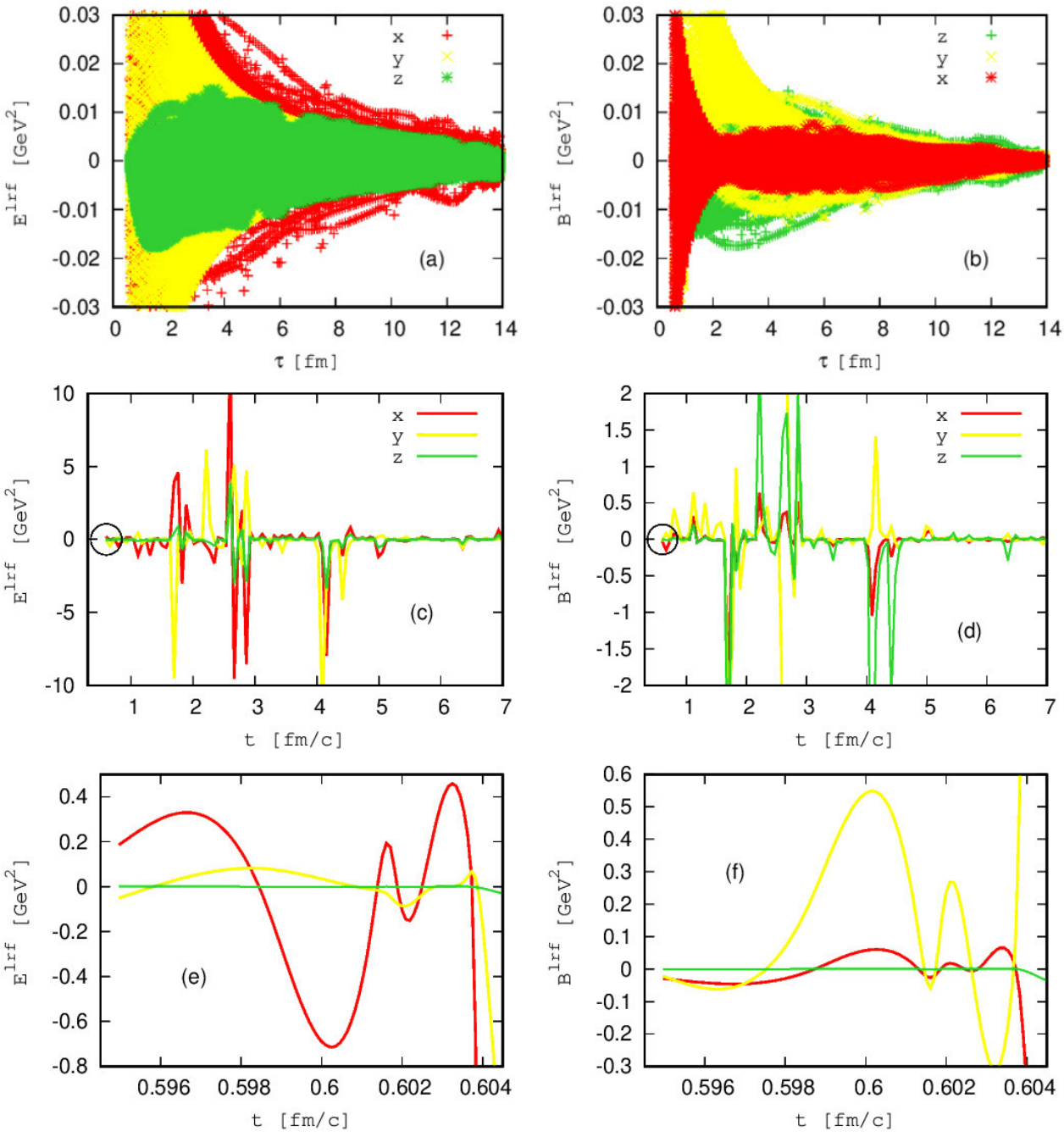

Figure 6.4: (Color online) : (a) and (b) illustrate evolution of the three components of the electric and magnetic fields in the local fluid rest frame at points on the freeze-out surface respectively. (c) through (f) dictate three components of the electric and magnetic fields versus the local time in the fluid rest frame at a fixed space time rapidity of $\eta_s = 0$.

6.3 The Electromagnetic field evolution at fixed rapidity

The first top of Fig.6.4 is an illustration of the evolution of the three components of the electromagnetic field created in relativistic Pb+Pb collision with collision energy of $\sqrt{s} = 2.76$ A TeV. The calculations were made at centrality ranging from 20-30 % (impact parameters in the range 6.24 fm $<$ b $<$ 9.05 fm) and η_s ranging from -7.9 to 7.9. The three components of of the electric fields in the local fluid rest frame at points on the freeze-out surface created are presented in Fig.6.4(a). The created electric field seen above and below of the reaction axis is quite different and this is expected to be due to the coulomb electric field created by the positively charged spectator particles at the beginning of the collision. This field created from the spectators is the reason for the current created in the plasma. The electric field in the z-direction is shown to be smaller than that of the two axes. This is presented 6.4(c). The electric field evolution in the reaction plane increases as the system evolves. It is easy to notice that the transverse (x) and the longitudinal (y) components of the electric field are indistinguishable only at the very early stages of the evolution of the system. Yet, $\vec{E}_y$ and $\vec{B}_y$ has been found to be in same order through out the evolution. As seen on 6.4 (a), the y-component of the electric field varies steeply which dictates the fact that at the very beginning of the evolution a large amount of net charge stays temporally in the almond shaped overlapping region as explained in [133].

We find out that By is not symmetrical and dominated Bx and Bz which can easily be seen from Fig.6.1(b). The sudden pop ups of By seen on Fig.6.4(f) dictates same conclusion. Moreover field components Bx, Ex, and Ey which are as large as By are seen in different time of the system evolution. This can be due to the fluctuations of the positions of charged particles. This in-homogeneous spatial structural distribution of the electromagnetic field has also been studied in [133] where they have utilized the HIJING model to investigate the generation and evolution of the electromagnetic fields in heavy-ion collisions.

Zooming out Fig.6.4(a) we have noticed that, the electric fields perpendicular to the reaction plane shows larger gradiant than the electric fields created parallel to this plane. As explained in [133], depending on how the electrical conductivity is, these outside electric fields can derive positive (negative) charged particles to move outward (toward) the reaction plane, and thus induce an electric quadruple moment which can lead to al elliptic flow imbalance between same particles of different signs; and our result have confirmed this by presenting the elliptic flow variation as given in Fig. 6.10.

To provide more complete information on the early evolution of E and B fields, we show in 6.1 (e) and (f) magnifying the circled region from 6.1 (c) and (d) respectively. As expected E$_x$ is shifted away from zero earlier which dictates the dominance of the field from the positively charged spectator particles

in the beginning of the hydrodynamics. The coulomb force between the particles in the plasma creates an electric field which is against the coulomb electric field. The decreasing of the electric field in the reaction plane inturn drops the magnetic field causing Faraday electric field to evolve. Furthermore as expected, $\mathtt{B}z$ is smaller than $\mathtt{B}x$ and $\mathtt{B}y$.

As explained in the previous sections the total electric field comes from Coulomb field of the spectators plus the plasma, the Faraday and finally the Lorentz field from the moving charges. The fluctuating electric field evolution at a fixed space time rapidity given in Fig. 6.1(c) assures the non-uniformity of the created field. Yet, at a latter time when the spectators have already moved far away from the collision region, the contributions from the residue become important because they move much slower than the spectators. These residue can essentially slow down the decay of the transverse fields in the latter time, as seen from 6.1 and [133].

6.4 The Elliptic flow

6.4.1 Flow Harmonics with and with out the Electromagnetic fields

As explained in the previous sections one of the main job we intended to do beside analyzing the electromagnetic field evolution is to study the contribution of fields on the elliptical flow of identified particles. Table. 6.1 presents how the percentage increase in elliptic flow of the four particles kaon plus, pion plus, pion minus and proton vary. The elliptic flow of proton is suppressed up to an elliptic flow value of nearly 2.37 % of the initial value. At lower momentum they get suppressed down to 1% of its initial value. It is different for pions; at lower momentum the created field raised the flow up to 2.7 %. The effect of the electromagnetic evolution is almost same for the considered particles at higher momentum. As-far-as the system evolution is concerned the flow harmonics values gets suppressed or rouse is non uniform fashion through out the evolution. The percentage increases in elliptic flow of Pion-plus and Pion-minus are exactly the same, dictating how mass plays a dominant role in affecting the bend of flow of particles due to the electromagnetic field evolution.

In Table 6.2 and 6.3 the momentum-dependent flow harmonics coefficients for Neutron and Omega are illustrated. The elliptic flow for the ideal case is compared to the case with the electromagnetic field. The electromagnetic field acts on the evolution of flow that leads to the reduction of elliptic flow of these positively charged particles dominantly. The flow harmonics percentage increase of both neutron and omega increase as the collision energy is raised. At lower momentum both neutron and omega get a percentage increase less than 2% from its initial value. At higher momentum the directed flow is raised up to 6% for neutron and

8% for omega. The created electromagnetic field raised the directed flow in non uniform fashion up to 70 %. Yet, the elliptic flow at 13 A TeV is raised to percentage increase of 10 % which is just 2.7 % at 2.76 A TeV. As-far-as the system evolution is concerned, the flow harmonics values get suppressed or rouse in non uniform fashion through out the evolution. Inorder to explain the effects caused by the electromagnetic evolutions better, every possible contributors like the drag force, electrical conductivity and gluon charge density shall be explained well.

Percentage increase of elliptic flow (ΔV_2) at $\sqrt{s} = 2.76$ A TeV					
No.	Pt (GeV)	Kaon	Pion-Plus	Pion-minus	Proton
1	0.007	0.632501	-2.73601	2.81298	0.990285
2	0.093	-0.628995	2.70434	2.70434	-0.975547
3	0.038	-0.656113	-2.05481	2.09792	-0.984963
4	0.282	-0.884207	1.13557	1.13557	-1.02334
5	0.175	0.67311	0.450833	0.450833	1.19795
6	0.582	0.0102495	0.106331	0.106331	-2.37322
7	0.417	-0.0734528	-0.0689745	-0.0689745	-1.46714
8	0.778	-0.139839	-0.183828	-0.183828	-0.332473
9	1.010	-0.22153	-0.283167	-0.283167	-0.077351
10	1.281	-0.320878	-0.385958	-0.385958	-0.0928342
11	1.598	-0.439648	-0.503512	-0.503512	-0.254785
12	1.971	-0.585524	-0.6487	-0.6487	-0.426537
13	2.416	-0.780726	-0.8473	-0.8473	-0.628866
14	2.964	-1.08911	-1.16826	-1.16826	-0.916958
15	3.694	-1.75244	-1.87066	-1.87066	-1.49467

Table 6.1: The percentage increase of elliptic flow due to the electromagnetic force evolution created in relativistic Pb+Pb collision with collision energy of $\sqrt{s} = 2.76$ A TeV. The change in elliptic flow (ΔV_2) is percentage increase was calculated as the difference between V_2 Theory and V_2 with EM divided by V_2 Theory and the the whole resut was multiplied by 100 percent.

Fig. 6.5 displays off our principal results for the $20 - 30$ % centrality Au+Au at 2.76 TeV. It is a little bit tricky to see how the elliptic flow these four given particles change because of the the electromagnetic field evolution created in the system. plot (a) of Fig. 6.5 shows us how the elliptic flow reacts to the change

Percentage increase of flow harmonics at $\sqrt{s} = 8.16$ A TeV									
No.	Pt (GeV)	Neutron				Omega			
		ΔV_1	ΔV_2	ΔV_3	ΔV_4	ΔV_1	ΔV_2	ΔV_3	ΔV_4
1	0.007	-1.72	-1.01	-0.04	0.0002	-69.3	-1.1	-0.1	0.0001
2	0.093	-1.8	-1.0	-1.5	0.23	-70.5	-1.1	-1.5	0.2
3	0.038	-1.8	-1.0	-1.9	-1.33	-69.5	-1.1	-1.8	-0.8
4	0.282	-1.8	-1.04	-1.9	-1.05	-66.3	-1.2	-1.9	-0.6
5	0.175	-1.9	-1.17	-1.95	-0.9	-61.0	-1.6	-1.9	-0.35
6	0.582	-2.1	-2.2	-2.1	-0.5	-56.0	10.3	-2.2	0.3
7	0.417	-2.3	1.3	-2.45	0.3	-58.7	0.4	-2.9	8.2
8	0.778	-2.5	0.26	-3.8	-11.4	-159	0.1	-6.9	-2.2
9	1.010	-3.32	0.04	-182.0	-1.9	23.6	-0.06	3.5	-1.3
10	1.281	-3.25	-0.1	1.3	-1.2	2.9	-0.2	0.16	-0.99
11	1.598	-3.0	-0.3	-0.4	-0.9	-0.3	-0.3	-0.8	-0.8
12	1.971	0.27	-0.4	-1.2	-0.6	-21.9	-0.5	-1.5	-0.5
13	2.416	-4.3	-0.63	-2.0	-0.3	-2.9	-0.7	-2.3	-0.14
14	2.964	-1.2	-0.9	-3.0	0.24	0.2	-1.0	-3.3	0.4
15	3.694	5.9	-1.5	-4.85	1.2	7.9	-1.6	-5.2	1.4

Table 6.2: The percentage increase of flow harmonics due to the electromagnetic force evolution created in relativistic Pb+Pb collision with collision energy of $\sqrt{s} = 8.16$ A TeV. The change in elliptic flow (ΔV_2) is percentage increase was calculated as the difference between V_2 Theory and V_2 with EM divided by V_2 Theory and the the whole resut was multiplied by 100 percent.

in the transverse momentum at different rapidity. Plot (b) of Fig. 6.5 shows us how the elliptic flow changes at a fixed rapidity where on every point on the plot the rapidity is different.

One can see that the elliptic flow of the four particles is not that much affected if we consider the transverse momentum alone, which implies that space and time matters. At a given momentum particles might have similar flow coefficient but transversing at different rapidity. But the momentum it self is not electromagnetic field proof, it also get affected because of the electromagnetic field created. On Fig. 6.5, if one sets the momentum be fixed, the flow coefficient changes and vice versa. The electromagnetic field evolution stamp down the flow of the particles yet the elliptic flow was roused to a higher elliptic flow coefficient at lower momentum.

It is quiet open to as to what level the elliptic flow is affected for different particles. As one can see from Fig. 6.6 the change in elliptic flow of the four particles proton, pion plus, kaon plus and anti proton is quit different yet very clear to notice the magnitude difference. Protons have larger electromagnetically induce shift in their mean P_T compared to that of pions and kaons. The elliptic flow of protons was raised and supprressed to a recognizable percentage at lower momentum. It is different for pions; at lower momentum it

Percentage increase of flow harmonics at $\sqrt{s} = 13$ A TeV									
No.	Pt (GeV)	Neutron				Omega			
		ΔV_1	ΔV_2	ΔV_3	ΔV_4	ΔV_1	ΔV_2	ΔV_3	ΔV_4
1	0.007	-1.71	-1.01	-0.04	0.00025	-69.3	-1.1	-0.06	0.0001
2	0.093	-1.75	-1.00	-1.48	0.23	-70.5	-1.1	-1.5	0.18
3	0.038	-1.78	-1.01	-1.87	-1.33	-69.5	-1.1	-1.8	-0.9
4	0.282	-1.83	-1.04	-1.91	-1.1	-66.3	-1.2	-1.9	-0.59
5	0.175	-1.93	-1.17	-1.95	-0.88	-61.0	-1.6	-1.97	-0.35
6	0.582	-2.1	-2.2	-2.1	-0.5	-56.0628	10.3	-2.2	0.26
7	0.417	-2.3	1.3	-2.45	0.3	-58.7	0.4	-2.9	8.2
8	0.778	-2.5	0.26	-3.76	-11.4	-159.0	0.092	-6.9	-2.2
9	1.010	-3.3	0.04	-1.9	-1.9	23.6	-0.059	3.5	-1.33
10	1.281	-3.2	-0.1	1.3	-1.24	2.95	-0.19	0.16	-0.99
11	1.598	-3	-0.3	-0.4	-0.9	-0.307	-0.33	-0.8	-0.75
12	1.971	0.3	-0.45	-1.2	-0.6	-21.9	-0.49	-1.5	-0.49
13	2.416	-4.3	-0.6	-2.0	-0.3	-2.87	-0.68	-2.27	-0.14
14	2.964	-1.2	-0.9	-3.0	0.2	0.22	-0.98	-3.28	0.4
15	3.694	5.9	-1.5	-4.8	1.2	7.95	-1.59	-5.18	1.37

Table 6.3: The percentage increase of flow harmonics due to the electromagnetic force evolution created in relativistic Pb+Pb collision with collision energy of $\sqrt{s} = 13$ A TeV. The change in elliptic flow (ΔV_2) is percentage increase was calculated as the difference between V_2 Theory and V_2 with EM divided by V_2 Theory and the the whole resut was multiplied by 100 percent.

suppress the flow up to 3%. The effect of the electromagnetic evolution looks almost same for the considered particles at higher momentum. The values by what the elliptic flow gets suppressed or rouse is not uniform as expected, it changes through out the evolution. As far as the electromagnetic evolution is affected by the drag force, electrical conductivity and gluon charge density, the functionality of every variables should come to the table. Why the shift induced by the field is larger for protons than pions can be answered with a single word, mass. At a given transverse momentum their speed will not be the same. Hence, the slower the particle is the higher it gets exposed to the field and they happen to be protons than pions. Yet this difference can no be avoided with this reason only; a detailed analysis of the gluon field distribution, the temperature effect, and many possible other functions has to be studied well. It is like saying a detailed Magnetohydrodynamics calculation is awaiting ahead.

6.4.2 Other Flows

As one can see from Fig. 6.10, the electromagnetic field effect on Δv_1 is small in magnitude. This can lead us to ask that: how in the world those electric fields the coulomb, Faraday, Lorentz, and whatever the

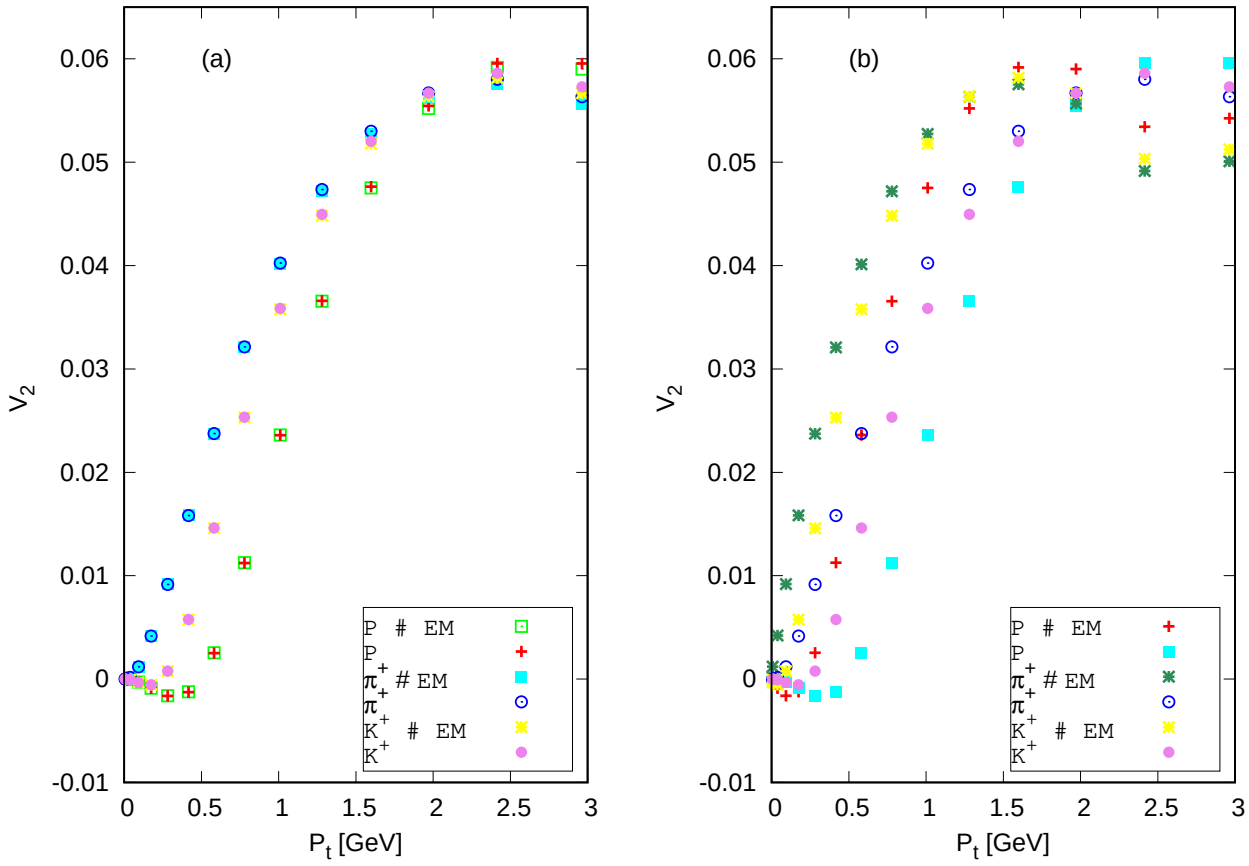

Figure 6.5: The Elliptic with and with out the electromagnetic effect

field from the plasma contributes to the flow of particles radially ? The answer would rather be simple; they cancel out each other and get extremely low so that the field in the dilute system manages to be dominant multi−directionality. Because of this the contribution to the odd harmonics fall to be very small and a significant contribution to the even harmonics is clearly seen. From these one can come up to the decision that, the sidway electric fields created by the Faraday and Coulomb has almost canceled the electric Lorentz field created in the fluid system. Still there is a very small contribution to the radial flow and this has to be from the collision axis.

6.4.3 Other Identified Particles

As we have discussed above the flow harmonics of particles is influenced by the electromagnetic field evolution. Here let′s see how other particles are influenced too. Reminding as each points on the plot of Fig. 6.8 represents different rapidity, one can notice as the elliptic flows of heavier elementary particles are influenced by the fluid evolution. The plot dictates that the change in directed flow is so small that even

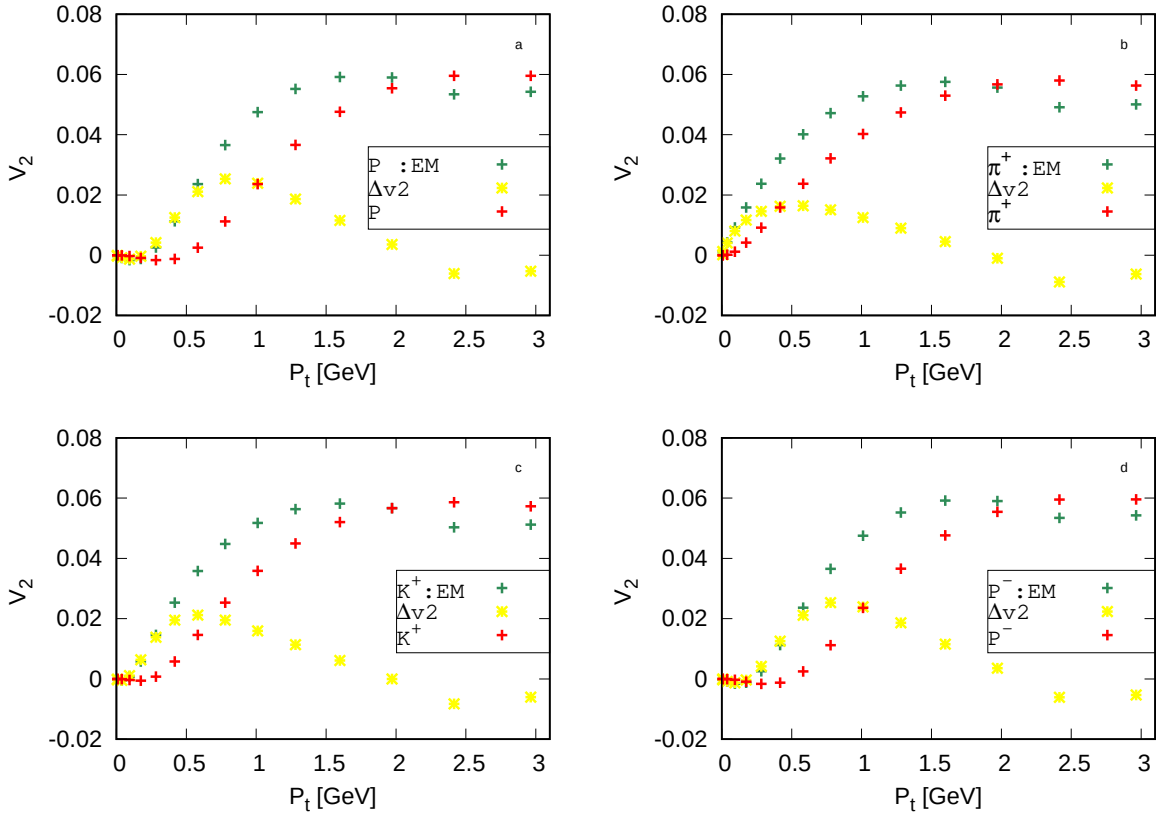

Figure 6.6: The change in elliptic flow of pions, kaons, protons and anti−protons from the electromagnetic effect created during nuclear collision between Au−Au at 2.76 TeV

one can say, the side push from the field is almost insignificant. even in these very small changes proton, neutron and kaons get pushed aside with higher magnitude than that of pions. This tells us that, the heavier the particle is the higher side pushes it gets. To thecontrary of the results from [102], we have found that the electromagnetic field evolution does not depend much on the type of charge the particles has as it is expected; it rather looks how heavy that particle is. This ic clearly seen on the plot (a), (b), (d) and Fig. 6.9 that a particle and its anti particle gets a side push from the electromagnetic field evolution with very close magnitudes. In the force balance calculation, we found the drift velocity for particles with charge 1, -1, 2 and -2 as in [102]. This is like saying we have calculated the drift−velocity of these charges on a given fluid cell. Diversifying the vast charge consideration will await us for future exploration of the field influence on any particle found anywhere.

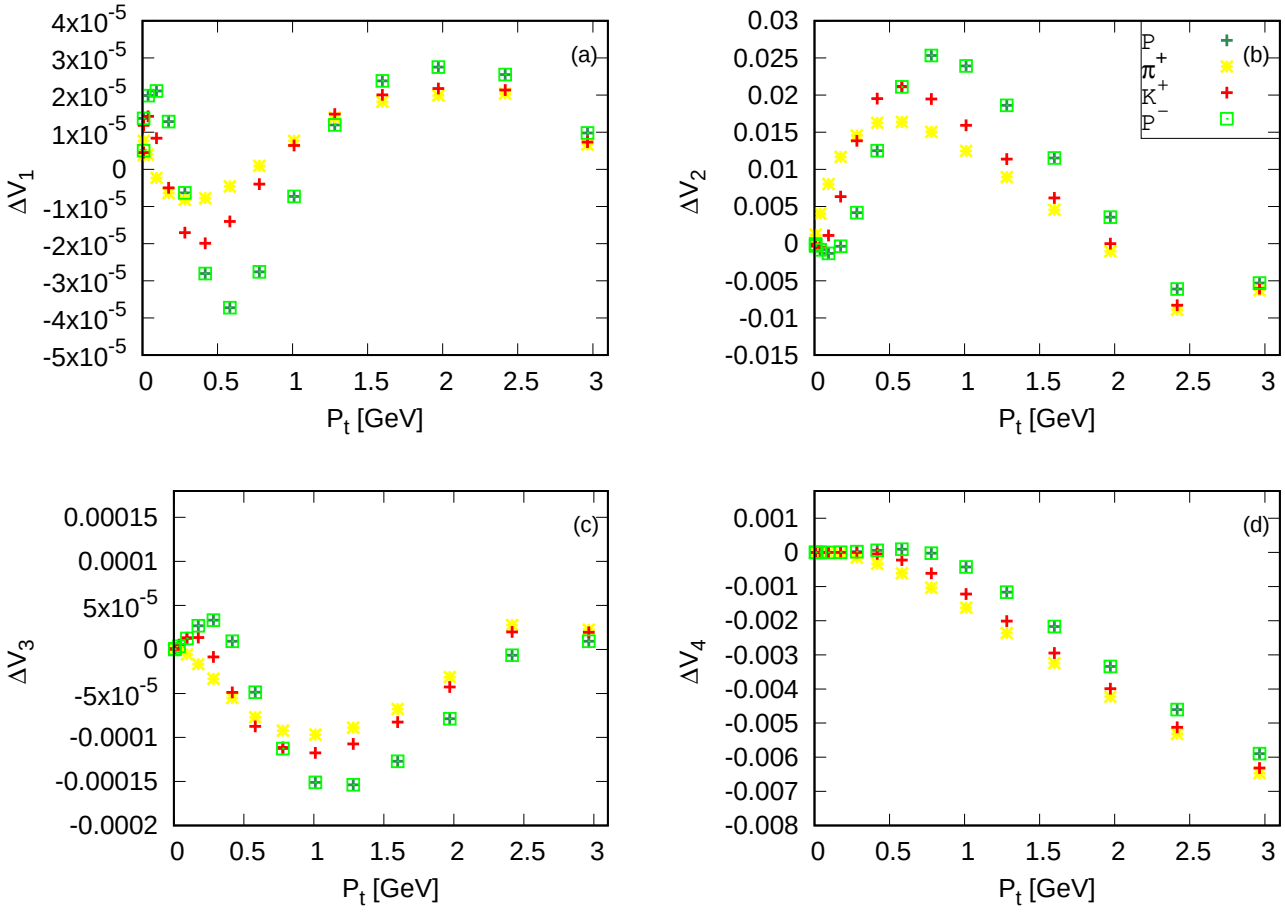

Figure 6.7: The effect of electromagnetic force on radial, elliptical, triangular and rectangular flows. The value of elliptic flow is much higher than all the other three harmonics coefficients. Elliptic flow is higher than radial, triangular and rectangular flow in the order of $10^3, 10^2$, and 10 respectively. It is like approximately saying, V_2 is 1000 times higher than V_1 and 100 times higher than v_3 and 10 times that of v_4. The contribution of electromagnetic field created in the system is dominant on the elliptic flow.

Fig. 6.9 dictates that particle λ and Ξ gets larger directed flow change and this tells us that lambda and xi gets a better kick off than even proton; same as found in Ref. [132]. This tells us once again the dependence of field effect on the mass of created particles reminding as both contains strange and/charm quarks.

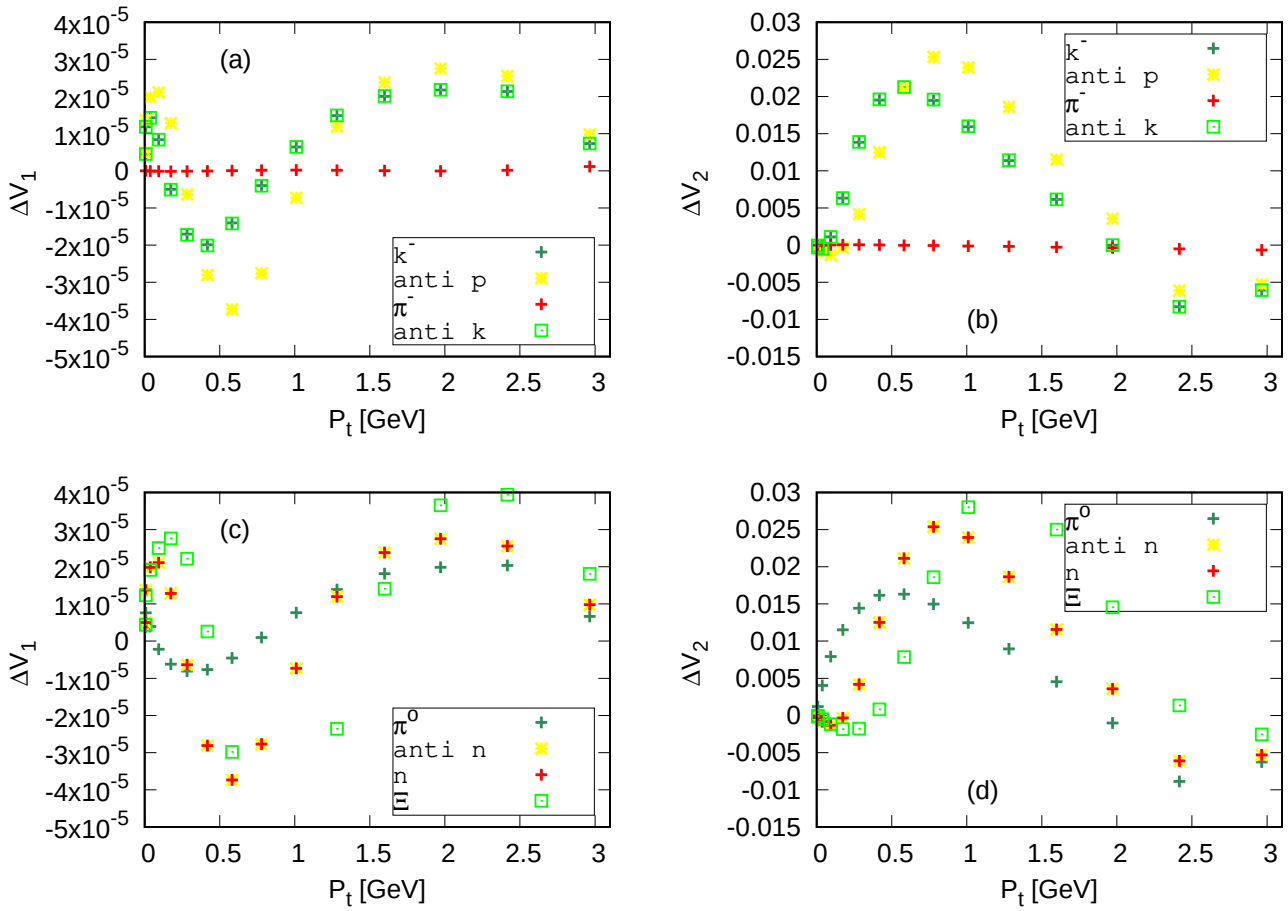

Figure 6.8: Illustration of the change in radial and elliptic flow of particles relative to other particles

6.4.4 Comparison

As one can see from Fig. 6.10, the electromagnetic field effect on Δv_2 and Δv_3 is small in magnitude for the positively charged and lighter particles. The change on the odd flow harmonics and the even ones is not quiet same. The even flow harmonics get suppressed or lower in higher magnitude than the odd ones. The directed flow specially get influenced insignificantly which should be due to the side-way electric fields created by the Faraday and Coulomb has been being almost canceled the electric Lorentz field created in the fluid system. Still there is a very small contribution to the directed flow and this has to be from the collision axis. Meanwhile as presented in Fig. 6.10 (c) and (d), the triangular flow change is in the order of 10^{-4} for neutron, xsi, antiproton, lambda and anti kaon. The elliptic flow change for proton, kaon and pion happened to be in the order of 10^{-6}. From these two triangular flow changes we can see how small the specialized side pushes are. Yet from Fig. 6.10 (a), it is easily seen as the elliptic flow of neutron, xsi, antiproton, lambda and anti kaon is significantly influenced by the created electromagnetic evolution. This leads us to notice

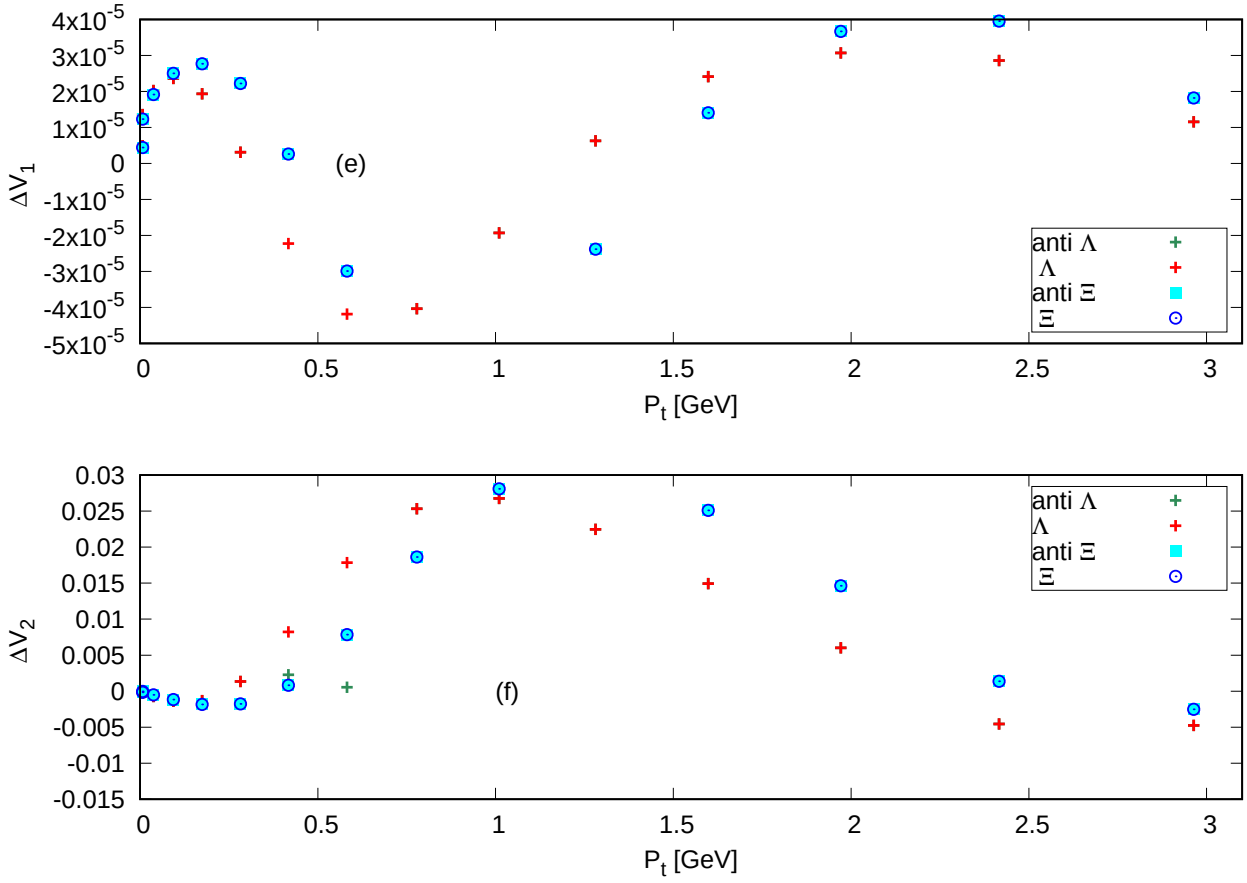

Figure 6.9: Illustration of of the change in radial and elliptic flow of particles and their anti−particles

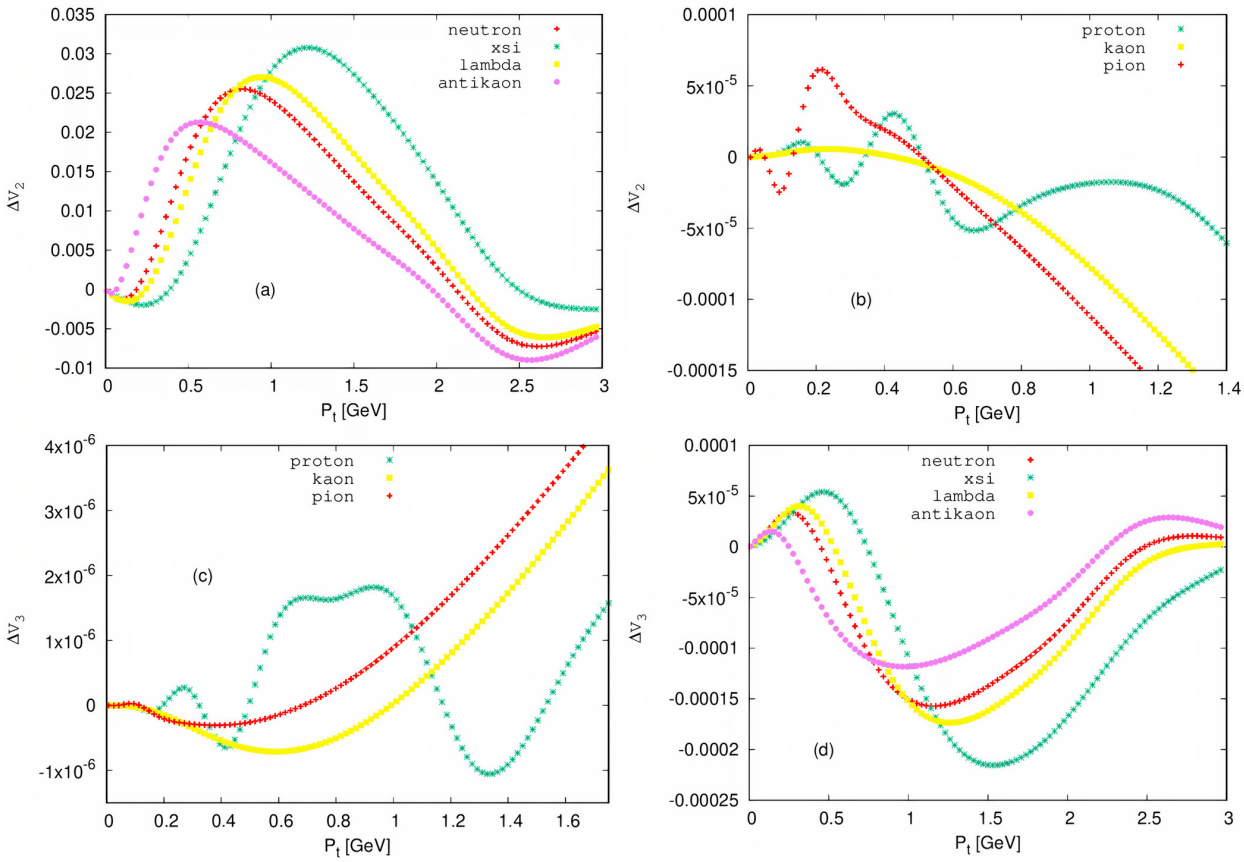

Figure 6.10: (Color online) The effect of electromagnetic force on the change in directed flow ΔV_1, change in elliptic flow ΔV_2, change in triangular flow ΔV_3 and change in rectangular flow ΔV_4 for some identified particles. The change in even flow harmonics coefficients is higher than that of the odds.

how the multi-directional side push of the created heavier particles is significantly influenced by the fields of electromagnetic evolution. The heavier a particle, the higher side pushes it gets. The particles Lambda and Xsi getting larger odd flow harmonics changes than proton, same as found in Ref. [132], tells us once again the dependence of field effect on the mass of created particles.

A hand full of other groups have studied the effect of electromagnetic field evolution on the flow of particles in relativistic heavy ion collision. They all have used different approaches making some crude assumptions to tackle the problem as we just did. Our model set−up is same as that given in [102]. All the studies [102, 112, 130, 131] came up to similar understanding as the electromagnetic evolution has an effect on the bending of particles flow. Yet they all simplify their assumptions to make calculations easier as we did. We calculated the drift velocity of particles with charges ranging from $-2/3$ to 2. our result of heavier particles getting better initial push agrees with [130]. Odd to that of the results in most of the papers listed above, our result shows that the electromagnetic effect on flow harmonics of particles depends on mass rather than charges. To much of our surprise the suppression of the field at higher momentum, even though it looks small, gives us to work an event by event simulation of this work freeing some series assumptions we make; like the conductivity not depending on temperature, not thinking of the gluon field fluctuating nature, the drag force coefficient and many others assumptions too.

Chapter 7: Conclusion and Outlooks

Calculating the magnitude of the evolution of both the electric field and magnetic field in relativistic heavy ion collision, analyzing its effect on the flow of particles identified and pointing out some other related dependences were the main goals of this thesis. We have used the iEBE-VISHNU frame work to describe the full relativistic viscous hydrodynamics of the heavy ion collision considered. The work includes writing a code to calculate the magnitude of electric and magnetic fields created in the system from the well known Maxwell′s equations plus find out the drift velocities caused by these fields. After having the field magnitude, we were expected to inject these velocity vectors to the fame work and deduce what contributions the field has on the evolution of particles created. After analyzing the results from the field evolution and the hydro calculation, we have made the following conclusions.

The peak value of the magnetic field created by the charges reach up to 0.4 GeV. These non uniform fluctuating fields created at the early stage are created dominantly by the spectators. The evolution of the field is not uniform and is different from left and right side of the collision axis. Since the created system has its own electrical conductivity level, it makes it complex for the field to propagate through. As the electrical conductivity increases, the electromagnetic field distribution in the x and y becomes fair, but not in the reaction axis.

Both the transverse momentum and flow of particles are influenced by the electromagnetic field evolution. The effect is not uniform for all particles. The Electromagnetic field created stamp down the flow of particles at higher momentum and rouse the flow at lower transverse momentum or just at mid rapidity. Protons being massive than pions, have got affected by the field in the early evolution time. The lighter particles fly off the region before getting pushed by the fields.

The Electromagnetic field created is found to stamp down and rouse the flow of particles at different transversal momentum in non uniform fashion. We found out that heavier particles like lambda and xsi get the higher flow harmonics increase. The different radial electric forces cancel out each other causing directed flow not to be that affected as elliptic flow. Mass is the dominant factor than charges which is observed as particles and their anti-particles get washed aside by the field in similar fashion. The lighter particles get slight flow harmonics increase and they should have flown off the region before getting pushed by the fields. Yet at collision energy of $\sqrt{s} = 2.76$ ATeV, maximum of $\pm$ 2.7 % increase in elliptic flow is observed.

The elliptic flow of protons was raised up to an elliptic flow percentage increase of 2.37 % from the initial value. At lower momentum, the elliptic flow of proton gets suppressed down to 1.5% of its initial value. For pions, the flow was raised by 2.7 %. At higher momentum the effect of electromagnetic on the change in elliptic flow was found very close. As-far-as the system evolution is concerned the flow harmonics values gets suppressed or rouse is non uniform fashion through out the evolution. Inorder better explain the effects caused by the electromagnetic evolution, every possible contributors to the change in elliptic flow should be included in functional form.

The elliptic flow coefficient is increased up to 10 % of its value due to the electromagnetic field evolution at collision energy of 8.16 ATeV, and it is also affected to the order of a thousand than the radial flow and this happens because of the cancellation of the electric fields in the x and y direction having a slight field in the reaction axis which causes the very small radial flow change observed. The triangular flow is also not that affected by the field, it is lower than the elliptic flow by the order of $100s$. When we come to the rectangular flow, it is lower only to the order of tens with the elliptic flow. This shows that, the electromagnetic field evolution affects the even flow harmonics with greater magnitude than the odd ones.

From analyzing the flow harmonics change of different evolution of particles, it is clear that Lambda and Xsi get larger directed flow change than the other particles like Pions, Kaons, and even Proton. Lambda and Xsi's being made of with strange and (or) charm quarks as their building blocks play a role to let them be heavier and waits the field until it pushes them aside. Particles and their antiparticles getting crudely same flow harmonics change because of the fields created says: mass is the dominant factor than charges and these particles and their anti−particles just get washed aside by the field.

In short, this field of relativistic heavy ion collision hasn$'$t seen its end yet and we believe it will keep developing well with the collaborations among several different groups all over the world digging every hole to understand everything about the QGP will keep getting better. What this thesis has covered is just part of polishing the gateway for a story that has just began.

BIBLIOGRAPHY

[1] Tewodros Gezhagn and A. K. Chaubey, Elliptic Flow of Particles under the Influence of Electromagnetic Field Evolution in Relativistic Heavy Ion Collision, *Sch J Phys Math Stat.***DOI: 10.36347/sjpms.2021.v08i02.002** (2021).

[2] U. W. Heinz, Towards the Little Bang Standard Model, *J. Phys. Conf. Ser.***455** (2013).

[3] B. Muller, J. Schukraft and B. Wyslouch, First Results from Pb+Pb Collisions at the LHC *Ann. Rev. Nucl. Part. Sci. 62*,**361**(2012).

[4] J.-Y. Ollitrault, "Anisotropy as a signature of transverse collective flow," *Phys. Rev.* **D46** (1992) 229–245.

[5] W. Reisdorf and H. G. Ritter, "Collective flow in heavy-ion collisions," *Ann. Rev. Nucl. Part. Sci.* **47** (1997) 663–709.

[6] P. F. Kolb and U. Heinz, "Hydrodynamic description of ultrarelativistic heavy ion collisions," *in* Quark-Gluon Plasma 3*, edited by R. C. Hwa and X.-N. Wang (World Scientific, Singapore)* (2003) 634, nucl-th/0305084.

[7] P. Huovinen, "Hydrodynamical description of collective flow," *in* Quark-Gluon Plasma 3*, edited by R. C. Hwa and X.-N. Wang (World Scientific, Singapore)* (2003) 600, nucl-th/0305064.

[8] J. Rafelski and B. Muller, "Strangeness production in the quark - gluon plasma," *Phys. Rev. Lett.* **48** (1982) 1066.

[9] J. Sollfrank and U. W. Heinz, "The role of strangeness in ultrarelativistic nuclear collisions," nucl-th/9505004.

[10] T. Matsui and H. Satz, "J/ψ suppression by quark-gluon plasma formation," *Phys. Lett.* **B178** (1986) 416.

[11] L. Kluberg and H. Satz, "Color deconfinement and charmonium production," 0901.3831.

[12] L. D. McLerran and T. Toimela, "Photon and dilepton emission from the quark - gluon plasma: some general considerations," *Phys. Rev.* **D31** (1985) 545.

[13] C. Gale and K. L. Haglin, "Electromagnetic radiation from relativistic nuclear collisions," hep-ph/0306098.

[14] X.-N. Wang and M. Gyulassy, "Gluon shadowing and jet quenching in A + A collisions at $\sqrt{s} = 200$ GeV," *Phys. Rev. Lett.* **68** (1992) 1480–1483.

[15] X.-N. Wang, Z. Huang, and I. Sarcevic, "Jet quenching in the opposite direction of a tagged photon in high-energy heavy-ion collisions," *Phys. Rev. Lett.* **77** (1996) 231–234, hep-ph/9605213.

[16] M. Gyulassy, I. Vitev, X.-N. Wang, and B.-W. Zhang, "Jet quenching and radiative energy loss in dense nuclear matter," nucl-th/0302077.

[17] A. Kovner and U. A. Wiedemann, "Gluon radiation and parton energy loss," hep-ph/0304151.

[18] S. Jeon and V. Koch, "Event-by-event fluctuations," hep-ph/0304012.

[19] U. W. Heinz and M. Jacob, "Evidence for a new state of matter: An assessment of the results from the CERN lead beam programme," nucl-th/0002042.

[20] "The frontiers of nuclear science, a long range plan," 0809.3137.

[21] P. Jacobs *et al.*, "Phases of QCD: Summary of the Rutgers long range plan town meeting," 0705.1930.

[22] "RHIC scientists serve up perfect liquid," http://www.bnl.gov/rhic/milestones.htm.

[23] C. Shen, "The standard model for relativistic heavy-ion collisions and electromagnetic tomography," .

[24] H. Song and U. Heinz, Suppression of elliptic flow in a minimally viscous quark- gluon plasma, Phys. Lett. B 658. arxiv.org/pdf/0709.0742, doi:10.1016/j.physletb.2007.11.019.

[25] H. Song, S. Bass, U. Heinz, T. Hirano, and C. Shen, 200 A GeV Au+Au, collisions serve a nearly perfect quark-gluon liquid, Phys.Rev.Lett. 106 (2011) 192301, arxiv.org/pdf/1011.2783, 10.1103/physrevlett.106.192301.

[26] M. Luzum, Elliptic flow at energies available at the CERN Large Hadron Collider: Comparing heavy-ion data to viscous hydrodynamic predictions, Phys.Rev. C83 (2011) 044911, arxiv.org/pdf/1011.5173, 10.1103/PhysRevC.83.044911.

[27] L. Csernai, Introduction to relativistic heavy ion collisions,

[28] T. D. Lee and G. C. Wick, "Vacuum stability and vacuum excitation in a spin 0 field theory," *Phys. Rev.* **D9** (1974) 2291.

[29] J. C. Collins and M. J. Perry, "Superdense matter: neutrons or asymptotically free quarks?," *Phys. Rev. Lett.* **34** (1975) 1353.

[30] H. G. Baumgardt *et al.*, "Shock waves and Mach cones in fast nucleus-nucleus Collisions," *Z. Phys.* **A273** (1975) 359–371.

[31] C. Wong, "Introduction to high energy heavy-ion collisions," *World Scientifc* (1994).

[32] V. Hove, C. Prudent, Theoretical prediction of a new state of matter, the "quark-gluon plasma" (also called "quark matter"), Phys.Rev. C83 (2011) 044911, cds.cern.ch/record/183417, 10.1103/PhysRevC.83.044911.

[33] F. Karsch,"The phase transition to the quark gluon plasma: Recent results from lattice calculations", Nuclear Physics A.590. 9503010, 10.1016/0375-9474(95)00248-Y.

[34] A. Bazavov *et al.*, "Equation of state and QCD transition at finite temperature," 0903.4379.

[35] M. Cheng *et al.*, "The QCD equation of state with almost physical quark masses," *Phys. Rev.* **D77** (2008) 014511, 0710.0354.

[36] U. W. Heinz and P. F. Kolb, "Early thermalization at RHIC," *Nucl. Phys.* **A702** (2002) 269–280, hep-ph/0111075.

[37] M. Gyulassy, "The QGP discovered at RHIC," nucl-th/0403032.

[38] M. Gyulassy and L. McLerran, "New forms of QCD matter discovered at RHIC," *Nucl. Phys.* **A750** (2005) 30–63, nucl-th/0405013.

[39] E. V. Shuryak, "What RHIC experiments and theory tell us about properties of quark-gluon plasma?," *Nucl. Phys.* **A750** (2005) 64–83, hep-ph/0405066.

[40] U. W. Heinz, M. Jacob, Evidence for a New State of Matter: An Assessment of the Results from the CERN Lead Beam Programme, arXiv:abs/nucl-th/0002042.

[41] V. Barbara, Jacak1, and B. MÃ¼ller, The Exploration of Hot Nuclear Matter, American Association for the Advancement of Science 337, Issue 6092, pp. 310-314 10.1126/science.1215901.

[42] E. Shuryak, Prog.Part.Nucl.Phys. **53**, 273 (2004), hep-ph/0312227.

[43] P. Kovtun, D. Son, and A. Starinets, Phys.Rev.Lett. **94**, 111601 (2005), hep-th/0405231.

[44] P. Danielewicz and G. Odyniec, Phys. Lett. B 157, 146 (1985).

[45] Q. B. Pan and P. Danielewicz, Phys. Rev. Lett. 70, 2062 (1993).

[46] J. Zhang, S. Das Gupta and C. Gale, Phys. Rev. C 50, 1617 (1994).

[47] B. A. Li, Phys. Lett. B 300, 14 (1993); Nucl. Phys. A 570, 797 (1994).

[48] G. Q. Li, C. M. Ko, and B. A. Li, Phys. Rev. Lett. 74, 235 (1995); G. Q. Li and C. M. Ko, Nucl. Phys. A 594, 460 (1995); Phys. Rev. C 54, 1897, R2159 (1996).

[49] J.-Y. Ollitrault, Nucl. Phys. A 638, 195c (1998).

[50] P. Romatschke and U. Romatschke, Phys.Rev.Lett. **99**, 172301 (2007), 0706.1522.

[51] H. Song and U. W. Heinz, Phys.Rev. **C78**, 024902 (2008), 0805.1756.

[52] P. R. Sorensen, "Kaon and Lambda production at intermediate p_T: insights into the hadronization of the bulk partonic matter created in Au + Au collisions at RHIC," *Ph.D thesis(2003),* nucl-ex/0309003.

[53] **STAR** Collaboration, J. Adams *et al.*, "Multi-strange baryon elliptic flow in Au + Au collisions at $\sqrt{s_{NN}} = 200$ GeV," *Phys. Rev. Lett.* **95** (2005) 122301, nucl-ex/0504022.

[54] U. W. Heinz, "Thermalization at RHIC," *AIP Conf. Proc.* **739** (2005) 163–180, nucl-th/0407067.

[55] R.D. Field and R.P.Feynman, *Phys. Rev.* **D15**, 2590 (1977)

[56] K.P. Das And R.C. Hwa, *Phys. Lett.* **B68**, 459 (1977)

[57] R.J. Fries et al. *Phys. Rev. Lett.* **90**, 202303 (2003).

[58] V. Greco et al., *Phys. Rev. Lett.* **90**, 202302 (2003)

[59] R. Bellwied, "What are the degrees of freedom in the partonic fluid at RHIC ?" arxiv/0709.4454.

[60] H. Song, "Causal Viscous Hydrodynamics for Relativistic Heavy Ion Collisions" arxiv/0908.3656.

[61] M. Guo-Liang and W. Xin-Nian "Jets, Mach Cones, Hot Spots, Ridges, Harmonic Flow, Dihadron, and Hadron Correlations in High-Energy Heavy-Ion Collisions,"ISSN:1079-7114, *Nucl. Phys.* **A750** (2005) 30–63, 10.1103/physrevlett.106.162301.

[62] B. Schenke "BNL: The Shape and Flow of Heavy Ion Collisions 490th Brookhaven Lecture" .

[63] U. W. Heinz, H. Song, and A. K. Chaudhuri, "Dissipative hydrodynamics for viscous relativistic fluids," *Phys. Rev.* **C73** (2006) 034904, nucl-th/0510014.

[64] P. F. Kolb, U. W. Heinz, P. Huovinen, K. J. Eskola, and K. Tuominen, "Centrality dependence of multiplicity, transverse energy, and elliptic flow from hydrodynamics," *Nucl. Phys.* **A696** (2001) 197–215, hep-ph/0103234.

[65] H. Song and U. W. Heinz, "Suppression of elliptic flow in a minimally viscous quark- gluon plasma," *Phys. Lett.* **B658** (2008) 279–283, 0709.0742.

[66] U. W. Heinz, "Concepts of heavy-ion physics," hep-ph/0407360.

[67] P. Huovinen, P. F. Kolb, U. W. Heinz, P. V. Ruuskanen, and S. A. Voloshin, "Radial and elliptic flow at RHIC: further predictions," *Phys. Lett.* **B503** (2001) 58–64, hep-ph/0101136.

[68] K. Aamodt *et al.* [The ALICE Collaboration], "Elliptic flow of charged particles in Pb-Pb collisions at 2.76 TeV," Phys. Rev. Lett. **105**, 252302 (2010). .

[69] L.P. Csernai, *Introduction to relativistic heavy ion collisions* (Wiley&Sons, Chichester (UK), 1994).

[70] U. W. Heinz and P. F. Kolb, "Two RHIC puzzles: early thermalization and the HBT problem," hep-ph/0204061.

[71] K. Yagi, T. Hatsuda, and Y. Miake, *Quark-Gluon Plasma*, (Cambridge University Press, Cambridge, 2005)

[72] F. Gelis, E. Iancu, J. Jalilian-Marian, and R. Venugopalan, Ann. Rev. Nucl. Part. Sci. **60** (2010) 463.

[73] R. Bhalerao, "Relativistic heavy-ion collisions" arxiv/1404.3294.

[74] S. Richard, "Strings and Things: The Discovery of the strongly interacting Quark Gluon Plasma at the Relativistic Heavy ion Collider" .

[75] L. D. McLerran and R. Venugopalan, "Computing quark and gluon distribution functions for very large nuclei," *Phys. Rev.* **D49** (1994) 2233–2241, hep-ph/9309289.

[76] L. D. McLerran and R. Venugopalan, "Gluon distribution functions for very large nuclei at small transverse momentum," *Phys. Rev.* **D49** hep-ph/9311205.

[77] T. Lappi and L. McLerran, "Some features of the glasma," *Nucl. Phys.* **A772** (2006) 200–212, hep-ph/0602189.

[78] U. W. Heinz, "Kinetic theory for nonabelian plasmas," *Phys. Rev. Lett.* **51** (1983) 351.

[79] U. W. Heinz, "Quark - gluon transport theory. part 1. the classical theory," *Ann. Phys.* **161** (1985) 48.

[80] U. W. Heinz, "Quark - gluon transport theory. part 2. color response and color correlations in a quark-gluon plasma," *Ann. Phys.* **168** (1986) 148.

[81] H.-T. Elze and U. W. Heinz, "Quark - gluon transport theory," *Phys. Rept.* **183** (1989) 81–135.

[82] H. Sorge, H. Stoecker, and W. Greiner, "Poincare invariant Hamiltonian dynamics: modeling multi - hadronic interaction in a phase space appproach," *Annals Phys.* **192** (1989) 266–306.

[83] P. Romatschke, "NEW DEVELOPMENTS IN RELATIVISTIC VISCOUS HYDRODYNAMICS," *International Journal of Modern Physics E* **95** (2005) 122301, 10.1142/s0218301310014613. 1793-6608.

[84] L. Euler, "Principes généraux du mouvement des fluides", Mém. Acad. Sci. Berlin 11 (1755) [printed in 1757]. Also in Opera omnia, ser. 2, 12, (1907) 54-91, E226.

[85] L.D. Landau and E.M. Lifshitz, Course of Theoretical Physics Volume 6, "Fluid Mechanics", Elsevier, 2nd edition (1987).

[86] C.L.M.H. Navier, "Mémoire sur les lois du mouvement des fluides", Mém. Acad. Sci. Inst. France, 6, (1822), 389-440.

[87] G.G. Stokes, "On the theories of the internal friction of fluids in motion, and of the equilibrium and motion of elastic solids", Trans. Camb. Philos. Soc. 8:287-319 (1845).

[88] E. Iancu and R. Venugopalan, arXiv:hep-ph/0303204.

[89] M. Prakash, M. Prakash, R. Venugopalan and G. Welke, Phys. Rept. **227** (1993) 321.

[90] D. T. Son and A. O. Starinets, JHEP **0603** (2006) 052 [arXiv:hep-th/0601157].

[91] D. H. Rischke, arXiv:nucl-th/9809044.

[92] A. Muronga, Phys. Rev. C **69** (2004) 034903 [arXiv:nucl-th/0309055].

[93] W. A. Hiscock and L. Lindblom, Phys. Rev. D **31** (1985) 725.

[94] P. Kostadt and M. Liu, Phys. Rev. D **62** (2000) 023003.

[95] J.C. Maxwell, Phil. Trans. R. Soc. **157** (1867) 49.

[96] C. Cattaneo, Atti Sem. Mat. Fis. Univ. Modena **3** (1948) 3.

[97] D. Jou, J. Casas-Vazquez and G. Lebon, Rep. Prog. Phys. **51** (1988) 1105.

[98] D.D. Joseph and L. Preziosi, Rev. Mod. Phys. **61** (1989) 41.

[99] R. B. Clare and D. Strottman, "Relativistic hydrodynamics and heavy ion reactions," *Phys. Rept.* **141** (1986) 177–280.

[100] P. Arnold, G. D. Moore, and L. G. Yaffe, "The fate of non-abelian plasma instabilities in 3+1 dimensions," *Phys. Rev.* **D72** (2005) 054003, hep-ph/0505212.

[101] P. Romatschke and R. Venugopalan, "The unstable Glasma," *Phys. Rev.* **D74** (2006) 045011, hep-ph/0605045.

[102] U. Gursoy, D. Kharzeev, E. Marcus, K. Rajagopal and C. Shen "Charge-dependent flow induced by magnetic and electric fields in heavy ion collisions," *Phys. Rev.* **D74** (2006) 2469-9993, PhysRevC.98.055201.

[103] J. Harmen "The Effects of topological charge change in heavy ion collisions: 'Event by event P and CP violation", *nuclphysa.2008.02.298* arXiv:0711.0950

[104] V. Skokov, A. Illarionov and V. Toneev "Estimate of the magnetic field strength in heavy-ion collisions", *10.1142/S0217751X09047570* Int. J. Mod. Phys. arXiv:0907.1396

[105] U. Heinz and S. Moreland "Energy dependent growth of the nucleon and hydrodynamic initial conditions" *https://arxiv.org/abs/1108.5379v2* Physical Review C.1089-490X .

[106] C. Shen, Z. Qiu, H. Song, J. Bernhard, S. Bass, U. Heinz, "The iEBE-VISHNU code package for relativistic heavy-ion collisions", .

[107] W. Broniowski, M. Rybczynski, P. Bozek, GLISSANDO: Glauber initial-state simulation and more.., Comput.Phys.Commun. 180 (2009) 69–83. arXiv:0710.5731, doi:10.1016/j.cpc.2008.07.016.

[108] B. Alver, M. Baker, C. Loizides, P. Steinberg, The PHOBOS Glauber Monte CarloarXiv:0805.4411.

[109] C. Loizides, J. Nagle, P. Steinberg, Improved version of the PHOBOS Glauber Monte CarloarXiv:1408.2549.

[110] D. Kharzeev, E. Levin, M. Nardi, The Onset of classical QCD dynamics in relativistic heavy ion collisions, Phys.Rev. C71 (2005) 054903. arXiv:hep-ph/0111315, doi:10.1103/PhysRevC.71.054903.

[111] D. Kharzeev, E. Levin, M. Nardi, Color glass condensate at the LHC: Hadron multiplicities in pp, pA and AA collisions, Nucl.Phys. A747 (2005) 609–629. arXiv:hep-ph/0408050, doi:10.1016/j.nuclphysa.2004.10.018.

[112] V. Voronyuk, V. Toneev, W. Cassing, E. Bratkovskaya, V. Konchakovski, . SVoloshin Electromagnetic field evolution in relativistic heavy-ion collisions Physical.Review.C.62.361(2012) arXiv:1202.3233v1,doi.org/10.1103/physrevc.83.054911.

[113] H. Niemi, G. Denicol, P. Huovinen, E. Molnar, and D. Rischke, "Influence of the Shear Viscosity of the Quark- Gluon Plasma on Elliptic Flow in Ultrarelativistic Heavy-Ion Collisions", Phys. Rev. Lett. 106, 212302 (2011). .

[114] P. Huovinen and P. Petreczky QCD Equation of State and Hadron Resonance Gas Physical.Review.C.62.361(2012) arXiv:0912.2541,https://doi.org/10.1016/j.nuclphysa.2010.02.015.

[115] W. Reisdorf, H. Ritter "Collective Flow in Heavy-Ion Collisions", Annual Review of Nuclear and Particle Science. 47: 663. *Annals Phys.* **1997ARNPS** hep-ph/0605045. doi:10.1146/annurev.nucl.47.1.663.

[116] R. Snellings,"Elliptic flow: A brief review". New Journal of Physics", arXiv:1102.3010.

[117] A. Sickles"RHIC The Smallest Drops of the Hottest Matter? New Investigations at the Relativistic Heavy Ion Collider," https://www.bnl.gov/rhic/video.php.

[118] A. Bilandzic, V. Naomi, J. Ollitrault and R. Snellings, "Electromagnetic field evolution in relativistic heavy-ion collisions" physrevc.83.014909 https://arxiv.org/abs/0801.3915,doi.org/10.1103/physrevc.83.054911.

[119] K. H. Ackermann *et al.* [STAR Collaboration], Phys. Rev. Lett. **86**, 402 (2001).

[120] B. B. Back *et al.* [PHOBOS Collaboration], Phys. Rev. Lett. **89**, 222301 (2002).

[121] S. S. Adler *et al.* [PHENIX Collaboration], Phys. Rev. Lett. **91**, 182301 (2003).

[122] A. M. Poskanzer and S. A. Voloshin, Phys. Rev. C **58**, 1671 (1998).

[123] J. Y. Ollitrault, Nucl. Phys. A **590**, 561C (1995).

[124] M. Miller and R. Snellings, arXiv:nucl-ex/0312008.

[125] B. Alver *et al.* [PHOBOS Collaboration], Phys. Rev. Lett. **98**, 242302 (2007).

[126] J. Adams *et al.* [STAR Collaboration], Phys. Rev. C **72**, 014904 (2005).

[127] S. Voloshin and Y. Zhang, Z. Phys. C **70**, 665 (1996).

[128] P. Danielewicz and G. Odyniec, Phys. Lett. B **157**, 146 (1985).

[129] J. Y. Ollitrault, arXiv:nucl-ex/9711003.

[130] Y. Zhong, C. Yang, X. Cai and S. sFeng "A Systematic Study of Magnetic Field in Relativistic Heavy-Ion Collisions in the RHIC and LHC Energy Regions", Advances in High Energy Physics,Hindawi Limited 10.1155/2014/193039.

[131] E. Marcus, "Magnetohydrodynamics at Heavy Ion collision", Bachelor Thesis (2015), Utrecht University.

[132] S. K. Das, S. Plumari, S. Chatterjee, J. Alam, F. Scardina, and V. Greco, "Directed Flow of Charm Quarks as a Witness of the Initial Strong Magnetic Field in Ultra-Relativistic Heavy Ion Collisions", Phys. Lett. B 768, 260.

[133] W. Deng, and X. Huang, Event-by-event generation of electromagnetic fields in heavy-ion collisions, Phys. Rev. C **85**, 044907. arxiv.org/pdf/1201.5108, doi:10.1103/physrevc.85.044907.